Search for Higgs boson pair production in the $b\bar{b}b\bar{b}$ final state at the Large Hadron Collider

Rebecca Jane Falla
University College London

Submitted to University College London in fulfilment
of the requirements for the award of the
degree of **Doctor of Philosophy**

April 11, 2016

Declaration

I, Rebecca Jane Falla confirm that the work presented in this thesis is my own. Where information has been derived from other sources, I confirm that this has been indicated in the thesis.

Rebecca Falla _____

Abstract

The work presented in this thesis focuses on the search for resonant and non-resonant Higgs boson pair production in the $b\bar{b}b\bar{b}$ final state at the LHC. All of the searches require the use of high transverse momentum b-tagged jet systems.

The first search presented is performed using a dataset of proton-proton collisions at $\sqrt{s} = 8$ TeV, collected in 2012 with the ATLAS detector, corresponding to an integrated luminosity of 19.5 fb^{-1}. The Higgs boson decay products are reconstructed as a pair of close-by small radius b-tagged jets with a high transverse momentum, known as "dijets". The resonant signals looked for are a Randall-Sundrum Kaluza-Klein graviton, G^*, and a heavy neutral scalar boson in the 2HDM model, H. A non-resonant search is also performed. No evidence for resonant or non-resonant Higgs boson pair production is observed. An upper limit on the cross-section for $\sigma(pp \to G^* \to hh \to b\bar{b}b\bar{b})$ of 3.2 fb is set for a G^* mass of 1.0 TeV, at the 95% confidence level. The search for non-resonant Standard Model hh production sets an observed 95% confidence level upper limit on the production cross-section $\sigma(pp \to hh \to b\bar{b}b\bar{b})$ of 202 fb, compared to a SM prediction of $\sigma(pp \to hh \to b\bar{b}b\bar{b}) = 3.6 \pm 0.5$ fb.

In preparation for Run 2 and the HL-LHC simulation studies based on $\sqrt{s} = 14$ TeV are made. A non-resonant search using the dijet method used in Run 1 is presented. A resonant study is also presented which shows a new method for reconstructing $pp \to X \to hh \to b\bar{b}b\bar{b}$ events. It uses the combination of many Higgs boson reconstruction techniques which vary with the Higgs boson

transverse momentum and is shown to be excellent at providing a high signal efficiency.

Acknowledgements

I would like to thank everyone who has helped me over the past three and a half years. Firstly, I would like to thank my supervisor, Nikos Konstantinidis, who has guided all of my work and given help when needed. Next I would like to thank my analysis team, especially Ben Cooper and David Wardrope who have helped me endlessly with physics and coding. It has been a pleasure to be part of the UCL HEP group and I would like to thank everyone in it, especially my colleagues in C17.

I would like to thank all my friends, who are incredibly important to me, and have provided encouragement, emotional support and entertainment. Special thanks goes to my bowling friends (you know who you are!). Lastly I would like to thank my partner, Pip, and my family, for all of their love and support.

Preface

This thesis covers searches for resonant and non-resonant Higgs boson pair production at the LHC. Firstly there is an analysis performed on data collected in 2012 by the ATLAS detector which is published in Ref. [1] and is presented here in Chapter 5 and secondly there are some simulation-based studies for searches at $\sqrt{s} = 14$ TeV presented in Chapter 6, for which the non-resonant search is published in Ref. [2] and the resonant search is not currently published.

The team working on the ATLAS search was John Allison, Ben Cooper, Nikos Konstantinidis, Luke Lambourne, Nurfikri Norjoharuddeen, David Wardrope and myself. Although I was involved in all parts of the analysis, I mainly contributed towards the event selection and its optimisation, in particular the trigger selection, $t\bar{t}$ veto and the Mass Dependent Cuts; the treatment of the multijet background, along with the cross-checks applied to it and systematic uncertainties including the generation of signal samples to estimate their theoretical uncertainties.

The team working on the non-resonant 14 TeV search was David Wardrope, Eric Jansen, Nikos Konstantinidis, Ben Cooper, Nurfikri Norjoharuddeen and myself. In this analysis I was only involved in the signal topology work.

The team working on the resonant 14 TeV search was Ben Cooper, Kristian Gregerson, Nikos Konstantinidis, David Wardrope, and myself. I worked on all parts of this study.

In addition to the work presented in this thesis, I also worked on ATLANTIS which is an event display for ATLAS. This was to gain authorship accreditation on the ATLAS experiment. My role was to make sure the event displays were working in the ATLAS Control Room, make event displays for the public, present software tutorials, and also some software development.

Contents

List of Figures

List of Tables

Chapter 1.

Introduction

The discovery of the Higgs boson [3, 4] in 2012 at the Large Hadron Collider (LHC) has opened up many new search channels for Beyond the Standard Model physics. Many new physics models predict Higgs boson pair production at rates significantly higher than in the Standard Model (SM) [5–7]. These models include TeV-scale resonances, such as the Randall-Sundrum [8, 9] model which predicts a Kaluza-Klein graviton, G^*, or two-Higgs-doublet models which predict a heavy neutral scalar boson, H, decaying into a pair of Higgs bosons. Non-resonant models which predict enhanced rates of higgs boson pair production include, for example, $t\bar{t}hh$ or $VVhh$ vertices [10, 11].

The searches presented in this thesis look for Higgs boson pair production decaying into four b-quarks ($pp \to hh \to b\bar{b}b\bar{b}$) in either the resonant or non-resonant case at the LHC using ATLAS. The all hadronic final state means that there is a large multijet background; however, due to the large expected branching ratio for SM $h \to b\bar{b}$ ($\sim 57\%$) and the distinctive topology created by requiring that the Higgs bosons have sufficiently high transverse momentum, p_{T}, one can achieve good sensitivity to this process.

The first few chapters of this thesis provide background information with a theoretical overview given in Chapter 2, a description of the ATLAS detector in Chapter 3, and a discussion of some of the techniques and tools used in an ATLAS analysis provided in Chapter 4. Chapter 5 presents the search for resonant and non-resonant $pp \to hh \to b\bar{b}b\bar{b}$ using 19.5 fb^{-1} of data collected with ATLAS in 2012, at a centre-of-mass ($\sqrt{s}$) energy of 8 TeV [1]. Chapter 6 presents a study into searches for $pp \to hh \to b\bar{b}b\bar{b}$ at $\sqrt{s} = 14$ TeV, firstly presenting a non-resonant MC study [2],

and then presenting a proof of concept for a new method to reconstruct resonant Higgs boson pair production at high Higgs boson boost.

Chapter 2.

The Standard Model of Particle Physics

2.1. The Standard Model

The Standard Model of Particle Physics (SM) [12, 13] is a theory which describes the elementary particles and all their fundamental interactions, excluding gravity. It is a quantum field theory which combines electroweak theory [14], the Brout-Englert-Higgs mechanism [15–19], and quantum chromodynamics (QCD) [20]. The Electroweak theory is the unification of the electromagnetic and weak interactions. The Brout-Englert-Higgs mechanism explains how weak gauge bosons acquire mass and allows for fermion masses to be included in the theory and QCD describes the interactions of the strong force. Bosons are particles with integer spin which obey Bose-Einstein statistics, fermions are particles which have half-integer spin and obey Fermi-Dirac statistics (and therefore obey the Pauli exclusion principle).

There are twelve elementary spin-$\frac{1}{2}$ particles predicted by the Standard Model. They can be split into two families - quarks and leptons. Both families have three known generations of particle. Quarks are summarised in Table 2.1, they carry colour charge and partake in electroweak and strong interactions. Each generation contains an "up-type" and a "down-type" quark. They are the particles which (along with gluons) make up atomic nuclei. Leptons are summarised in Table 2.2, each generation consists of an electrically charged particle paired with a neutral "neutrino". All leptons are colour neutral, so neutrinos can only interact via the weak force

Quark	Symbol	Charge [e]	Spin [$\frac{h}{2\pi}$]	Mass [GeV]
up	u	$\frac{2}{3}$	$\frac{1}{2}$	0.002
down	d	$-\frac{1}{3}$	$\frac{1}{2}$	0.005
charm	c	$\frac{2}{3}$	$\frac{1}{2}$	1.3
strange	s	$-\frac{1}{3}$	$\frac{1}{2}$	0.1
top	t	$\frac{2}{3}$	$\frac{1}{2}$	173
bottom	b	$-\frac{1}{3}$	$\frac{1}{2}$	4.2

Table 2.1.: The Standard Model quarks and some of their properties, paired into their generations [21].

Lepton	Symbol	Charge [e]	Spin [$\frac{h}{2\pi}$]	Mass [GeV]
electron	e	-1	$\frac{1}{2}$	0.0005
electron neutrino	ν_e	0	$\frac{1}{2}$	$< 2 \times 10^{-9}$
muon	μ	-1	$\frac{1}{2}$	0.106
muon neutrino	ν_μ	0	$\frac{1}{2}$	$< 2 \times 10^{-4}$
tau	τ	-1	$\frac{1}{2}$	1.8
tau neutrino	ν_τ	0	$\frac{1}{2}$	$< 2 \times 10^{-2}$

Table 2.2.: The Standard Model leptons and some of their properties, paired into their generations. [21]

making them hard to detect. Each fermion has an anti-partner which has the same mass but opposite electric charge and other quantum numbers.

There are four types of spin-1 force-carrying gauge bosons predicted in the Standard Model. They are summarised in Table 2.3 along with the Higgs Boson (see Section 2.1.2). The photon mediates the electromagnetic force, the$W^\pm$ and Z^0 mediate the weak and the gluons mediate the strong force (see Section 2.1.1).

The Standard Model has been very successful so far, not only have $\sim \frac{1}{3}$ of its elementary particles been experimentally discovered after they were predicted but it

Boson	Symbol	Charge [e]	Spin [$\frac{h}{2\pi}$]	Mass [GeV]
photon	γ	0	1	0
$W^{\pm}$	$W^{\pm}$	± 1	1	80.4
Z	Z^0	0	1	91.2
gluon	g	0	1	0
Higgs boson	h	0	0	125

Table 2.3.: The Standard Model bosons [21].

has also predicted measurable quantities to great accuracy. One such example is the fine structure constant which has been predicted and measured to within a precision of better then one part in a billion. There are, however, a few problems with the Standard Model and these are discussed in Section 2.2.

2.1.1. Quantum Chromodynamics

Quantum Chromodynamics is the SU(3) quantum field theory that describes the strong force: the interaction of quarks and gluons. The strong force affects particles with colour charge, this is analogous to electric charge in QED except that the charge has three types, denoted as RGB (red, green, and blue) where the neutral state can be either the mixture of all three colour-charges or a state combining a colour charge with its anti-charge, e.g. $R\bar{R}$. Quarks have a single colour-charge. Gluons, which are the mediating bosons of the strong force, have pairs of colour-charge. They can also self-interact. These two properties lead to two effects: colour confinement, and asymptotic freedom.

Particles with colour-charge cannot be isolated, this is known as colour confinement. For instance, when a $q\bar{q}$ pair has energy applied to it they separate and the virtual gluons connecting them get "stretched" out. At some point it becomes more energetically favourable for the gluons to create a new $q\bar{q}$ pair in-between the original pair than for the gluons to be stretched any more. This process repeats until the quarks reach some ground state. In hadron colliders, this results in showers of quarks and gluons emanating from a single parton, which cluster into hadrons which can be measured. The spray of particles is what is known as a jet.

As energy increases (or equivalently distance decreases) the coupling of the strong force decreases asymptotically, this is known as asymptotic freedom. The fact that the coupling constant changes with energy/distance can be explained with screening. In QED, screening is when the effective strength of an EM field is decreased by virtual e^+e^- pairs polarising the vacuum. In QCD, this also happens but with $q\bar{q}$ pairs, however there is a competing effect from virtual gluons which end up increasing the effective colour charge (anti-screening). At high energy/small distance the anti-screening effect is negligible so the gluon field strength decreases. The low coupling strength at high energies means that QCD can be calculated perturbatively.

At low energies, ~ 500 MeV, the coupling of the strong force becomes extremely large (~ 1), causing perturbation theory to stop working, so perturbative QCD cannot make reliable predictions. To overcome this problem, experimentalists use parton distribution functions (PDFs), these give the probability of finding a particle with a certain momentum fraction, x, given an energy scale of the hard interaction, Q. PDFs are tuned to experimental data.

2.1.2. The Higgs Boson

For the unification of the electromagnetic and weak forces into the electroweak force there has to be a spontaneous symmetry break which gives mass to some of the electroweak gauge bosons. The mechanism that does this is called the Brout-Englert-Higgs mechanism. It introduces a complex scalar doublet under the $\mathrm{SU(2)_L}$ gauge group which introduces 4 degrees of freedom, 3 of these couple to the $W^\pm$ and Z^0 bosons to give them mass whereas the remaining degree of freedom is a spin-0 massive gauge boson – the Higgs boson. The Higgs boson can interact with any massive particle including itself.

In July 2012 the Higgs boson was discovered at the LHC by ATLAS [3] and CMS [4]. It has a mass of $125.1 \pm 0.2\,(stat.) \pm 0.1\,(syst.)$ GeV [22] and measurements of its properties so far are consistent with the SM predictions [23]. At the LHC its main production modes are gluon fusion (ggF) and vector boson fusion (VBF), which can be seen in Figure 2.1 and they account for 86% and 7% of production during Run-1 at $\sqrt{s} = 8$ TeV respectively. The main decay channel for the Higgs boson is $h \to b\bar{b}$. It has a branching ratio of $\sim 57\%$, but, despite this, the Higgs boson has not been discovered in this channel yet due to the large multijet backgrounds [24, 25] [26–28].

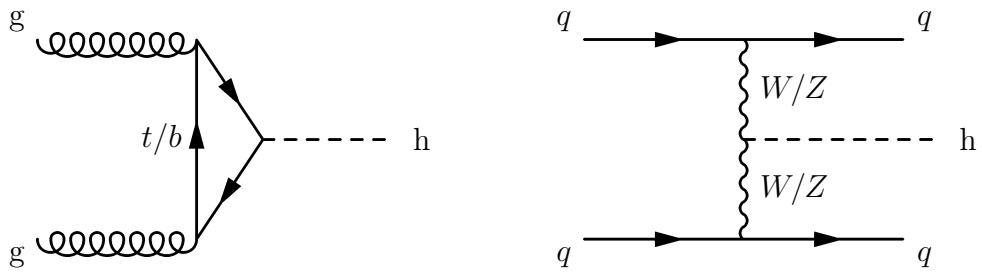

(a) gluon fusion **(b)** vector boson fusion

Figure 2.1.: The two leading Higgs boson production mechanisms at the LHC.

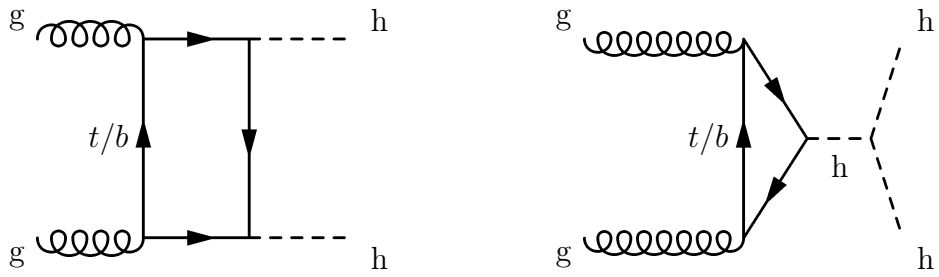

(a) box diagram **(b)** triangle diagram

Figure 2.2.: Higgs boson pair production diagrams which contribute to the gluon fusion process.

The discovery of the Higgs boson has opened up many new searches because the Higgs boson can be used as a tool for discovery. The searches presented in this thesis are looking for Higgs boson pair production decaying into four b-quarks in either the non-resonant case: $pp \to hh \to b\bar{b}b\bar{b}$ or a new resonance which decays in this manner: $pp \to X \to hh \to b\bar{b}b\bar{b}$. If any discovery was made, then this would in fact be a double discovery due to the search in the $h \to b\bar{b}$ decay channel not having a significant excess yet. In the SM, the main production mode for Higgs boson pairs is gluon fusion. There are two types of diagram which contribute – box and triangle; they can be seen in Figure 2.2. The four b-quark final state is a hard signature to search for due to the large irreducible multijet background that comes from having an all-hadronic final state, but the use of boosted techniques – where the Higgs bosons are required to have high transverse momenta, means that these studies are possible.

At $\sqrt{s} = 8$ TeV ATLAS and CMS have performed searches for Higgs boson pair production. ATLAS in the $\gamma\gamma b\bar{b}$ [29], $b\bar{b}\tau\tau$ [30] and $\gamma\gamma WW^*$ [30] final states at $\sqrt{s} = 8$ TeV along with the $b\bar{b}b\bar{b}$ final state which is presented in Chapter 5 and in Ref. [1]. CMS has performed searches in the $b\bar{b}\tau\tau$ [31], $\gamma\gamma b\bar{b}$ [32], multi-lepton and multi-lepton plus photons final states [33], as well as their own $b\bar{b}b\bar{b}$ search [34].

2.2. Beyond the Standard Model

Despite the successes of the Standard Model, there are many unresolved problems with it, perhaps the most notable one is that there is no inclusion of gravity in it. Other problems include the lack of an explanation for Dark Matter which makes up $\sim 85\%$ of the total matter of the universe, and also the lack of an explanation for why the Weak force is 10^{32} times stronger than Gravity (this problem is known as the "hierarchy problem"). Due to these problems with the Standard Model, it is believed that there must be "new physics" out there and so experimentalists search for it at the LHC and also elsewhere. At the LHC there are two common methods for searching for new physics, the first is "bump hunting", this is where peaks are looked for in continuous distributions (usually resonances in invariant mass distributions). The second is non-resonant searches which involve looking at the number of measured events against the number expected.

2.2.1. Theories Beyond the Standard Model

Theories which extend the Standard Model in the hope of answering some of the unresolved questions are known as "Beyond the Standard Model" or BSM theories. There are two which are searched for in Chapters 5 and 6: the Randall-Sundrum Model and the Two-Higgs Doublet Model.

Randall-Sundrum Model

The Randall-Sundrum (RS) Model [8,9] yields a solution to the heirarchy problem. It does this by introducing an extra dimension through which only gravity propagates. The extra dimension is bounded by two branes - the TeV brane, where the Standard

Model particles reside, and the Planck brane where gravity is strong. The change in the strength of gravity between the two branes is caused by the extra dimension being warped. The warped extra dimension has a curvature parameter k. The RS model predicts that there is a spin-2 particle called the graviton, G^*, whose mass should be at the TeV scale, of which one of its decay channels is via two Higgs bosons: $G^* \to hh$, where h is the $m_h = 125$ GeV SM Higgs boson.

Two-Higgs Doublet Model

The Two-Higgs Doublet Model (2HDM) [35] is an extension to the Standard Model which involves adding an extra higgs doublet to the theory such that there are now five physical states: the 125 GeV Higgs boson, h, a heavy neutral scalar boson, H, two charged Higgs bosons, $H^{\pm}$, and a CP odd pseudoscalar, A. The heavy neutral scalar boson H can decay to a pair of light Higgs bosons and it is searched for in Chapter 5. The six free parameters in 2HDM models are $\tan\beta$, α and the 4 Higgs masses: m_h, m_H, m_A, $m_{H^{\pm}}$. $\tan\beta$ is the ratio of the vacuum expectation values of the two Higgs doublets and α is the mixing angle between the two neutral CP-even scalars. There are many types of 2HDM model, two that are commonly searched for are Type-I, where charged fermions only couple to the second doublet, and Type-II, where up-type and down-type quarks couple to separate Higgs doublets.

One of 2HDMs main motivations is supersymmetry (SUSY) [36], which provides a solution to the hierarchy problem by introducing a supersymmetric partner particle for each SM particle. The additional Higgs doublet is required to give mass to the up- and down-type quarks in a way which is invariant under supersymmetric transformations.

Chapter 3.

The Large Hadron Collider and the ATLAS Detector

3.1. The Large Hadron Collider

The Large Hadron Collider (LHC) [37] is the world's highest energy particle accelerator. It is a proton-proton collider designed to deliver $\mathcal{O}(10^9)$ collisions per second, by firing bunches of 1.1×10^{11} protons around a 27 km ring at a centre-of-mass energy ($\sqrt{s}$) of 14 TeV, reaching an instantaneous luminosity of over $10^{34}\text{cm}^{-2}\text{s}^{-1}$. It is located underground at the French-Swiss border near Geneva at depths between 50m and 175m. The bunches of protons are focussed together at points around the ring where the detectors are found. There are four main detectors: ATLAS [38], CMS [39], LHC*b* [40] and ALICE [41]. The LHC is not running at its design energy yet, in 2012 it ran at $\sqrt{s} = 8$ TeV and the 20.3 fb^{-1} of data collected by ATLAS then is the data used in Chapter 5. In 2015 it started running at $\sqrt{s} = 13$ TeV.

Figure 3.1 shows the accelerator layout at CERN. The protons used in the LHC are produced from hydrogen gas. They are injected into a linear accelerator - Linac 2 where they are accelerated to an energy of 50 MeV and then they are passed onto the Proton Synchrotron Booster which brings them up to 1.4 GeV. The beam is then injected into the Proton Synchrotron where they reach energies of 25 GeV. After this they are passed to the Super Proton Synchrotron where they are accelerated to 450 GeV, and finally they are passed into the LHC ring where they are cycled around until reaching the desired energy.

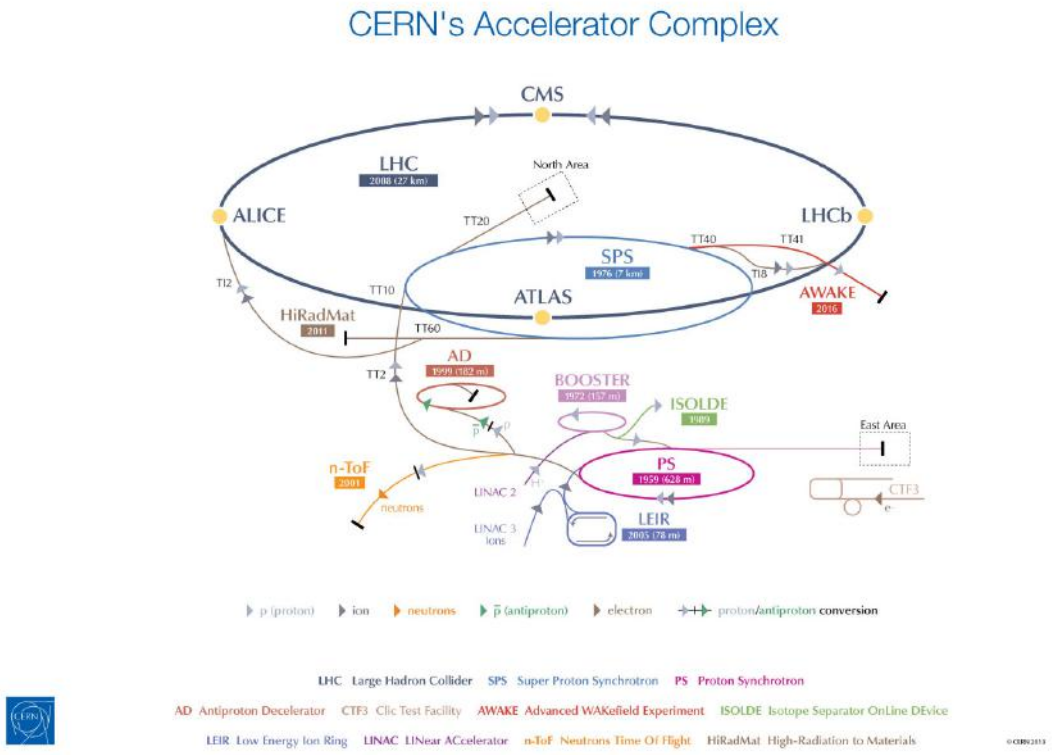

Figure 3.1.: The CERN accelerator complex [42].

3.2. The ATLAS Detector

ATLAS is one of two general purpose detectors at the LHC (the other being CMS). It is a large machine which is 44m long, 25 m in diameter and weighs 7000 tonnes. A diagram of the ATLAS detector can be seen in Figure 3.2. The detector is comprised of many sub-systems (sub-detectors) which are designed to measure different things. From the beam line outwards the sub-detectors are: the *inner detector*, which measures charged particles' tracks and therefore momentum, the *calorimeters*, which measure the energy that particles deposit within them, and the *muon system*, which detects muons; all are described in more detail below.

The coordinate system within ATLAS is as follows: the origin is at the nominal interaction point, the x-axis points towards the centre of the LHC ring, the y-axis points upwards and the z-axis points along the beam-pipe in an anti-clockwise direction. The "transverse" plane is the plane perpendicular to the beam-pipe (the x-y plane) and the "longitudinal" direction is along the beam-pipe. In spherical coordinates the azimuthal angle, ϕ, starts at the x-axis and the polar coordinate, θ, starts at the z-axis. Pseudorapidity, η, is a more commonly used variable than θ. It is the rapidity, y, in the massless limit (such that it is independent of the particle's energy), and is defined in Equation 3.1. Objects with a low value of $|\eta|$ are referred to as "central" whilst objects with high $|\eta|$ values are "forward". η is useful for analyses because the rate of particle production is approximately flat in η.

$$\eta = -\ln \tan \frac{\theta}{2} \tag{3.1}$$

3.2.1. The Inner Detector

The inner detector (ID) is used to measure charged particle trajectories (tracks) and interaction vertices. It comprises a silicon pixel detector, a semiconductor tracker (SCT) and a transition radiation tracker (TRT). A diagram of the ID can be found in Figure 3.3. The ID fully covers the range $|\eta| < 2.5$.

The pixel detector is the component closest to the beam-pipe. It is used to detect particles which decay very quickly - close to the interaction point. It is made up of

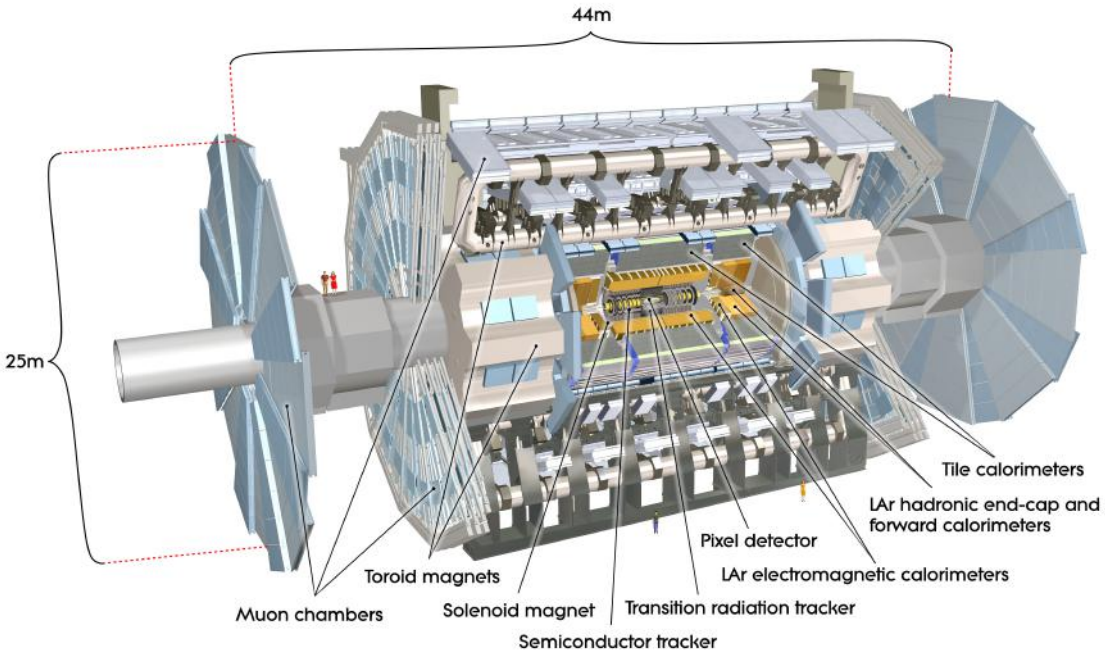

Figure 3.2.: The ATLAS detector [43].

80 million pixels, mostly of size $50 \times 400\mu m^2$, which are laid out as 3 disks in each endcap (13M pixels) and 3 barrel layers (67M pixels). It has an intrinsic resolution of about 10 μm in the transverse plane and 115 μm in the longitudinal plane.

The component outside the pixel detector is the SCT, it is 60 m^2 of silicon distributed over 9 disks in each endcap and 4 barrel layers, resulting in over 6M readouts. Each layer has two sets of strips which are back-to-back with a 40 mrad angle between them, in the barrel one set of strips in each layer is parallel to the beam direction whilst in the endcaps one layer runs radially, this is to ensure there are measurements in both η and ϕ. The mean pitch length is 80 μm. The SCT has a resolution of 17μm per layer in the direction transverse to the strips.

The outer layer of the ID is the TRT, a straw detector filled with xenon gas. It has over 350,000 readout channels and can make precision measurements of 130 μm in the transverse direction. Surrounding the ID is a 2T solenoid magnet which causes the charged particle tracks to bend so that their charge and momentum can be determined.

Impact parameters, which are the distance of closest approach between a track and the primary vertex are used when identifying the tracks which originate from the decays of b-hadrons. The ID of ATLAS achieves impact parameter resolutions down to $\sim$10 μm in the transverse plane and $\sim$80 μm in the beam direction.

3.2.2. The Calorimeters

Calorimeters measure the energy of particles which interact via the electromagnetic or strong force. A diagram of the calorimeters can be seen in Figure 3.4. The calorimeters in ATLAS are sampling calorimeters, they are made of alternating materials - a dense, passive one to initiate showers and an active one to measure the energy. The calorimeters are designed to give an accurate energy measurement in all but the most forward regions ($|\eta| > 4.9$) such that the missing energy in the transverse plane can be reconstructed from conservation of momentum. This missing energy is used as a proxy for neutrinos, or other (yet to be discovered) weakly interacting particles, which pass straight through ATLAS so they are undetectable by it.

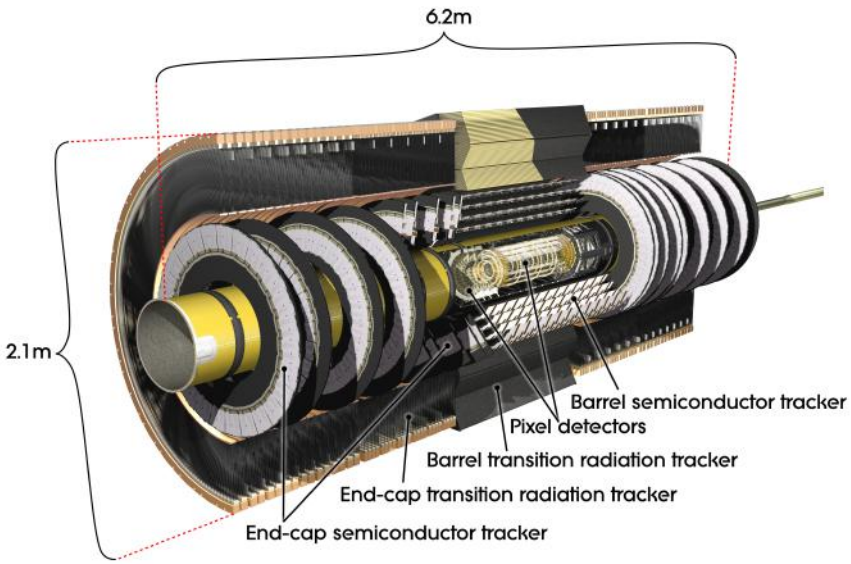

Figure 3.3.: The ATLAS Inner Detector [44].

The region covering $|\eta| < 1.475$ in the barrel and $1.375 < |\eta| < 3.2$ in the endcaps is the electromagnetic calorimeter (ECAL). Its passive material is lead and its active material (which is ionised by the EM shower) is liquid argon. The ECAL has an overall energy resolution of within $\sigma_E/E = 10\%/\sqrt{E} \pm 0.2\%$, where the first term is a stochastic term and the second term represents local non-uniformites in calorimeter response. The size of an EM shower is proportional to the radiation length, X_0, of the calorimeter material. The total depth of the ECAL is 22-33 X_0 in the barrel (depending on the η) and 24-38 X_0 in the endcaps.

The hadronic calorimeter surrounds the ECAL and is split into barrel, endcap and forward sections. The barrel region ($|\eta| < 1.0$) uses plastic scintillator tiles as its active sampling material and lead as its passive. There is an extended barrel region ($0.8 < |\eta| < 1.7$) which uses iron plates as the passive material and liquid argon as the active. The endcaps cover $1.5 < |\eta| < 3.2$ and are made of liquid argon and copper. The hadronic calorimeter energy resolution is dependent on the component and the type of particle, but all fall within the design resolution of $\sigma_E/E = 50\%/\sqrt{E} \pm 3\%$.

The forward calorimeter covers $3.1 < |\eta| < 4.9$ and uses liquid argon for its active material, the passive material is copper for the EM calorimeter and tungsten for the hadronic. The energy resolution for the forward calorimeter falls within $\sigma_E/E = 100\%/\sqrt{E} \pm 10\%$.

The size of a hadronic shower is proportional to the nuclear interaction length, λ, of the calorimeter material. The total depth of the entire active calorimeter region is about 9.7 λ in the barrel and 10 λ in the endcaps.

3.2.3. The Muon System

The muon spectrometer (MS) is used to measure the position and momenta of muons within the range $|\eta| < 2.7$. Muons (and neutrinos) are the only known particles which pass through the ID and calorimeters. A diagram showing the MS is shown in Figure 3.5. The MS is also used to trigger events with muons within the range $|\eta| < 2.4$. There are two parts of the MS which deal with measuring the tracks of muons: the Monitored Drift Tubes (MDTs) covering $|\eta| < 2.0$ and for closer to the beam pipe, $2.0 < |\eta| < 2.7$, the Cathode Strip Chambers (CSCs). Each MDT has an average spatial resolution of 80 μm in the y-z plane and 35 μm per chamber. The spatial

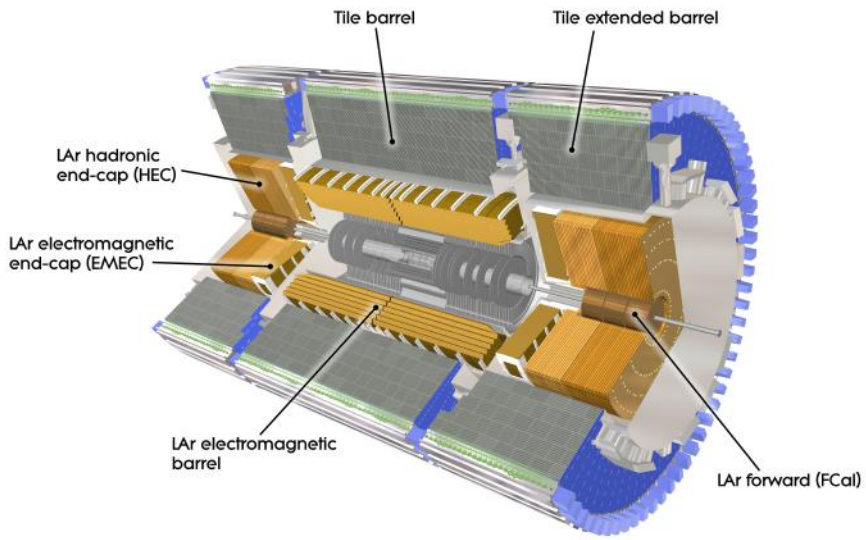

Figure 3.4.: The ATLAS calorimeters [45].

resolution of the CSC is about 40 μm in the y-z plane and 5 mm in the transverse plane. The MS has a momentum resolution of around 10% for p_{T} up to 1 TeV. For triggering there are also two types of detector: the Resistive-Plate Chambers (RPCs) which are central, ($|\eta| < 1.05$) and elsewhere the Thin-Gap chambers (TGC) at $1.05 < |\eta| < 2.4$. To bend the muons' tracks there are three air-filled toroidal magnets, one in the barrel and one in each endcap.

3.2.4. The Trigger System

During 2012 the LHC provided ATLAS with bunches of protons spaced 50ns apart, this corresponds to an event rate of 20MHz. This is an enormous amount of data and as such it was impossible to record all of the events. The ATLAS trigger system is used to ensure that events which are physically interesting are recorded by using hardware and specialised computer algorithms to pick them out. The trigger system works in three sequential stages: the Level 1 trigger (L1), the Level 2 trigger (L2) and the Event Filter (EF). L2 and the EF are collectively called the High-Level Trigger (HLT).

The Level 1 trigger is hardware-based. It takes coarse granularity information from the calorimeters and MS and decides whether an event has any Regions of Interest (RoIs) by looking for possible signatures that could indicate electrons, muons, taus, jets, photons or E_{T}^{miss}. If any RoIs are found then they are passed to L2. The L1 trigger reduces the event rate to 75kHz and it takes approximately 2.5μs to do so.

The Level 2 trigger is run on a dedicated CPU farm near to the detector. It takes the RoIs given to it from the L1 trigger but with the full detector granularity and combines them with information from the ID to use as inputs to fast reconstruction and decision algorithms. The increase in information makes this reconstruction more accurate. The L2 trigger reduces the event rate to around 5kHz and takes 40ms to do so.

The EF is also run on a dedicated CPU farm near to the detector, it takes the events passed to it from the L2 trigger and reconstructs them using the full detector information. The resultant reconstruction is similar to that of the "offline" reconstruction used in analyses. The EF reduces the event rate to 400Hz in about 4s and the events which pass this trigger are then recorded.

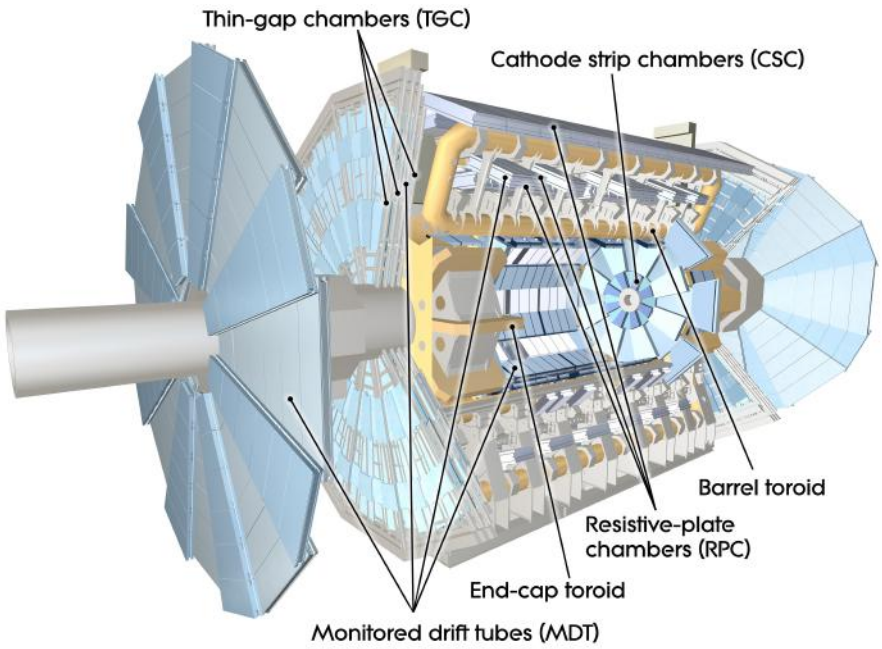

Figure 3.5.: The ATLAS muon system [46].

Many triggers are prescaled, this means that a fraction of the events that pass that trigger is recorded. Prescales are used to keep the event rate down to a recordable level. They can be different at each stage of the triggering, and usually the L1 trigger will have the highest prescale. When a trigger has been prescaled, its events will be given a weight so that the total distribution of events passing will be unbiased.

3.2.5. Luminosity

Luminosity is the number of events with cross-section σ that will occur per unit time, at the LHC it can be written as:

$$\mathcal{L} = \frac{R_{inel}}{\sigma_{inel}} \tag{3.2}$$

where $\mathcal{L}$ is the luminosity, R_{inel} is the inelastic collision rate and σ_{inel} is the pp inelastic cross-section. It has units of $\text{cm}^{-2}\text{s}^{-1}$.

The luminosity can also be written as follows:

$$\mathcal{L} = \frac{n_b f_r n_p^2}{2\pi\sigma_x\sigma_y} \tag{3.3}$$

where n_b is the number of bunches per beam, f_r is the rotation frequency of the beam, n_p is the number of protons per bunch and $\sigma_{x/y}$ is the width of the beam in the horizontal and vertical directions.

In ATLAS the luminosity is measured using a variety of sub-detectors and algorithms. There are two luminosity specific sub-detectors located in forward regions of the detector [47]. The calibration of the luminosity measurement is done using dedicated Van der Meer scans [48]. The total time-integrated luminosity that ATLAS recorded in 2012 is 21.3 fb^{-1} of which 20.3 fb^{-1} is "good for physics", however the amount used in the analysis in Chapter 5 is 19.5 fb^{-1}. This is due to a software bug in the b-jet triggers used in the analysis, which affected data recorded at the start of 2012.

3.3. Future Plans

In February 2013, the LHC turned off for two years, this was the end of Run 1 and the start of Long Shutdown 1 (LS1). During this time many improvements and fixes were made to both the LHC and ATLAS before restarting the beams again at an increased energy of $\sqrt{s} = 13$ TeV for Run 2, in June 2015. During Run 2 the LHC is expected to reach it's nominal energy and bunch spacing of $\sqrt{s} = 14$ TeV and 25 ns respectively, with peak instantaneous luminosity of $1.7 \times 10^{34}\text{cm}^{-2}\text{s}^{-1}$. Run 2 is scheduled to carry on until the end of 2018 where there will be another long shutdown (LS2) which will bring in more enhancements to the machines.

One of the main improvements to ATLAS that was applied during LS1 was the addition of an extra pixel layer, close to the beam pipe (33 mm from the beam-line), known as the Insertable B-Layer (IBL) [49]. It was added to ensure good vertexing and b-tagging in ATLAS despite the increased luminosity and pile-up, along with any problems that arise in the existing pixel detector due to radiation damage or hardware lifetime. Figure 3.6 shows a cosmic muon travelling through the ID of ATLAS in the x-y plane, taken before the start of collisions in Run 2, the IBL can be seen as the innermost circle, with the three layers around it being the rest of the Pixel sub-detector, and the 4 layers around those the SCT.

In the longer term future (∼2023) there are plans to upgrade the LHC further, one proposal is the High Luminosity LHC (HL-LHC) [50, 51] which would increase the design luminosity by a factor of 10 to 3000 fb^{-1}, allowing the accuracy of measurements and discovery potential to increase significantly.

The analysis in Chapter 6 is performed for the LHC running at $\sqrt{s} = 14$ TeV. The techniques used could be used during Run 2 of the LHC or the HL-LHC. The final results are presented for an integrated luminosity of 3000 fb^{-1}, so they show what could be achieved at the HL-LHC.

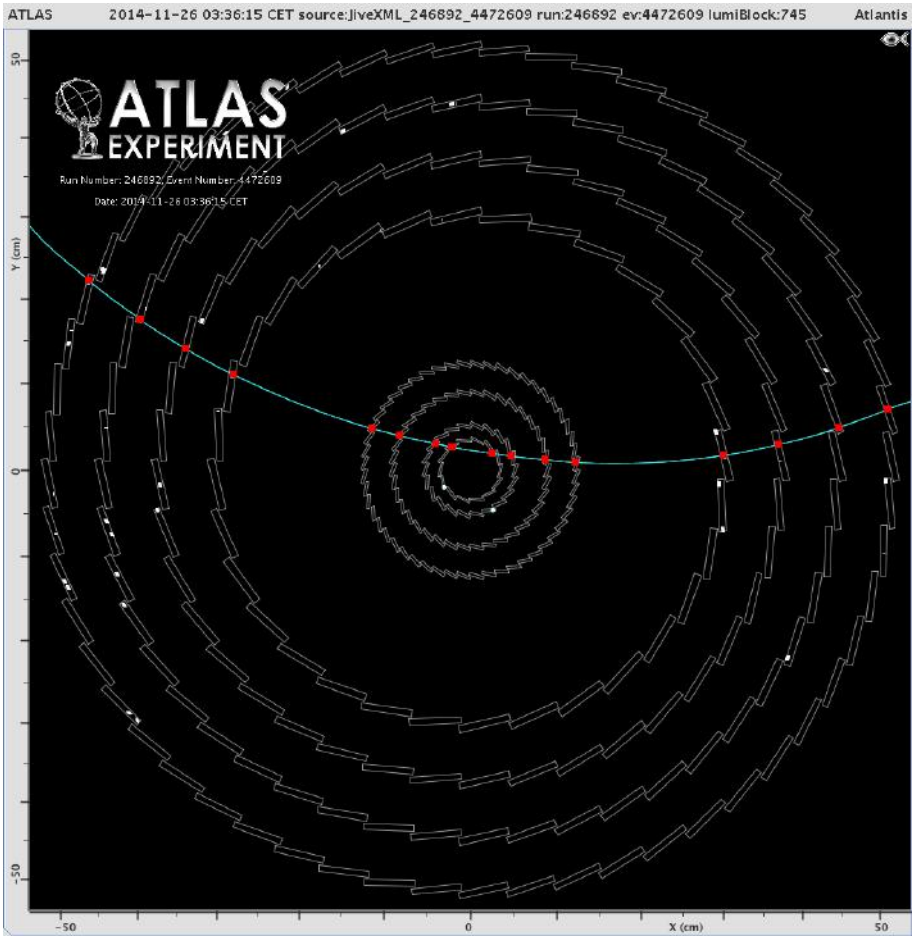

Figure 3.6.: An event display made with Atlantis showing a cosmic muon in the x-y plane of ATLAS. The pixel detector, including the IBL, and the SCT are shown.

Chapter 4.

Analysis Tools

4.1. Jets

When a quark or gluon is emitted from the hard process it quickly radiates and, due to colour confinement, hadronises into a shower of particles, which is what we can measure in the detector. Clustering algorithms are used to try to combine all the hadrons from one parton into an object which we call a 'jet', such that we can focus on the hard process.

4.1.1. Jet Reconstruction

It is important for clustering algorithms to return infrared and collinear safe jets, so that if a soft parton is added (infrared), or if a parton emits another parton at a small angle (collinear) the jets will be unaffected. One group of clustering algorithms which are infrared and collinear safe are sequential recombination algorithms. These algorithms work by iteratively combining an event's constituents, in the order of 'closest' first. In Monte Carlo simulation, an event's constituents would be the list of stable particles, in ATLAS these can be either tracks or groups of energy deposits in the calorimeter. Sequential recombination algorithms are defined by the following equations [52]:

$$d_{ij} = min(k_{ti}^{2p}, k_{tj}^{2p}) \frac{\Delta_{ij}^2}{R^2} \tag{4.1}$$

$$d_{iB} = k_{ti}^{2p} \tag{4.2}$$

where d_{ij} is the distance between two particles i and j, d_{iB} is the distance between a particle i and the beam B, $\Delta_{ij}^2 = (y_i - y_j)^2 + (\phi_i - \phi_j)^2$ and k_{ti}, y_i and ϕ_i are the transverse momentum, rapidity and azimuth of particle i, respectively, R is the radius parameter and p denotes which algorithm, with $p = -1, 0, 1$ giving the anti-k_t [52], Cambridge-Aachen [53], and k_t [54] algorithms respectively. The method is as follows:

1. Compute all distance parameters
2. Find the smallest distance parameter, if it is a ...
   a) d_{iB}: remove particle i from the list of particles and call it a jet
   b) d_{ij}: combine particles i and j into a single particle
3. Repeat steps 1 and 2 until no particles remain

The anti-k_t algorithm produces cone shaped jets by clustering lower p_{T} objects around a hard centre, it is widely used within ATLAS. The searches in Chapter 5 use anti-k_t jets with a radius parameter of 0.4 and Chapter 6 investigates the use of anti-k_t jets with many different radii. The Cambridge-Aachen algorithm uses a distance measure that is only dependent on the angular separation of particles, it produces somewhat irregularly shaped jets which are susceptible to pile-up and the underlying event but one can undo the final reclustering steps and look at the internal structure of the jet. In Chapter 6 the use of Cambridge-Aachen jets is investigated for reconstructing boosted Higgs bosons. The k_t algorithm clusters the lowest p_{T} particles first and as a result creates irregularly shaped jets which are very susceptible to the underlying event and pile-up due to the ill-defined jet area. k_t jets are good at resolving subjets. In Chapter 6 anti-k_t jets with a radius parameter of 0.2 are used to mimic track jets (defined below) in truth level MC.

Calorimeter Jets

The shower of hadrons produced from a quark or gluon originating from an interaction in ATLAS deposits its energy in the calorimeters. We can reconstruct jets, known as "calorimeter jets" [55], using clusters of the energy deposits as the input for the sequential reclustering algorithms. These are the most commonly used jets in ATLAS and all jets used in Chapter 5 are of this kind.

The topological clusters (topo-clusters) are formed using an iterative procedure which begins by finding seed cells with a signal, S, to noise, N, ratio above the threshold S/N = 4. Neighbouring cells which have S/N > 2 are added iteratively, along with their neighbours passing the same requirement. The final step is to add any remaining neighbours with S/N > 0.

Once all topo-clusters have been found in an event, local maxima within the topo-clusters are then searched for. A local maximum is a cell with $E_{cell} > 500$ MeV, $E_{cell} > E_{neighbours}$, and it must have at least 4 neighbours. If more than one local maxima is found then the topo-cluster is split, and the energy from shared cells is distributed according to weights which take into account the energies and distances of the local maximum to the shared cells.

Only positive energy topo-clusters are considered for jet reconstruction and, once assembled, the mass of the topo-cluster is set to 0 and the position is taken as the energy-weighted centre of the topo-cluster, before putting it into the sequential reclustering algorithm.

Track Jets

In addition to the calorimeter jets, there are also "track jets" [56]. These are jets where the input to the reclustering algorithms are tracks instead of calorimeter energy deposits. Only charged particles' tracks are recorded in ATLAS so these jets are not good for estimating the energy of the original parton. However, track jets are useful in identifying b-decays within boosted objects when used in tandem with large-R calorimeter jets. In Chapter 6 track jets, imitated by R = 0.2 anti-k_t jets in Monte Carlo, are used to identify highly boosted $h \to b\bar{b}$ candidates.

The conditions on which tracks can be used as input to the jet algorithms are: track $p_{\mathrm{T}} > 500$ MeV, there must be at least 1 hit in the pixel detector, 6 in the SCT, and the track must satisfy the impact parameter requirements of $d_0 < 1.5$ mm and $|z_0 \sin\theta| < 1.5$ mm.

4.1.2. Jet Calibration and Uncertainties

Jet calibration is done to correct mismeasurements in jet energies. Jets are originally reconstructed at the electromagnetic (EM) scale, such that all particles produced from EM showers are measured correctly, this leads to jets having too low a measured energy because hadronic showers have parts of their energy which are invisible to the detector, as well as parts of the shower escaping into dead regions of the detector or not being detected above the level of noise.

Jet calibration in ATLAS consists of four steps [57]:

1. Pile-up correction
2. Orgin correction
3. Jet calibration from MC simulations
4. Residual in-situ corrections

These steps are described below, with the 3^{rd} and 4^{th} points combined as the Jet Energy Scale (JES).

Jet Pile-up Correction

In a typical event there will be more than one proton-proton collision due to the proton beams containing bunches of protons. This is known as pile-up and it adds energy to the jets. To correct for this additional energy, an offset term is derived from MC and subtracted from the measured energy of a jet. This offset depends on the η of the jet as well as the number of collision vertices reconstructed in the event, N_{PV}, and the average number of bunch crossings per interaction, μ. The correction is tested using in-situ methods which exploit momentum balance in objects which are stable under pile-up (tracks jets and photons).

Jet Origin Correction

Jets are reconstructed assuming that they originate from the centre of the ATLAS detector, which is not normally true. A correction to jets is applied such that they point back to the collision point that they came from: the primary vertex. The primary vertex is defined as the vertex which has the largest value of Equation 4.3

$$p_{\mathrm{T}}^{vertex} = \sum_{i<n_{track}} p_{\mathrm{T}}^{track,i} \tag{4.3}$$

where the tracks are the tracks which come from that vertex. This improves the jet's angular resolution and slightly affects the jet p_{T} (< 1 % difference).

Jet Energy Scale

The JES is to make sure that the measured energy of the jet corresponds to the actual energy of the jet. A change in the JES will shift all jets energies in the same direction. Firstly, the jet response is calculated by geometrically matching truth jets to reconstructed jets in MC, this is done as a function of both the jet energy and η. After this correction has been applied, an additional η correction is applied. This correction is derived from in-situ techniques exploiting the momentum balance of a well defined object or group of objects and a jet, e.g. photon/Z($\rightarrow e^+e^-$) + jet events.

There are many terms which contribute to the uncertainty on the JES; these are applied as a set of variations on the simulated energy of jets, where each variation is the $\pm 1\sigma$ uncertainty of that particular source. There are 15 components for untagged jets with an additional one for b-tagged jets.

Jet Energy Resolution

The Jet Energy Resolution (JER) is to correct for the inaccuracy of the detector, which can shift the measured energy of the jet above or below its true value. Jets in MC have their energies smeared such that their JER matches that in data. The

resolution of the jet p_{T} can be described by the following functional form:

$$\frac{\sigma(p_T)}{p_T} = \frac{N}{p_T} \oplus \frac{S}{\sqrt{p_T}} \oplus C \tag{4.4}$$

where N is the noise term, S the stochastic term, and C the constant term [58]. The noise term includes electronics and detector noise along with contributions from pile-up, it is (relatively) independent of the jet p_{T} and dominates at low ($\sim$ 30 GeV) jet p_{T}. The stochastic term is for statistical fluctuations in the measured p_{T}, it is dominant at intermediate jet p_{T}. The constant term covers fluctuations that are a constant fraction of jet p_{T}. Two examples of this are signal lost to passive regions of the detector and non-uniforities of response across the calorimeters. The constant term dominates at high ($\sim$ 400 GeV) jet p_{T}.

The modelling of JER in MC is assessed by measuring the JER using in-situ methods which exploit momentum balance in dijet events. The uncertainty on the JER in MC is assessed by smearing each jets p_{T} by a random factor pulled from a Gaussian with a mean of 1 and a width that is a p_{T} and η dependent smearing factor. The smearing factor is the quadratic difference between the truth resolution plus the (p_{T} and η dependent) uncertainty on the resolution, and the truth resolution.

4.2. *b*-tagging

Identifying jets which originate from b-quarks is important to many analyses in ATLAS, not least the analysis presented in Chapter 5, because it helps to remove background events. b-hadrons have a few properties which can be used to discriminate b-jets from jets originating from other quarks or gluons. The first is their relatively long lifetime (typically $\sim$ 1.5ps) which means that they typically travel a few mm in the detector before weakly decaying which creates a displaced secondary vertex. The second is that typically there will be one or more tertiary vertex from the c-hadron decaying, and this should be in line with the primary vertex and secondary vertex.

In simulation, a jet is labelled a true b-jet if it contains a b-hadron with $p_T > 5$ GeV and $\Delta R < 0.3$ with respect to the jet axis. If a jet does not contain a b-hadron, but does contain a c-hadron with $p_T > 5$ GeV and $\Delta R < 0.3$ to the jet it is labelled as a c-jet. Similarly, if a jet contains neither a b- or c-hadron, but does contain a

τ with $p_T > 5$ GeV and $\Delta R < 0.3$ to the jet it is labelled a τ-jet. If a jet is not labelled as a b-, c-, or τ-jet, then it is labelled as a light-jet. These simulated jets are often referred to as "truth jets".

In data it is not possible to know whether a jet truthfully contains a b-hadron or not. However, one can use algorithms to assign a likelihood that a jet contains a b-hadron. These algorithms are known as "taggers" and they rely on the tracks which have been associated to each jet. Tracks must pass a set of quality cuts which are designed to select well-measured tracks and minimise the number of fake tracks, tracks from long lived particles, and tracks from material interactions. For a track to be associated to a jet it must also be within a certain angular separation of the jet axis which depends on the jet's p_{T}.

There are a few kinds of b-taggers. One relies on impact parameters which are the distance of closest approach between a track and the primary vertex. This is measured in the transverse direction, d_0, and the longitudinal, $z_0 \sin\theta$. Impact parameters are signed based on whether the track extrapolation crosses the jet direction in front of (positive) or behind (negative) the primary vertex. Tracks with positive impact parameters are more likely to come from the secondary vertex created by the b-hadron decay. Normally an impact parameter based tagger uses the impact parameter significance, e.g. d_0/σ_{d_0}, so that more weight is given to tracks that are measured precisely. One such example of an impact parameter based tagger used in ATLAS is IP3D [59].

Another type of b-tagger look for the secondary vertex resulting from the b-hadron's decay. One such example in ATLAS is the SV1 tagger [59], which reconstructs an inclusive vertex by adding in any two-track pairs that form a good vertex (and are not compatible with material interaction or long lived particle decays). It then iteratively removes the worst tracks until the χ^2 of the fit to the vertex is satisfactory. Variables derived from this vertex and the jet are then used in a likelihood ratio technique to distinguish between b-jets and other flavoured jets.

Another type of b-tagger assumes that the b-decay will be followed by a c-decay and that these should happen along a line connecting the primary vertex: the b-hadron flight path. Consequently, all charged particle tracks originating from the b- or c-decay should intersect this flight axis. JetFitter [60] is one such tagger used in ATLAS.

The b-tagging algorithm used in Chapter 5 is called MV1 [61]. It uses the output of the three taggers: IP3D, SV1 and JetFitterCombNN, as the input to a neural network, where JetFitterCombNN is itself a neural network using the outputs of the taggers SV1 and JetFitter. The b-tag weight used in Chapter 5 is 70%, this means that a cut is made on the output of the MV1 algorithm for which b-jets in $t\bar{t}$ events[1] had a 70% efficiency to pass. The corresponding efficiencies for c-jets and light jets to pass this cut are 20% and 1% respectively. In Chapter 6 b-tagging efficiencies of 70% are mimicked by giving jets a weight of 0.7/0.2/0.01 depending on their true flavour, and using the product of these as an event weight.

4.2.1. *b*-tagging Calibration and Uncertainties

The b-tagging efficiency for b-jets and the mis-tag rates for c/l-jets in simulation are scaled to that in data. The simulated jets are given a scale factor which corresponds to the ratio of the b-tagging efficiency in data over the efficiency found in MC [62]:

$$\kappa_{\epsilon_b}^{data/sim} = \frac{\epsilon_b^{data}}{\epsilon_b^{sim}} \tag{4.5}$$

The efficiency in data, ϵ_b^{data}, is estimated using a semileptonic $t\bar{t}$ sample, since each event contains two b-quarks and they can be selected with high purity. The scale factor is applied as an event weight, where the weight for each event is the product of the b-tagged jets' scale factors. For the data and MC samples in Chapter 5, the scale factors were estimated to be close to unity. The scale factors are dependent on the p_{T} and η of the jet. The scale factors are all close to unity, and can be seen in Figure 4.1.

The uncertainty on this calibration ranges from 2-8%, and is a combination of generator uncertainties, JES uncertainties and statistical uncertainties. For b-jets with $p_{\mathrm{T}} > 300$ GeV there is not enough data to derive a meaningful calibration so the scale factor is derived from simulation and a larger additional uncertainty is included. This reaches up to 24% for jets with $p_{\mathrm{T}} > 800$ GeV.

[1] which had $p_{\mathrm{T}} > 20$ GeV, $|\eta| < 2.5$ and if $p_{\mathrm{T}} < 50$ GeV, then JVF > 0.5

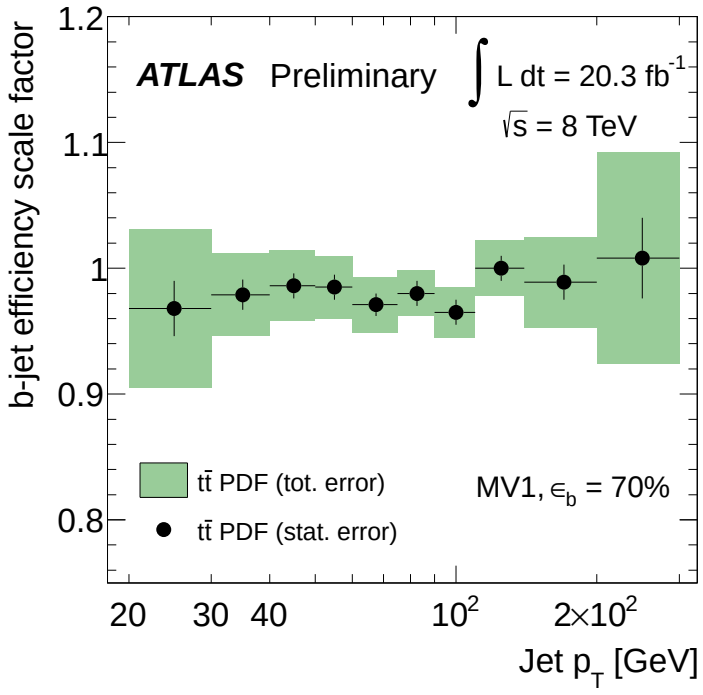

(a)

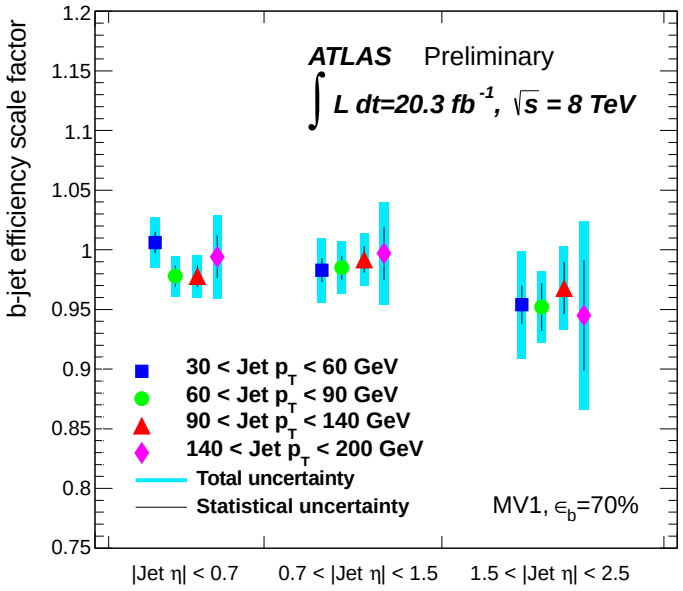

(b)

Figure 4.1.: The b-jet efficiency scale factors obtained for the MV1 b-tagging tool at the 70% b-jet efficiency working point. **(a)** As a function of jet p_{T}. **(b)** Binned in p_{T} and η. [62]

The uncertainties on the b-tagging calibration are applied in the analysis in Chapter 5 as 10 separate nuisance parameters, corresponding to the different jet p_{T} bins for the scale factors.

4.3. Monte Carlo

Monte Carlo (MC) methods are a way of generating numerical values from a probability distribution. In particle physics, MC generators are are used to simulate particle interactions. This simulated data can be used to model real and theoretical processes and provides predictions which can then be tested in real data. There are many different MC generators used in ATLAS analyses, and their results are constantly being tested against data from the LHC to make them more reliable.

The event generation method is as follows: firstly the hard process is generated by calculating the matrix element of that particular process at a fixed order (e.g. leading order (LO) or next-to-leading order (NLO)), and then using this along with a PDF set to numerically calculate the phase-space integral.

Any incoming or outgoing particles from the hard process which have colour charge will radiate gluons which in turn can radiate more gluons and pair-produce quarks, resulting in showers of partons. This is added to the hard process using a parton shower (PS) algorithm which adds partons from the energy scale of the hard process down to the scale of ~ 1 GeV.

Next the process of hadronization is simulated. This is where the coloured partons are confined into colourless hadrons. Finally, the underlying event is added, this is the interactions of the remaining constituents of the incoming particles (in ATLAS this would be protons).

For MC to be comparable with real data it must be run through a detector simulation. In ATLAS, GEANT [63, 64] is used for this. It simulates how the outgoing particles produced in the event generation would interact with the detector using information from test beams.

4.3.1. Examples of Monte Carlo Generators

There are many MC generators that can perform part or all of the event simulation. The generators used in this thesis are PYTHIA 8 [65], POWHEG [66–69], SHERPA [70] and MADGRAPH [71, 72].

PYTHIA 8

PYTHIA 8 is a leading order generator which uses transverse momentum (p_{T}) ordering when computing the parton shower, and the Lund string model [73] when dealing with the hadronisation.

POWHEG

POWHEG generates NLO matrix elements, this means that there are extra hard partons included in the ME then just the hard process. POWHEG samples are interfaced with a parton shower generator such as PYTHIA. By including the extra partons in the ME rather than the PS, one can get a more accurate treatment of events with multiple objects such as jets.

SHERPA

SHERPA is a multi-leg generator, meaning that it performs the Matrix Element and Parton Shower parts of the generation. It is a leading-order generator, but it takes into account Feynman diagrams with extra, hard partons in the process when calculating the ME. The showering in SHERPA is done using the dipole method where each branching process is considered a parton-pair (dipole) rather then a single parton emitting a soft parton. The hadronisation model used in SHERPA is the cluster model [74].

MADGRAPH

MADGRAPH is a leading-order Matrix Element generator. When used in this thesis, it is showered with PYTHIA 8.

Chapter 5.

A Search for $pp \to hh \to b\bar{b}b\bar{b}$ with ATLAS

This chapter focuses on the resolved search for resonant and non-resonant $pp \to hh \to b\bar{b}b\bar{b}$ described in Ref. [1][1], which was performed on 19.5fb^{-1} of data collected with ATLAS in 2012. Jets are reconstructed using the anti-k_t algorithm with a distance parameter R = 0.4. Events are selected where two boosted pairs of b-tagged jets can be found which have masses that are consistent with the Higgs boson mass and also pass a cut which is designed to remove $t\bar{t}$ events.

This analysis was based on an initial sensitivity study described in Ref. [75] and continues on from work presented in Ref. [76] (see also Section 5.6.2).

5.1. Data and Monte Carlo Samples

This analysis uses 19.5fb^{-1} of data collected in 2012 by the ATLAS detector at a centre-of-mass energy of 8 TeV.

Monte Carlo samples are used to model the signal samples and also the sub-dominant background of top-pair production, and the very small contribution to the background from Z+jets events. The main background in this analysis is QCD multijet events which are modelled using data.

[1]This paper presents two complementary approaches to Higgs boson reconstruction, "resolved" – where each b-quark from the Higgs boson decay is reconstructed into separate jets, and "boosted" – where both b-quarks are contained in one large radius jet.

The benchmark resonant signal sample is a spin-2 Randall-Sundrum Kaluza-Klein Graviton (G*), $pp \to G^* \to hh \to b\bar{b}b\bar{b}$, described in Section 2.2.1, with $k/\bar{M}_{Pl} = 1.0$ where $\bar{M}_{Pl}$ is the reduced Planck Mass. There are samples in the range from $500 < m_{G^*} < 1500$ GeV in 100 GeV intervals. There are also two other sets of samples with the values $k/\bar{M}_{Pl} = 1.5$ and $k/\bar{M}_{Pl} = 2.0$. The Graviton samples are generated with MadGraph v1.5.1 [71] with pythia v8.175 [65] for the underlying event modelling, parton showering and hadronisation. The PDFs used are CTEQ6L1 [77].

The other resonant signal is a spin-0 heavy neutral scalar boson, H, in the Two-Higgs Doublet Model (2HDM), $pp \to H \to hh \to b\bar{b}b\bar{b}$, described in Section 2.2.1. Again, eleven samples in the range from $500 < m_H < 1500$ GeV in 100 GeV intervals are used. The samples are generated with MadGraph v1.5.1 plus pythia v8.175 and the PDF set used is CTEQ6L1. These samples are generated in a simplified model with a fixed narrow width $\Gamma_H = 1$ GeV.

The non-resonant signal is the production of a pair of Standard Model Higgs bosons decaying to four b-quarks (SM hh): $pp \to hh \to b\bar{b}b\bar{b}$. This is generated with MadGraph v1.5.1 interfaced with pythia v8.175. The exact form factors for the top loop are taken from HPAIR [5,78]. The cross-section is $\sigma(pp \to hh \to b\bar{b}b\bar{b}) = 3.6 \pm 0.5$ fb, which is the NNLO gluon-fusion production cross-section from [7], summed with the NLO predictions for vector-boson-fusion, top-pair-associated and vector-boson-associated production from [79]. This is the inclusive cross-section. The PDFs used are CTEQ6L1.

The $t\bar{t}$ MC is generated with powheg v1.0 and showered with pythia v6.426. It is normalised to the next-to-next-to-leading order + next-to-leading log (NNLO+NLL) cross-section prediction of 252.89pb [80–85]. A reweighting is applied to the $t\bar{t}$ samples to correct for the top p_{T} spectra to be in agreement with the unfolded $\sqrt{s}$ =7 TeV ATLAS measurement [86].

The Z+jets sample is generated using Sherpa v1.4.3 [70] with the CT10 PDF set [87]. The Z boson decays to two b-quarks. The cross-section is scaled to a NLO powheg-box v1.0 [88] plus pythia v8.165 prediction.

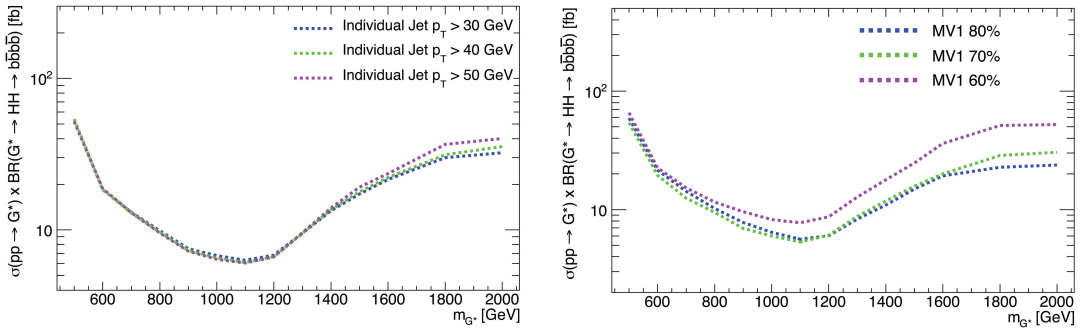

(a) **(b)**

Figure 5.1.: **(a)** The stat-only expected exclusion limits comparing different values of the minimum jet p_{T} for jets that make up the two dijets. **(b)** The stat-only expected exclusion limits comparing different working points of the MV1 b-tagging.

5.2. Event Selection

5.2.1. Cut Value Optimisation

All of the values of cuts in this analysis have been optimised in studies. The figure of merit used to optimise these cuts was the stat-only expected 95% exclusion limit for the $m_{G^*} = 500$ GeV, $k/\bar{M}_{Pl} = 1.0$ graviton sample. For the mass-dependent cuts, outlined in Section 5.2.5, the full mass range of the $k/\bar{M}_{Pl} = 1.0$ graviton samples was taken into account. Two examples of these stat-only expected limits can be seen in Figure 5.1.

5.2.2. Data Selection

For selection, data events must come from periods of time where the detector was running correctly. In addition to this, both data and MC events which contain a jet with $p_{\mathrm{T}} > 20$ GeV that fails the 'Looser' jet cleaning criteria outlined in Ref. [89] are vetoed. This is to avoid jets which result from detector noise, non-collision backgrounds and cosmic rays.

5.2.3. Triggers

After the initial data selection, both data and MC events are required to pass any of the following 5 triggers:

- **EF_2b35_loose_j145_j35_a4tchad**: requires a jet with transverse energy (E_{T}) greater than 145 GeVand 2 b-tagged jets with E_{T} greater then 35 GeV. One of the b-tagged jets can be the jet with E_{T} above 145 GeV.
- **EF_b45_medium_j145_j45_a4tchad_ht500**: requires a jet with E_{T} greater than 145 GeV and a b-tagged jet with E_{T} greater than 45 GeV. In addition to this, the scalar sum of the E_{T} of the jets in the event must be greater than 500 GeV.
- **EF_b45_medium_4j45_a4tchad_L2FS**: requires four jets with E_{T} greater than 45 GeV of which at least one is b-tagged.
- **EF_j360_a4tchad**: requires one jet with E_{T} greater than 360 GeV.
- **EF_4j80_a4tchad_L2FS**: requires 4 jets with E_{T} greater than 80 GeV.

These triggers did not have a prescale added to them so any event which passed one of them was recorded. The triggers are complementary to each other, and the overall efficiency relative to offline cuts for signal events that pass the preselection cuts described in Section 5.2.4 to also pass the OR of these triggers is high, estimated at 99% using the graviton $\to$ hh signal MC sample with $m_G = 500$ GeV. Figure 5.2 shows the predicted signal efficiencies for the individual triggers for the graviton samples. At high mass some of the trigger efficiencies are falling, there are two reasons for this. The first is that the increased boost of each Higgs boson causes the b-quarks to be emitted too close together to resolve into separate R = 0.4 jets, this can be seen in the multijet triggers. The second reason is that the higher masses are more likely to produce high p_{T} jets which have a lower b-tag efficiency. The predicted signal efficiencies for the 2HDM samples are all above 97% whilst the non resonant SM hh and $t\bar{t}$ MC are predicted at (99.2 $\pm$ 0.2)% and (99.3 $\pm$ 0.2)% respectively.

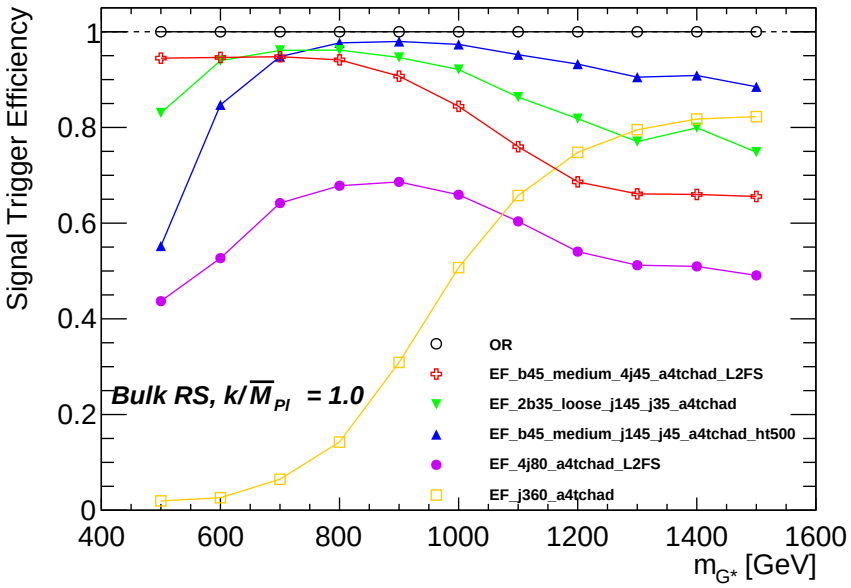

Figure 5.2.: The predicted signal efficiency relative to offline cuts for each mass point in the graviton $\to$ hh MC for each trigger.

5.2.4. Preselection

Together the cuts described below labelled 'Basic Kinematic Cuts' and '$t\bar{t}$ Veto' form the 'Preselection'.

Basic Kinematic Cuts

Jets are reconstructed with the anti-k_t algorithm with a radius parameter of 0.4, these jets are calibrated as described in Section 4.1.2. Any jets with a muon within $\Delta R < 0.4$ of the jet axis have the muon-in-jet correction applied. This is where the 4-vector of the muon is added to the jet and the estimated amount of energy that the muon deposited into the calorimeter is subtracted. This correction is to account for semi-leptonic decays of b-hadrons within the jet. For a muon to be eligible to be used in this correction it must be within the inner detector acceptance ($|\eta| < 2.5$) and pass a variety of quality cuts [90]. If multiple muons are matched to a jet, the muon closest to the jet axis is used. The effect of this correction can be seen in Figure 5.3 which shows the dijet mass ($m_{2\mathrm{j}}$) distribution in the graviton $m_G = 500$ GeV MC for jets with and without the correction. The $m_{2\mathrm{j}}$ distribution for the corrected jets has a better resolution.

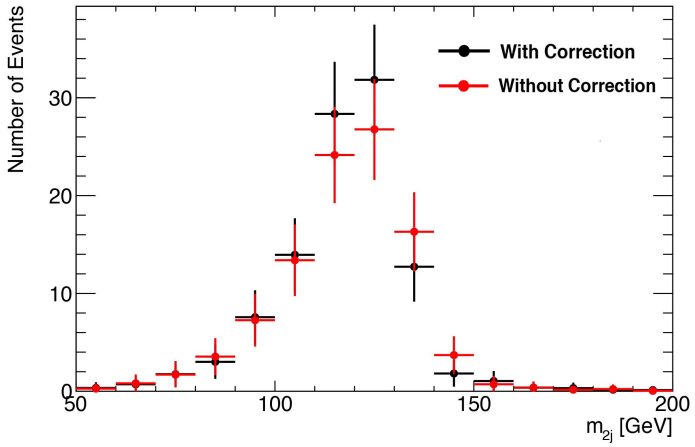

Figure 5.3.: The $m_{2\mathrm{j}}$ distribution in the graviton $m_G = 500$ GeV MC for jets with and without the muon-in-jet correction.

It was found that the minimum p_{T} of jets did not affect the sensitivity of the analysis, (see Figure 5.1a), so a cut of $p_{\mathrm{T}} > 40$ GeV was chosen as it is unlikely that jets with a greater p_{T} than this originate from pile-up or the underlying event. Jets are required to be b-tagged using the MV1 tagging algorithm with a working point that corresponds to 70% efficiency for b-jets. The 70% working point was chosen as it gives the analysis the best sensitivity at low mass (Figure 5.1b). b-tagging requires tracking information so jets are required to have $|\eta| < 2.5$. In addition to these cuts, if a jet has $|\eta| < 2.4$ and $p_{\mathrm{T}} < 50$ GeV, than it is required that at least 50% of the Σp_{T} of tracks matched to the jet come from tracks originating from the primary vertex. This is a "jet vertex fraction" cut (JVF) and it is used to remove any remaining jets that have a significant amount of energy coming from pile-up.

It is required that at least two dijets, made from pairing up and vectorially adding the 4-vectors of the four highest-p_{T} jets, can be found that satisfy the following criteria:

- Magnitude of the vectorial sum of the two jets momenta in the transverse plane $(\mathbf{p}_{\mathrm{jet1}} + \mathbf{p}_{\mathrm{jet2}})_{\mathrm{T}} > 200$ GeV for the leading dijet
- $(\mathbf{p}_{\mathrm{jet1}} + \mathbf{p}_{\mathrm{jet2}})_{\mathrm{T}} > 150$ GeV for the sub-leading dijet
- Angular separation of the jets $\Delta R_{\mathrm{jet1,jet2}} < 1.5$

Leading/sub-leading refer to the highest/second-highest dijet in p_{T}. In the case where a jet can be used to create more than one dijet which satisfies the above kinematic requirements then the dijet with the highest invariant mass is chosen. Again, the values for these cuts were optimised for the $m_{G^*} = 500$ GeV, $k/\bar{M}_{Pl} = 1.0$ graviton sample. The values for the p_{T} cuts are balanced between having a high enough cut that a lot of the large multijet background is eliminated and that a high trigger efficiency can be maintained for the lowest mass signals whilst they are low enough that the lowest mass signals have a good acceptance.

$t\bar{t}$ Veto

After the above selection, $t\bar{t}$ events make up about 20% of the background. Studies of truth MC show that the $t\bar{t}$ events passing these cuts are predominantly events where each top decays hadronically via $t \to bW \to bcs$, and the c-jet has been mistagged as a b-jet. To reduce this component of the background an additional kinematic cut is applied which vetoes events where a top candidate can be reconstructed.

Since tops mainly decay to three jets, extra jets from the event are used to reconstruct the mass of the W and the mass of the top when combined with the dijet. The mass of the W, m_W, is reconstructed by combining an extra jet and the jet with the lowest b-tag weight in the dijet and then taking the invariant mass. The mass of the top, m_t, is reconstructed by combining the dijet and an extra jet and then taking the invariant mass. Figure 5.4 shows the distributions of m_W and m_t in the $t\bar{t}$ MC and for various Graviton signal MC samples which show clear peaks in the $t\bar{t}$ sample. The 2HDM and SM hh distributions are very similar to the Graviton distributions. A cut is then made in the $m_W - m_t$ plane.

Extra jets are jets which are not used in the dijets and must satisfy:

- $|\eta| < 2.5$
- $p_{\mathrm{T}} > 30$ GeV
- if $|\eta| < 2.4$ and $p_{\mathrm{T}} < 50$ GeV, then JVF > 0.5
- Angular separation of the dijet and the extra jet, $\Delta R_{dijet,extrajet} < 1.5$

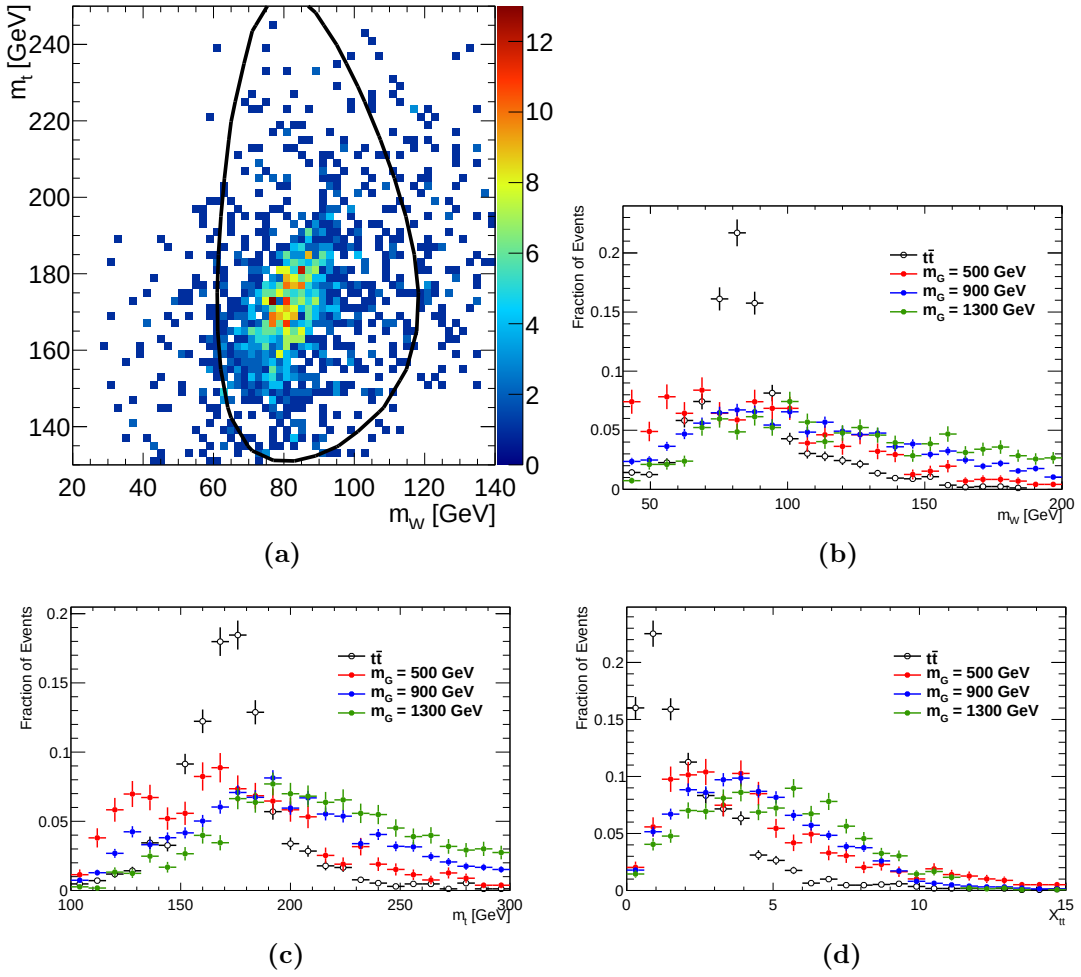

Figure 5.4.: **(a)** Distribution of m_t vs m_W for $t\bar{t}$ MC, also shown is the $X_{tt} = 3.2$ contour line (Equation 5.1). **(b)** The distribution of m_W for the graviton $\to$ hh, m_G = 500, 900, 1200 GeV and $t\bar{t}$ MC, **(c)** the distribution of m_t for the same samples and **(d)** the distribution of the ellipse value X_{tt} in these samples (one entry per event). Note that many of the signal MC events do not contain any extra jets and so are not plotted here (and pass the $t\bar{t}$ veto). These plots were made after applying the basic kinematic cuts from Section 5.2.4.

If an event doesn't have any extra jets that pass these cuts then it will pass the $t\bar{t}$ Veto. The compatibility of a three jet system to be from a top-quark is determined using the variable:

$$X_{tt} = \sqrt{\left(\frac{m_W - \tilde{m}_W}{\sigma_{m_W}}\right)^2 + \left(\frac{m_t - \tilde{m}_t}{\sigma_{m_t}}\right)^2}, \tag{5.1}$$

where m_W and m_t are the invariant masses of the W and top candidates, $\sigma_{m_W} = 0.1\, m_W$, $\sigma_{m_t} = 0.1\, m_t$, $\tilde{m}_W = 80.4\,\text{GeV}$ and $\tilde{m}_t = 172.5\,\text{GeV}$. The values of σ_{m_W} and σ_{m_t} reflect the dijet and three-jet system mass resolutions. If either dijet in an event has $X_{tt} < 3.2$ for any possible combination with an extra jet, the event is rejected. This requirement reduces the $t\bar{t}$ background by $\sim 60\%$, whilst retaining $\sim 90\%$ of signal events (shown as "$t\bar{t}$ Veto" in Fig 5.11).

5.2.5. Mass Dependent Cuts

A large range of resonance masses, $500 \leq m_X \leq 1500$ GeV, are considered for this search. The basic kinematic requirements described in Section 5.2.4 are optimised for the lowest resonance mass considered, but the optimum selection for higher masses differs from this. Figures 5.5 and 5.6 show distributions of the leading dijet p_{T}, sub-leading dijet p_{T} and the absolute difference in pseudorapidity between the dijets ($|\Delta\eta_{\text{dijets}}|$) for both multijet background and signal MC of various masses. These distributions show that for higher graviton masses it would be optimal to have harder requirements on the dijet p_{T}, and conversely, for the lower graviton masses, a tight cut on the pseudorapidity separation would improve sensitivity. For this reason, cuts which vary with the reconstructed resonance mass are used, hereafter referred to as "mass-dependent cuts" or "MDCs".

The MDCs were determined by finding the best stat-only expected limit for each mass point, for the $k/\bar{M}_{Pl} = 1.0$ graviton samples, using a three-dimensional scan of threshold values on the three different variables considered. For each variable the MDC was then made from linear fits to these best cuts in terms of the four-jet mass. These cuts are shown graphically as the red lines on Figure 5.7. The black points in these plots show the optimal value of the cut on that variable that for a graviton with a mass equaling $m_{4\text{j}}$.

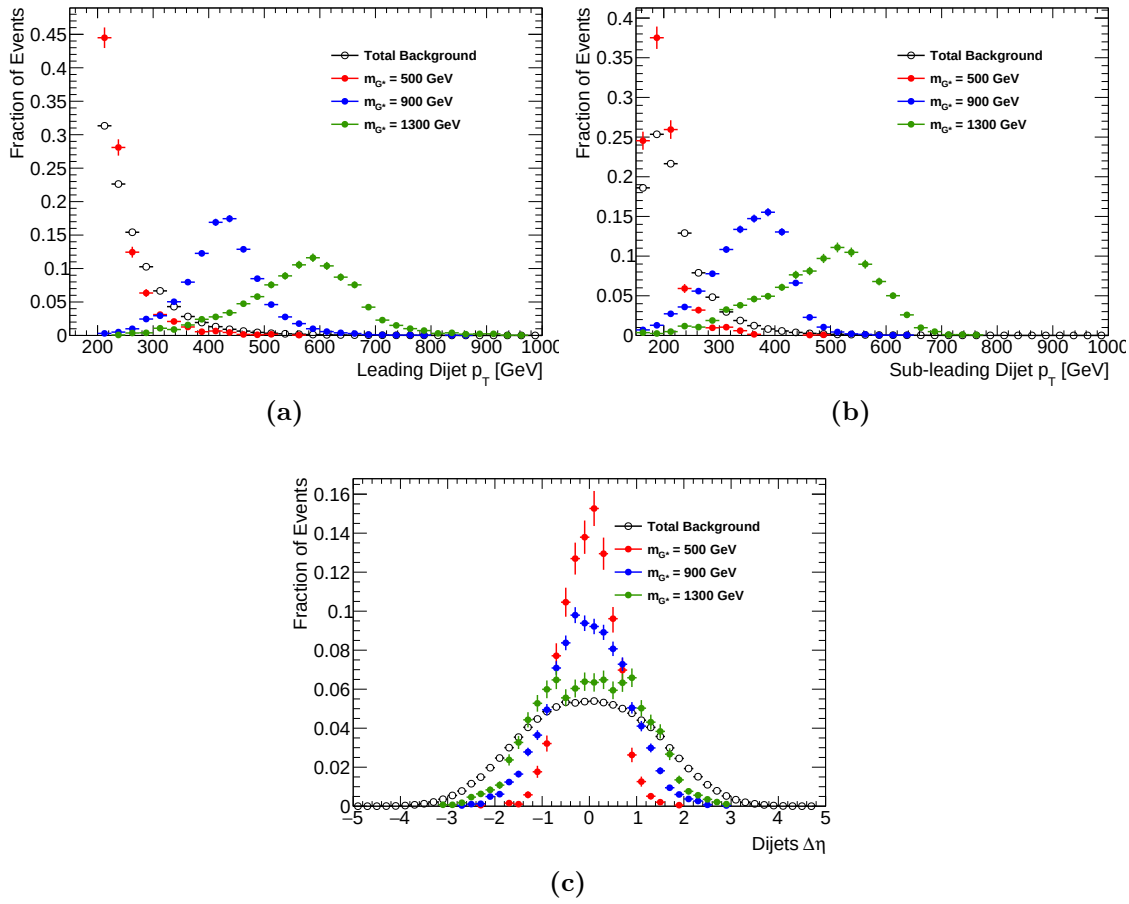

Figure 5.5.: The distributions of the variables which are used in the mass-dependent cuts for the total background and graviton MC samples. **(a)** The leading dijet p_{T}, **(b)** the sub-leading dijet p_{T}, **(c)** the absolute difference in pseudorapidity between the dijets ($|\Delta\eta_{\mathrm{dijets}}|$). These distributions are made after the preselection (Section 5.2.4)

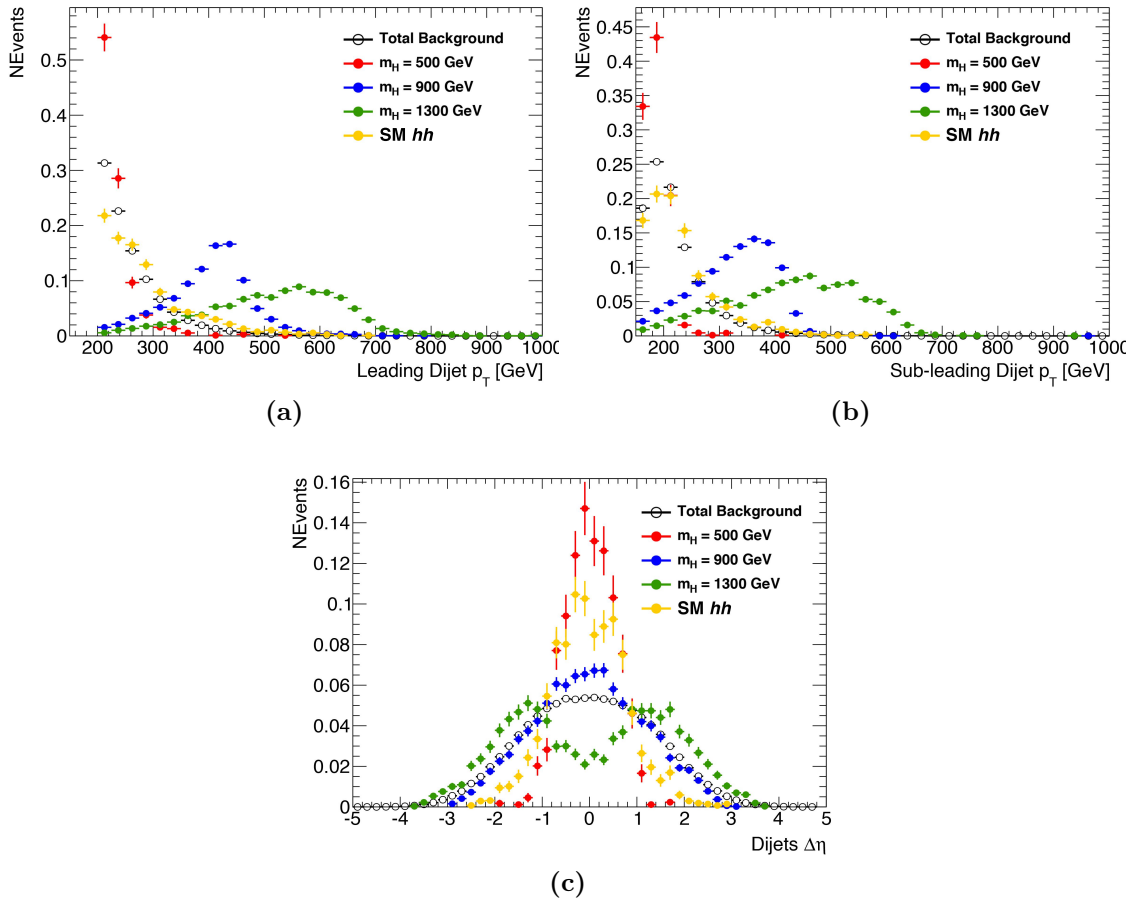

Figure 5.6.: The distributions of the variables which are used in the mass-dependent cuts for the total background, some 2HDM, and SM hh MC samples. **(a)** The leading dijet p_{T}, **(b)** the sub-leading dijet p_{T}, **(c)** the absolute difference in pseudorapidity between the dijets ($|\Delta\eta_{\mathrm{dijets}}|$). These distributions are made after the preselection (Section 5.2.4)

The MDCs are written in terms of the four-jet mass, $m_{4\mathrm{j}}$, expressed in GeV:

$$p_{\mathrm{T}}^{lead} > \begin{cases} 400 \text{ GeV} & \text{if } m_{4\mathrm{j}} > 910 \text{ GeV}, \\ 200 \text{ GeV} & \text{if } m_{4\mathrm{j}} < 600 \text{ GeV}, \\ 0.65 m_{4\mathrm{j}} - 190 \text{ GeV} & \text{otherwise}, \end{cases} \tag{5.2}$$

$$p_{\mathrm{T}}^{subl} > \begin{cases} 260 \text{ GeV} & \text{if } m_{4\mathrm{j}} > 990 \text{ GeV}, \\ 150 \text{ GeV} & \text{if } m_{4\mathrm{j}} < 520 \text{ GeV}, \\ 0.235 m_{4\mathrm{j}} + 28 \text{ GeV} & \text{otherwise}, \end{cases} \tag{5.3}$$

$$|\Delta\eta_{\mathrm{dijets}}| < \begin{cases} 1 & \text{if } m_{4\mathrm{j}} < 820 \text{ GeV}, \\ 1.55 \times 10^{-3} m_{4\mathrm{j}} - 0.27 & \text{otherwise}. \end{cases} \tag{5.4}$$

The 2HDM samples have a wider $|\Delta\eta_{\mathrm{dijets}}|$ distribution when compared with the graviton signal, due to this the $|\Delta\eta_{\mathrm{dijets}}|$ cut is less efficient for the 2HDM signal. For the case of the multijet and $t\bar{t}$ backgrounds, the mass-dependent cuts are applied after the reweighting procedure outlined in Section 5.3.2.

5.2.6. Signal Region Definition

We consider one signal region for $pp \to hh \to b\bar{b}b\bar{b}$ which is defined as a requirement on the leading and subleading dijet masses. It was treated as blind (despite the unblinding of a similar signal region in Ref. [76]) until we were satisfied with the background prediction, systematic uncertainties, and statistical procedure for the results. This means that we did not observe the number of events or any distributions including those events. The Signal Region is defined by an approximate elliptical cut in the dijet mass plane. The central values of the "ellipse", 124 GeV and 115 GeV, were chosen by finding the median values of dijet masses in the graviton signal MC samples, and these were found to be stable with the resonance mass. Figures 5.8

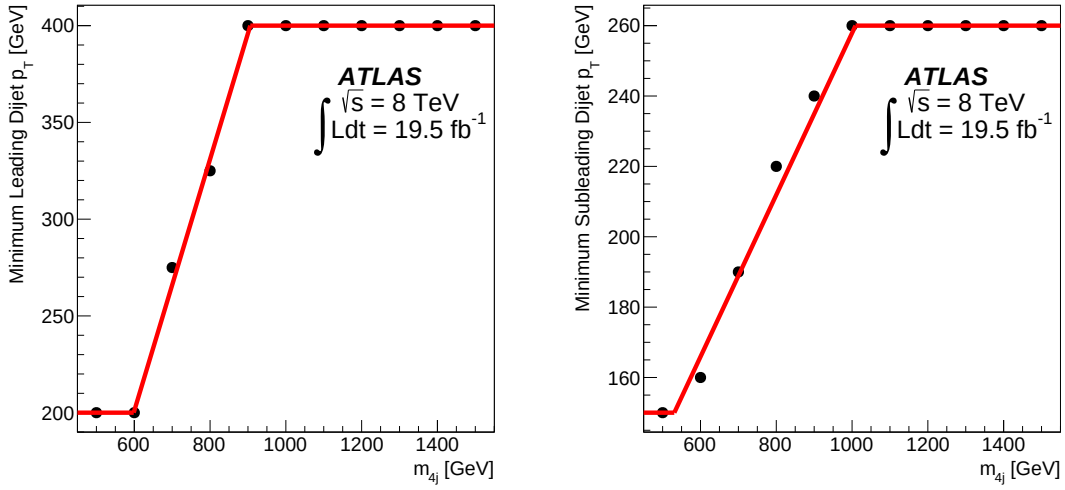

(a)

(b)

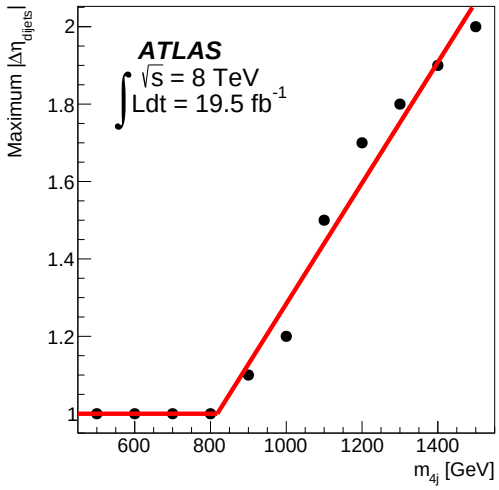

(c)

Figure 5.7.: The optimal cut value per graviton mass point for **(a)** the leading dijet p_{T}, **(b)** the sub-leading dijet p_{T}, **(c)** the absolute difference in pseudorapidity between the dijets. The red line shows the mass dependent cuts adopted as a function of the reconstructed $m_{4\mathrm{j}}$. These distributions are made after the preselection (Section 5.2.4)

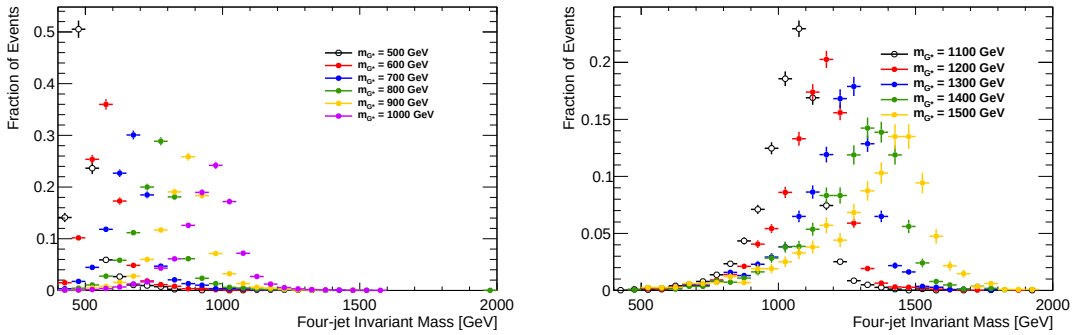

Figure 5.8.: The four-jet invariant mass distributions for the graviton → hh MC for the **(a)** 500 - 1000 GeV and **(b)** the 1100 - 1500 GeV mass points before the elliptical mass cut for the $k/M_{pl} = 1.0$ samples.

and 5.9 show the distribution of the four-jet invariant mass for the graviton, 2HDM H → hh and SM hh MC for the different mass points before the elliptical mass cut.

The definition of the approximate ellipse is:

$$X_{hh} = \sqrt{\left(\frac{m_{2\mathrm{j}}^{\mathrm{lead}} - 124\ \mathrm{GeV}}{0.1\, m_{2\mathrm{j}}^{\mathrm{lead}}}\right)^2 + \left(\frac{m_{2\mathrm{j}}^{\mathrm{subl}} - 115\ \mathrm{GeV}}{0.1\, m_{2\mathrm{j}}^{\mathrm{subl}}}\right)^2}, \tag{5.5}$$

where the $0.1\, m_{2j}$ terms represent the widths of the leading and sub-leading dijet mass distributions. The Signal Region is defined as $X_{hh} < 1.6$, it can be seen in Figure 5.10b as the area inside the inner black contour line.

The distribution of X_{hh} for some signal samples and $t\bar{t}$ MC is shown in Figure 5.10, along with the 2-D distribution of the individual dijet masses for 500 GeV resonances. It can be seen that the X_{hh} distribution does not vary significantly with graviton mass, and so there is no need to optimise this cut as a function of graviton mass. The 2HDM and SM hh signal samples have similar distributions. This cut removes ∼95% of the (multijet dominated) background whilst keeping an average signal efficiency of ∼60%.

The acceptance times efficiency ($A \times \varepsilon$) at each stage of the event selection for the resonant MC samples as a function of resonance mass can be seen in Figure 5.11. Two differences between the two signal samples can be seen in this figure, both of these originate from the difference in the spins of the resonances which causes them to have dissimilar angular distributions for their decay products. The spin-0 H has

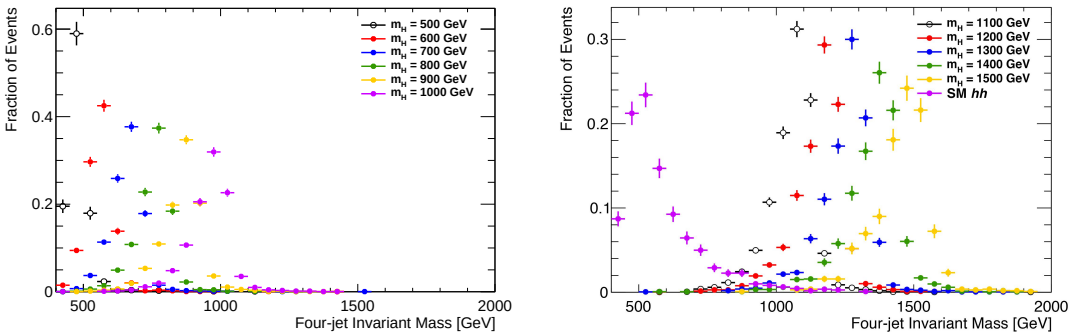

Figure 5.9.: The four-jet invariant mass distributions for the 2HDM H → hh MC for the **(a)** 500 - 1000 GeV and **(b)** the 1100 - 1500 GeV mass points before the elliptical mass cut. **(b)** also contains the SM hh MC sample.

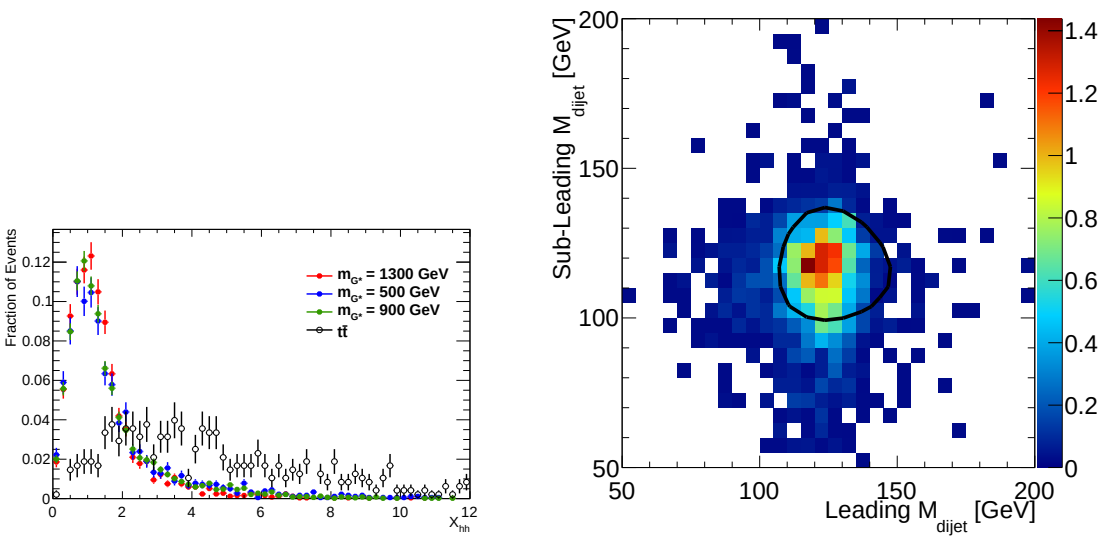

Figure 5.10.: **(a)** The X_{hh} distribution of graviton → hh signal samples of three different masses and $t\bar{t}$ MC, and **(b)** the 2-D distribution of leading dijet mass versus sub-leading dijet mass for the 500 GeV $G^* \to hh \to b\bar{b}b\bar{b}$ sample along with the $X_{hh} = 1.6$ contour line. Both distributions are shown before any cut on X_{hh}.

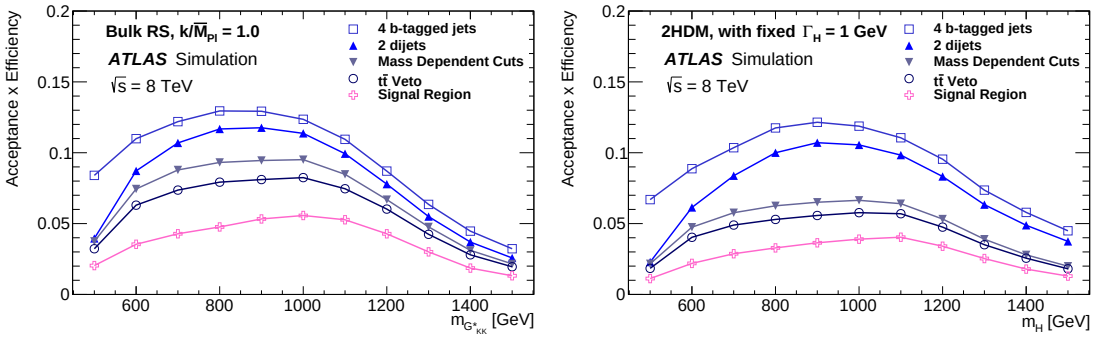

Figure 5.11.: The acceptance times reconstruction and selection efficiency for resonant signal events at each stage of the event selection for **(a)** the $G^* \to hh \to b\bar{b}b\bar{b}$ samples, shown for $k/M_{pl} = 1.0$, and **(b)** the 2HDM $H \to hh \to b\bar{b}b\bar{b}$ samples.

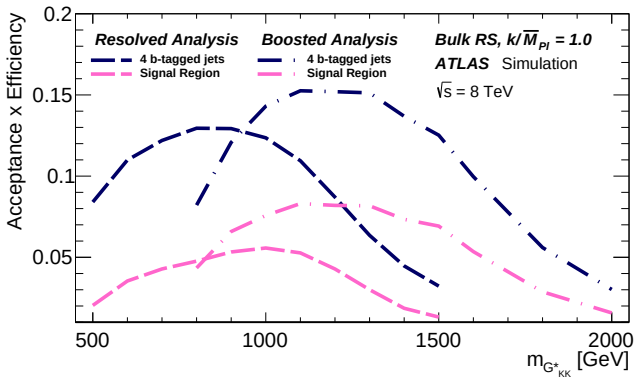

Figure 5.12.: Acceptance times reconstruction and selection efficiency as a function of graviton mass for the resolved and boosted analyses. The shapes of the curves are driven by the separation between the b-quarks from the Higgs boson decays and the impact on jet clustering.

a softer Higgs boson p_{T} spectrum than the spin-2 graviton, this leads to a lower acceptance for the basic kinematic cuts at low resonance mass. The H also has a lower MDC acceptance when compared with the graviton for $m_X \geq 700$ GeV due to the $|\Delta\eta_{\mathrm{dijets}}|$ cut. For both samples the efficiency drops at low resonance mass due to the p_{T} requirement on the fourth jet of 40 GeV. Also, there is a loss of efficiency at high m_X due to the boost of each Higgs boson causing the b-quarks to end up too close together to be resolved into two b-tagged jets - a second analysis which focussed on large radius jets to try to capture these boosted events can be found in the same paper [1]. Figure 5.12 shows how the two analyses compliment each other. Table 5.1 shows the $A \times \varepsilon$ for the non-resonant SM hh sample.

Requirement	$A \times \varepsilon$ [%]
4 b-tagged jets	4.9
2 dijets	1.5
MDC	1.2
$t\bar{t}$ Veto	1.0
$X_{hh} < 1.6$	0.60

Table 5.1.: The acceptance times efficiency ($A \times \varepsilon$) for the non-resonant SM hh signal model.

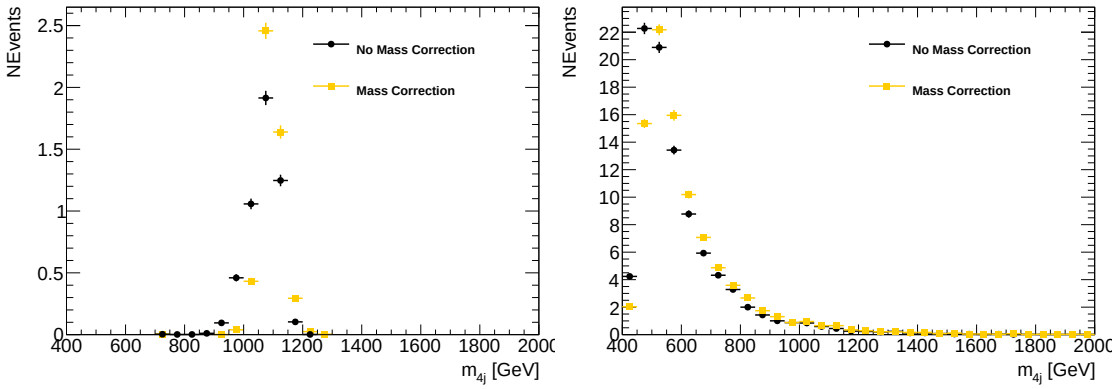

Figure 5.13.: $m_{4\mathrm{j}}$ distributions showing the effect of the mass rescaling, shown for **(a)** an $m_H = 1100$ GeV heavy neutral scalar boson sample and **(b)** the total background.

5.2.7. Mass Rescaling

In the resonant Higgs boson pair production searches, the final step of the search is to perform a fit to the four-jet mass in the Signal Region. The better the resolution of $m_{4\mathrm{j}}$, the better the sensitivity of this fit. To improve the resolution of $m_{4\mathrm{j}}$ the four-momenta of the dijets are scaled so that the mass of each dijet becomes m_h. The scale factor is $\alpha_{dijet} = m_h/m_{dijet}$. By doing this there is an improvement of $\sim 30\%$ in the signal $m_{4\mathrm{j}}$ resolution, whilst there is negligible effect on the background, this can be seen in Figure 5.13.

5.3. Background Estimation

There are two main backgrounds after the event selection described in Section 5.2: QCD-produced multijets and $t\bar{t}$. The multijet background comprises 94% of the total background and is modelled using a fully data-driven approach. The $t\bar{t}$ background comprises 6%, a data-driven approach is used to estimate the normalisation, and MC is used to estimate the shape. There is a small ($< 1\%$) Z+jets background which is estimated using MC. Non-resonant electroweak production of $ZZ \to b\bar{b}b\bar{b}$ is not considered in this analysis because using truth MC it was estimated that $\ll 1$ fb would pass our event selection. All of the methods to estimate our backgrounds are described in this chapter.

5.3.1. Z+jets Background

The predicted shape and normalisation of the $Z \to b\bar{b}$ +jets background is taken from the PYTHIA 8 MC sample described in Section 5.1. The PYTHIA 8 predicted cross-section is used, but after scaling with a k-factor of $2.02/1.25 = 1.62$, which was determined from the ratio of the POWHEG +PYTHIA 8 NLO+PS cross-section for boosted $Z \to b\bar{b}$ production (Z $p_{\mathrm{T}} > 200$ GeV) to that predicted by this sample. This background is very small - it contributes 0.5% to the total background, as can be seen in Table 5.5

5.3.2. Multijet Background

The multijet background is modelled using a fully data-driven method. The data used pass the trigger and preselection requirements described in Sections 5.2.3 and 5.2.4 with the exception of the offline b-tagging requirement: only one of the dijets has to consist of b-tagged jets. This "2-tag" selection yields a data sample of 485377 events, of which 98% are multijet events and the remaining 2% are $t\bar{t}$ (estimated from $t\bar{t}$ MC). The normal "4-tag" selection will be referred to as the data.

The multijet background is estimated before applying the mass-dependent cuts (Section 5.2.5). This is because before the multijet sample has been reweighted (Section 5.3.2) the distribution of the reconstructed mass of the four selected jets is

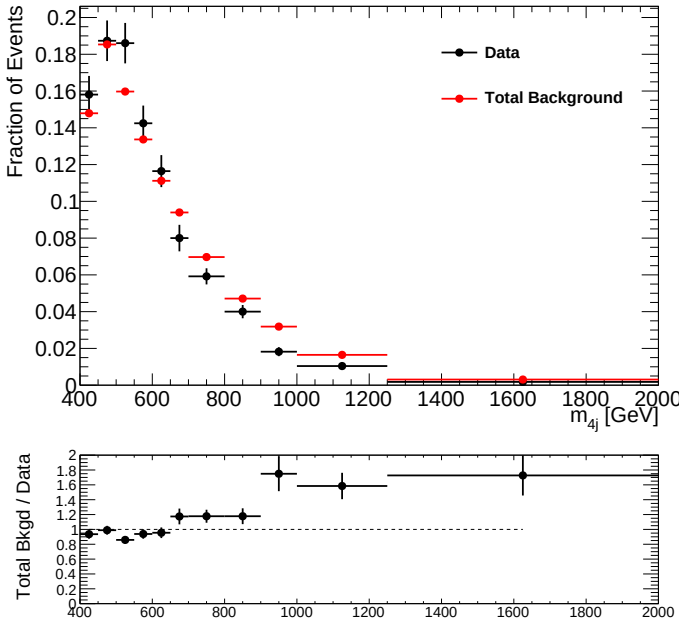

Figure 5.14.: The m_{4j} distribution shown for the data and the total background in the Sideband Region before reweighting and mass-dependent cuts (Section 5.2.5). The data is the 4-tag data, whilst the total background is the sum of the 2-tag data (which has been normalised to the 4-tag data in the Sideband Region using Equation 5.7), $t\bar{t}$ MC and Z+jets MC)

different between the 4-tag and 2-tag data (see Figure 5.14). Since the MDCs rely on this variable, applying them before the reweighting would introduce a bias between the two sets.

Regions of the Multijet Background

To estimate the normalisation and shape of the multijet background, the sample is split into three different regions, mapped out in the m_{2j}^{lead}-m_{2j}^{subl} plane. These regions can be seen in Figure 5.15. The innermost region is the Signal Region described in Equation 5.5. The events around the Signal Region are divided by the circle corresponding to Equation 5.6 which has a radius such that the two regions are of roughly equal statistics.

$$\sqrt{(m_{2j}^{\text{lead}} - 124.0)^2 + (m_{2j}^{\text{subl}} - 115.0)^2} = 58 \text{ GeV} \tag{5.6}$$

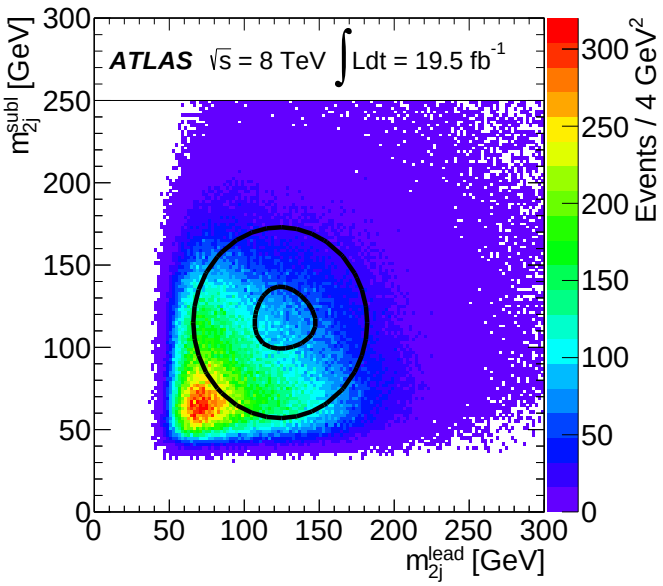

Figure 5.15.: The distribution of the subleading dijet mass, m_{2j}^{subl}, vs the leading dijet mass, m_{2j}^{lead}, for the 2-tag data sample used to model the multijet background. The Signal Region is the area surrounded by the inner black contour line, centred on $m_{2j}^{lead} = 124$ GeV, $m_{2j}^{subl} = 115$ GeV. The control region is the area inside the outer black contour line, excluding the Signal Region. The sideband region is the area outside the outer contour line.

The region outside the circle, known as the "Sideband Region", is where the normalisation and shape corrections to the multijet background are set. The region inside the circle, excluding the Signal Region, is known as the "Control Region", and is used to test the predictions made in the Sideband Region.

Multijet Normalisation

The normalisation of the multijet background prediction is set by scaling the number of events in each region of the 2-tag sample by the following factor, μ_{QCD}, calculated in the sideband region:

$$\mu_{\text{QCD}} = \frac{N_{\text{QCD}}^{4-\text{tag}}}{N_{\text{QCD}}^{2-\text{tag}}} = \frac{N_{\text{data}}^{4-\text{tag}} - N_{t\bar{t}}^{4-\text{tag}} - N_{Z}^{4-\text{tag}}}{N_{\text{data}}^{2-\text{tag}} - N_{t\bar{t}}^{2-\text{tag}} - N_{Z}^{2-\text{tag}}}, \tag{5.7}$$

where $N_{\text{data}}^{2-/4-\text{tag}}$ is the number of events in the Sideband Region in the 2- or 4-tag data sample respectively, $N_{t\bar{t}}^{2-/4-\text{tag}}$ and $N_{\text{Z+jets}}^{2-/4-\text{tag}}$ are the number of $t\bar{t}$ and Z+jets

events in the 2-/4-tag selected Sideband Region predicted by the data-driven $t\bar{t}$ (described in Section 5.3.3) and Z+jets MC samples respectively.

To predict the distributions of the multijet background, first, the predicted 2-tag distributions of Z+jets and $t\bar{t}$ are subtracted from the 2-tag data sample's distribution, and this distribution is then scaled by μ_{QCD}. This subtraction accounts for the varying level of $t\bar{t}$ and Z+jets contamination in each 2-tag region.

Multijet Shape

Figure 5.16 shows comparisons of the total background (multijet + $t\bar{t}$ + Z+jets) distribution and data in various kinematic variables in the Sideband Region, prior to the MDCs. As explained in the previous section, the data and total background distributions have equal area by construction.

One can see systematic differences between the total background and data distributions. Since the total background is multijet dominated, these differences can be attributed to the differing b-tagging requirements. The b-tagging algorithm's efficiency is dependent on jet p_{T} and $|\eta|$. For example, at higher jet p_{T} the algorithm is less efficient, this is reflected in the p_{T} spectrum of the jets which is harder for the multijet background. This is the main source of the difference, but there is also a contribution from the differing flavour compositions of the dijets. In order to correct for the limitations of the multijet sample we apply a reweighting procedure on the kinematics using a 1^{st} order polynomial fit to the ratio of the total background to the data in the Sideband Region using three kinematic variables:

- The leading dijet p_{T} (Figure 5.16a).
- The ΔR separation of the jets in the sub-leading dijet (Figure 5.16d).
- The ΔR separation of the dijets (Figure 5.16e).

The reweighting is done using 1-D distributions, but it is iterated three times such that correlations between the three variables are taken into account. Figure 5.17 shows the fit to the weights as a function of each variable in the first iteration of the reweighting. Figure 5.18 shows the evolution of the weights for the leading dijet p_{T} variable. The total weight applied to the event is the product of three weights, one from each variable. These weights are calculated for each event by taking the value

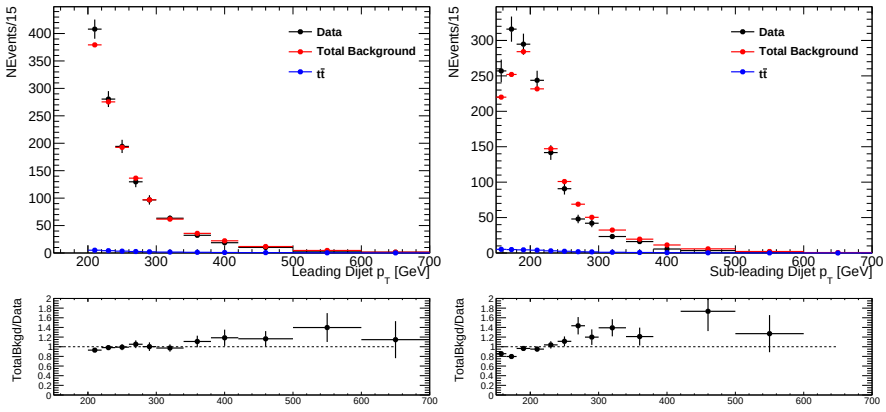

(a) Lead dijet p_{T}

(b) Sub-leading dijet p_{T}

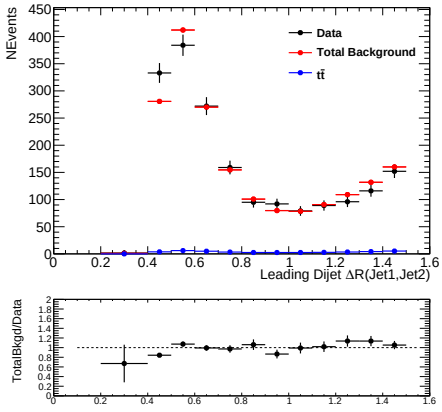

(c) Lead dijet jet-jet ΔR

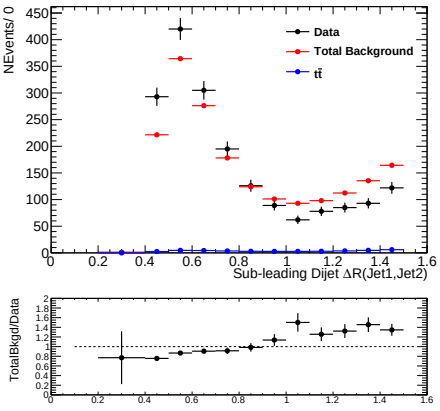

(d) Sub-leading dijet jet-jet ΔR

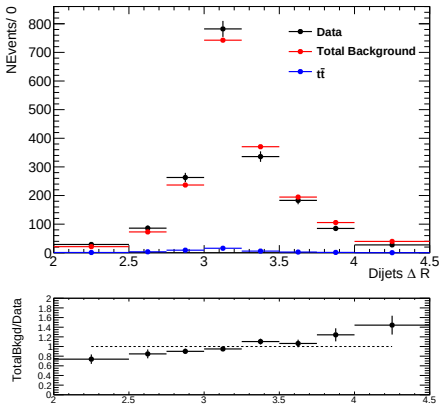

(e) ΔR separation of the dijets

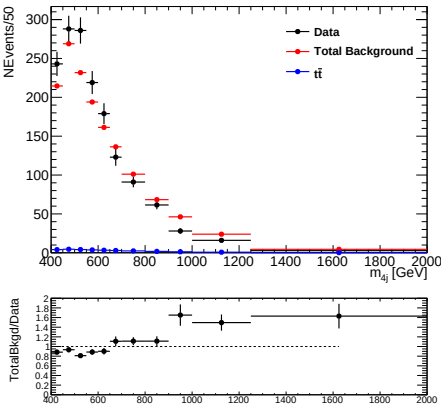

(f) $m_{4\mathrm{j}}$

Figure 5.16.: A comparison of the total predicted background to the data in the Sideband Region for various kinematic variables, prior to any reweighting of the multijet sample or MDCs. The small $t\bar{t}$ contribution to the total background is also shown.

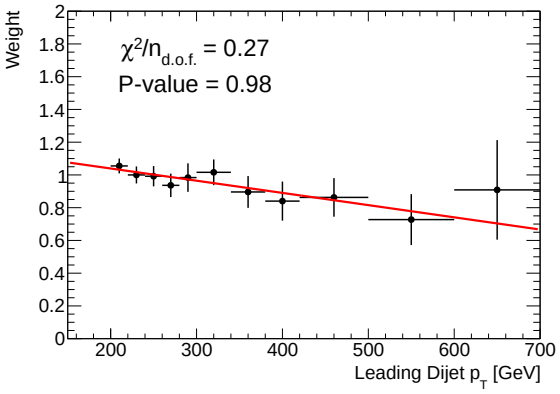

(a) Lead dijet p_{T}

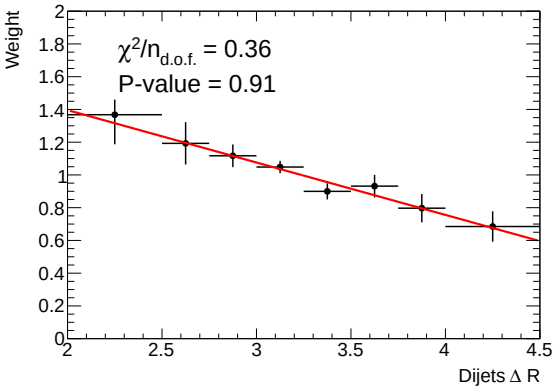

(b) The ΔR separation of the dijets

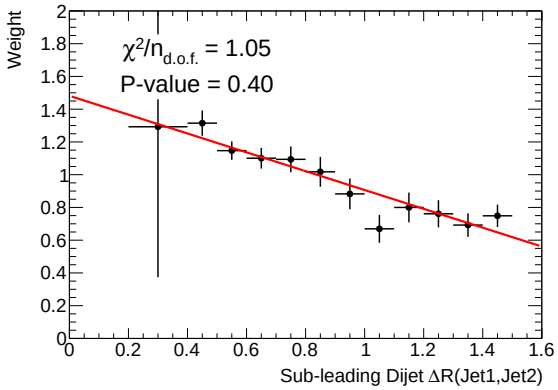

(c) The ΔR separation of the jets in the sub-leading dijet

Figure 5.17.: The weights applied for each reweighting variable in the first iteration of the reweighting. These are, by construction, the inverse of the TotalBkgd/Data ratios shown in Figures 5.16a, 5.16d and 5.16e.

of the fit at the value for the reweight variable. After the reweighting the multijet sample is scaled again to the data in the Sideband Region using Equation 5.7.

Figures 5.19 and 5.20 shows comparisons of the total background distribution and data in various kinematic variables in the Sideband Region after this reweighting has been performed, and also after the MDCs have been applied. One can see that the ratio of the total background to data in Figures 5.19a, 5.19d and 5.19e is close to unity, as expected. The other kinematic variables show good agreement between the total background and data. In particular, the $m_{4\mathrm{j}}$ distribution shown in Figure 5.20f is well reproduced.

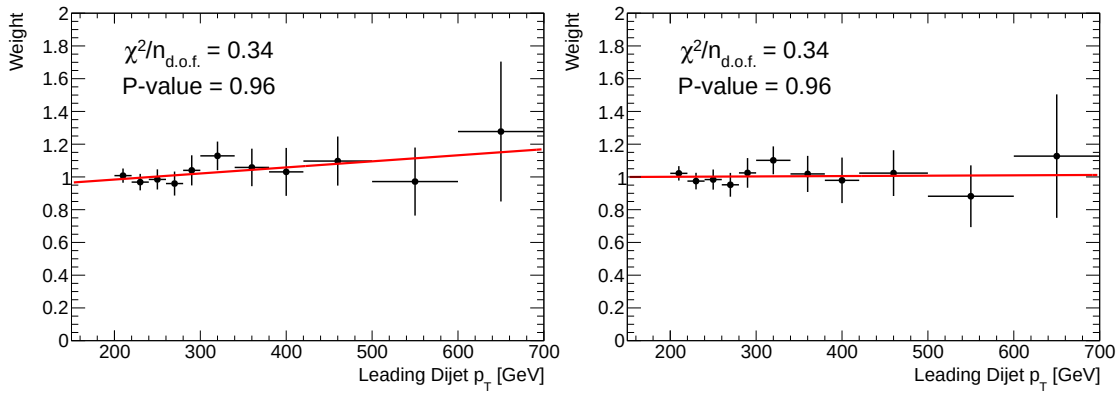

(a) After the second iteration **(b)** After the third iteration

Figure 5.18.: The weights applied for the lead dijet p_{T} reweighting variable after the second and third iterations of the reweighting.

Testing the Multijet Prediction in the Control Region

The Control Region can be used to test our multijet background prediction since it is orthogonal to the Sideband Region, has a low $t\bar{t}$ contamination, and is close to the Signal Region.

Table 5.2 shows the number of predicted background events from QCD-produced multijet, $t\bar{t}$ and Z+jets after the preselection in the Sideband Region and in the Control Region, after the mass dependent cuts have been applied. The total number of predicted background events and the number of events in the data are also shown. In the Sideband Region these numbers agree well by construction (due to the multijet normalisation coming from this region before the MDCs). One can also see that they agree very well in the Control Region - well within the statistical uncertainty on the data. In addition to the multijet background cross-checks analysis described later in Section 5.4, this agreement will be used to inform the multijet normalisation uncertainty (Section 5.5.2).

Figure 5.21 shows comparisons of the total background distribution and data in various kinematic variables in the Control Region. One can see that the level of agreement between the total background and the data is in general very good, indicating that the transportation of the multijet background prediction from the Sideband Region to the Control Region has been successful. Later in Section 5.4 we

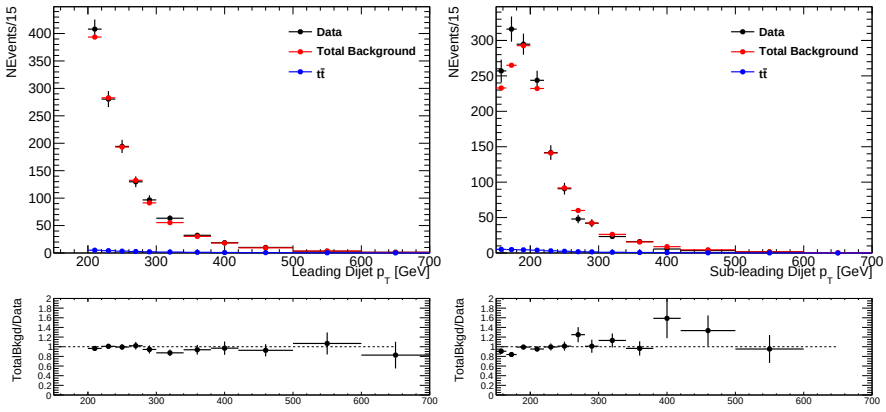

(a) Lead dijet p_{T}

(b) Sub-leading dijet p_{T}

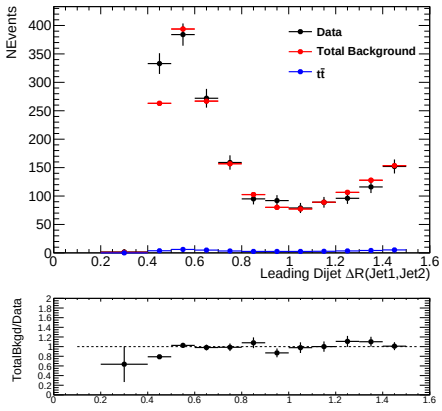

(c) Lead dijet jet-jet ΔR

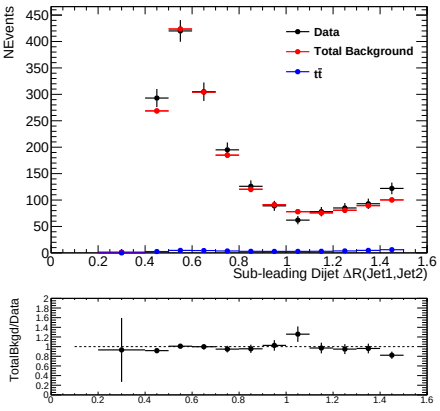

(d) Sub-leading dijet jet-jet ΔR

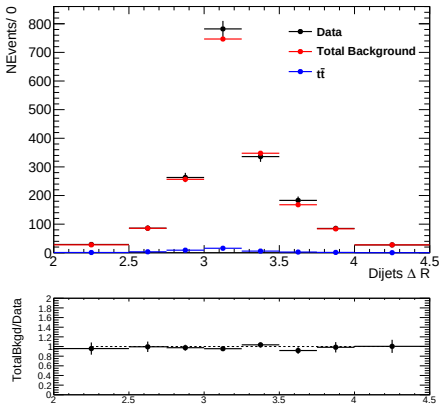

(e) ΔR separation of the dijets

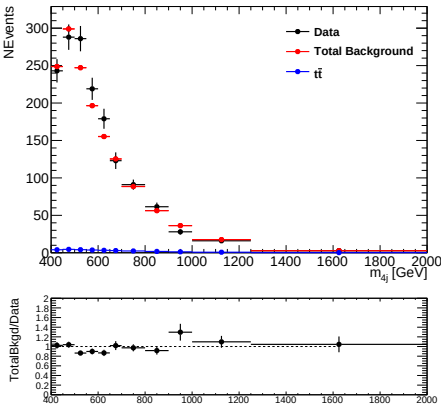

(f) $m_{4\mathrm{j}}$

Figure 5.19.: A comparison of the total predicted background to the data in the Sideband Region for various kinematic variables, after reweighting the multijet sample, prior to the MDCs. The small $t\bar{t}$ contribution to the total background is also shown.

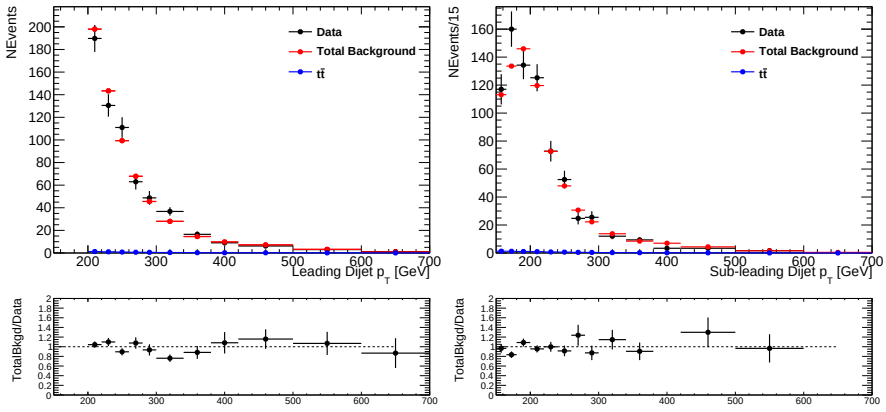

(a) Lead dijet p_{T}

(b) Sub-leading dijet p_{T}

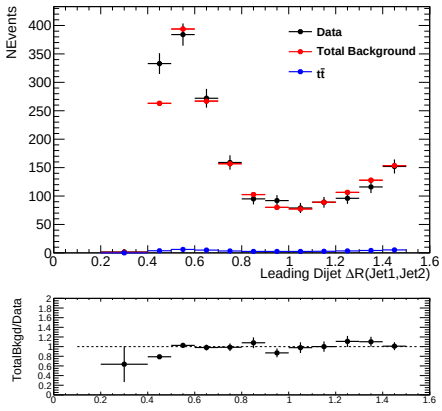

(c) Lead dijet jet-jet ΔR

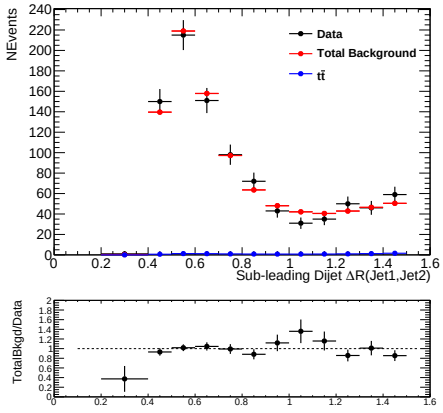

(d) Sub-leading dijet jet-jet ΔR

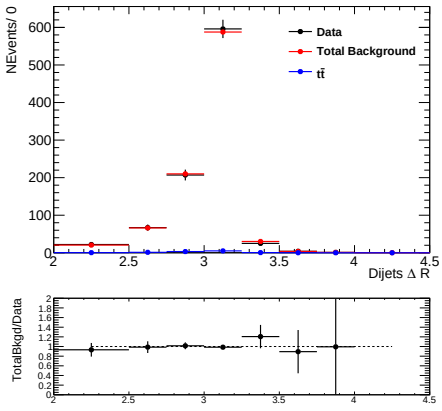

(e) ΔR separation of the dijets

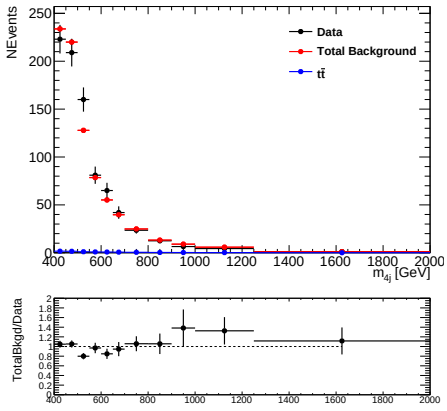

(f) $m_{4\mathrm{j}}$

Figure 5.20.: A comparison of the total predicted background to the data in the Sideband Region for various kinematic variables, after reweighting the multijet sample, after the MDCs. The small $t\bar{t}$ contribution to the total background is also shown.

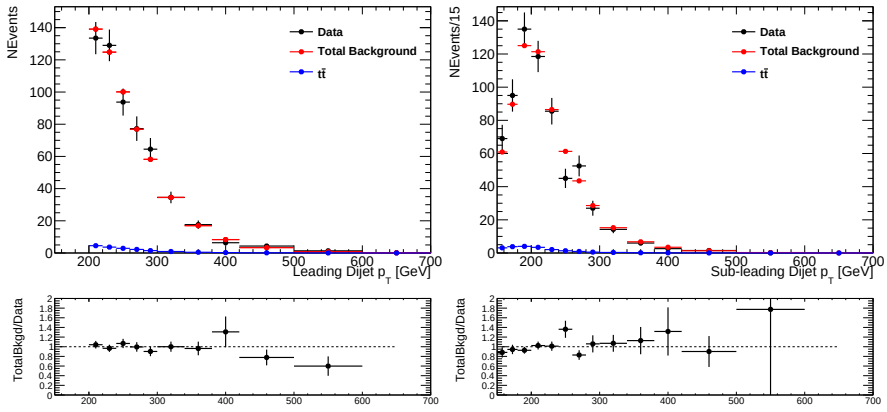

(a) Lead dijet p_{T}

(b) Sub-leading dijet p_{T}

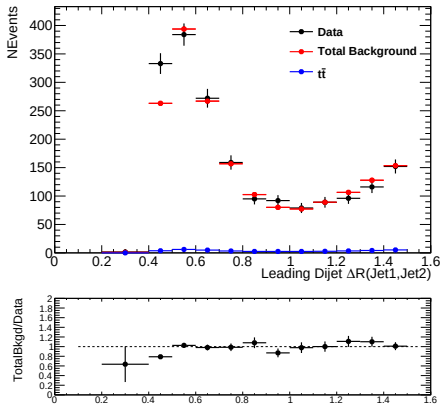

(c) Lead dijet jet-jet ΔR

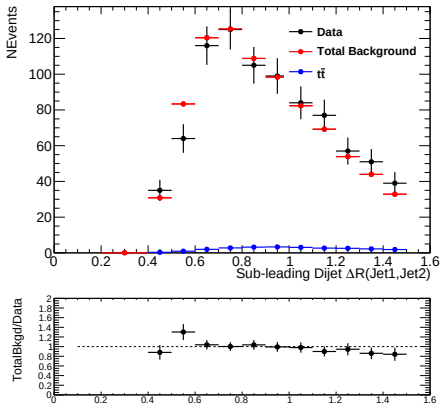

(d) Sub-leading dijet jet-jet ΔR

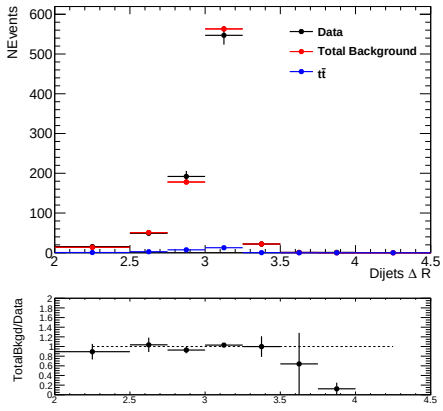

(e) ΔR separation of the dijets

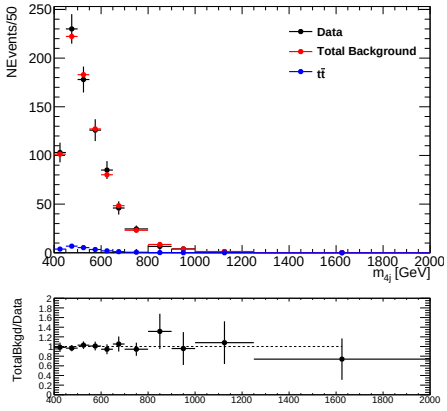

(f) $m_{4\mathrm{j}}$

Figure 5.21.: A comparison of the total predicted background to the data in the Control Region for various kinematic variables, after reweighting the multijet sample, after the MDCs. The small $t\bar{t}$ contribution to the total background is also shown.

Sample	Sideband Region	Control Region
Multijet	907.1 ± 2.8	789.1 ± 2.6
$t\bar{t}$	25.5 ± 0.3	57.5 ± 0.4
Z+jets	14.2 ± 1.2	20.3 ± 1.4
Total Bkgd	946.7 ± 3.1	866.9 ± 3.0
Data	952.0 (± 30.9)	852.0 (± 29.2)

Table 5.2.: The number of events in data and predicted background events after applying the preselection and mass dependent cuts in the Sideband and Control Regions. The uncertainties on these numbers are purely statistical. The $t\bar{t}$ yield in this table is estimated using MC simulation. The total predicted background and data yields do not agree exactly in the Sideband Region because the μ_{QCD} normalisation is performed before the MDCs.

will use the level of agreement in the $m_{4\mathrm{j}}$ distribution shown in Figure 5.21f to set a shape uncertainty on the QCD background prediction.

5.3.3. $t\bar{t}$ Background

The $t\bar{t}$ background is mostly made up of events where both of the tops decay hadronically and the c-jets from the W boson decays are mistagged as b-jets. These b-c dijets can often have masses similar to m_h due to some of the mass of the top going into the third jet which is not included in the dijet.

Normalisation of the $t\bar{t}$ Background

For the normalisation of the $t\bar{t}$ background a data-driven approach was used. The reason for this is that using MC would rely on trusting the MC modelling of our Signal Region which contains relatively boosted tops and requires there to be mis-tags. The cross-sections of boosted tops have been shown to be overestimated by up to 50% for POWHEG +PYTHIA $t\bar{t}$ MC, even with the p_{T} correction described in Section 5.1 [91]. Using MC also relies on the modelling of the $t\bar{t}$ veto efficiency since tops that

pass this cut can have lost jets or mis-measured jets and these can be inaccurately described by MC.

Method Overview

To estimate the number of $t\bar{t}$ events in our Signal Region a $t\bar{t}$ Control Sample is used. The $t\bar{t}$ Control Sample is defined by events that pass the basic kinematic cuts described in Section 5.2.4 but fail the $t\bar{t}$ veto in Section 5.2.4. The $t\bar{t}$ yield in this $t\bar{t}$ Control Sample is calculated and the amount of $t\bar{t}$ events in the Signal Region is extrapolated from this value using the efficiency of a dijet to pass the $t\bar{t}$ veto, $\epsilon_{t\bar{t}}$, which is measured in data. The $t\bar{t}$ yield in the Signal Region is calculated using the following formula:

$$N_{t\bar{t}}^{Bkg} = \frac{\epsilon_{t\bar{t}}^2}{1-\epsilon_{t\bar{t}}^2} \times N_{t\bar{t}}^{CS}, \tag{5.8}$$

where $\epsilon_{t\bar{t}}$ is the $t\bar{t}$ veto efficiency, and $N_{t\bar{t}}^{CS}$ is the number of $t\bar{t}$ events in the Signal Region of the $t\bar{t}$ Control Sample.

Estimating the $t\bar{t}$ Yield in the $t\bar{t}$ Control Sample

$N_{t\bar{t}}^{CS}$ from Equation 5.8 is determined from the $t\bar{t}$ Control Sample, which is the events which pass the Preselection (Section 5.2.4) with the exception that the $t\bar{t}$ veto is reversed, such that one or both dijets in the event fail the X_{tt} cut (i.e. have $X_{tt} < 3.2$). This contains an independent sample from the events in the Signal Region and is composed of ∼70% multijet and ∼30% $t\bar{t}$. To determine the $t\bar{t}$ yield in this sample, the multijet and (small) Z+jets contributions must be subtracted from the data. To determine the multijet content, a method analogous to that described in Section 5.3.2 is used where the data in a "2-tag" sample is normalised and then reweighted to the 4-tag data in a sideband region and tested in a control region. The regions can be seen in Figure 5.22 and are defined as:

- TTSideband Region: ($m_{2\text{j}}^{\text{subl}} < 55\,\text{GeV}$ OR $\text{m}_{2\text{j}}^{\text{subl}} > 160\,\text{GeV}$) OR ($\text{m}_{2\text{j}}^{\text{lead}} < 65\,\text{GeV}$ OR $\text{m}_{2\text{j}}^{\text{lead}} > 170\,\text{GeV}$)

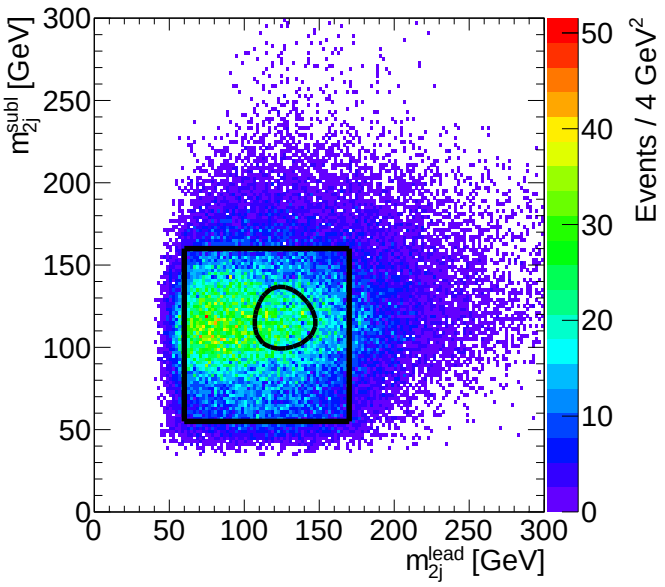

Figure 5.22.: The TTSideband Region and TTControl Region in the m_{2j}^{lead}- m_{2j}^{subl} plane for the 2-tag data sample after the reversal of the $t\bar{t}$ veto requirements.

- TTControl Region: $m_{2j}^{subl} > 55\,\text{GeV}$ AND $m_{2j}^{subl} < 160\,\text{GeV}$ AND $m_{2j}^{lead} > 65\,\text{GeV}$ AND $m_{2j}^{lead} < 170\,\text{GeV}$ AND (event does not pass hh signal ellipse selection).

The TTSideband Region is dominated by multijet events whereas the TTControl Region is $t\bar{t}$ enhanced. To find the normalisation of the multijet background in the $t\bar{t}$ Control Sample, first the 2-tag $t\bar{t}$ MC and Z+jets MC are subtracted from the 2-tag data, then it is scaled by the μ_{QCD} found in Section 5.3.2. It is reasonable to use the value previously found for μ_{QCD} because the ratio of the rate of multijet events that pass the 4-tag to 2-tag selection is independent of the $t\bar{t}$ veto, and in using this value we gain an estimation of the multijet independent of the $t\bar{t}$ Control Sample. The reweighting is done in the same way as Section 5.3.2 except five iterations are needed rather then three (iterations are stopped when the $(n+1)^{\text{th}}$-iteration yields negligible difference to the n^{th}-iteration - the weights are ~ 1).

Table 5.3 shows the predicted number of background events in the TTSideband and TTControl Regions. There is a 20% uncertainty given to the $t\bar{t}$ MC from adding in quadrature detector effects such as JES and JER, this does not include other uncertainties such as generator uncertainties. The agreement between the total predicted background and data in the TTSideband and TTControl Regions is

Sample	TTSideband Region	TTControl Region	TTSignal Region
Multijet	159.9 ± 9.6	347.4 ± 20.8	49.6 ± 3.0
$t\bar{t}$ MC	34.6 ± 6.9	164.2 ± 32.8	45.6 ± 9.1
Z+jets MC	1.3 ± 0.3	5.5 ± 0.7	0.3 ± 0.2
Total Bkgd	195.7 ± 11.8	517.1 ± 38.8	95.5 ± 9.6
Data	230.0 (± 15.2)	485.0 (± 22.0)	73.0 (± 8.5)

Table 5.3.: The number of events in data and predicted background events in the TTSideband, TTControl and TTSignal Regions for the $t\bar{t}$ control sample, before using Mass Dependent Cuts. The multijet numbers have an uncertainty of 6% and the $t\bar{t}$ MC has an uncertainty of 20%. The uncertainties on the Z+jets numbers are purely statistical, reflecting the limited size of the sample.

reasonable. Table 5.3 also shows the number of data events along with the predicted number of multijet and Z+jets events in the signal region for the$t\bar{t}$ Control Sample (TTSignal Region). Subtracting the multijet and Z+jets predictions from the data gives us the predicted number of $t\bar{t}$ events in the TTSignal Region, before MDCs, to be:

$$N_{t\bar{t}}^{CS} = 23.1 \pm 8.6.$$

There is a large statistical uncertainty due to the limited data. This method assumes that there is no signal contamination within the TTSignal Region. This is assumed to be a reasonable assumption since the efficiency for the signal to fail the $t\bar{t}$ veto is 10%.

Measurement of the $t\bar{t}$ Veto Efficiency

The $t\bar{t}$ veto efficiency used in Equation 5.8 is measured in data using a semi-leptonic selection which has a high $t\bar{t}$ purity. This selection tags a leptonically decaying top and measures the fraction of dijets passing the $t\bar{t}$ veto on the other side of the event. The event selection for this Semi-Leptonic Control Sample (SLCS) is as follows:

- single muon trigger
- leptonic top candidate with $p_{\mathrm{T}} > 180$ GeV

Observable	Before m_h cut	After m_h cut
N_P	388	147
N_F	229	132
$\epsilon_{t\bar{t}}$ from Data	0.629 ± 0.019	0.527 ± 0.030
$\epsilon_{t\bar{t}}$ from MC	0.606 ± 0.008	0.540 ± 0.012

Table 5.4.: The $t\bar{t}$ veto efficiency measured in data. A comparison with the value measured in MC is also included. Quoted uncertainties are statistical only. m_h cut is defined by $100 \leq m_{dijet} \leq 140$ GeV.

- dijet candidate with $p_{\mathrm{T}} > 150$ GeV(same dijet selection as in Section 5.2.4)

where the leptonic candidate consists of:

- one isolated, tight muon with $p_{\mathrm{T}} > 25$ GeV
- one b-tagged jet (same selection as in Section 5.2.4)
- $\Delta R_{(\mu,b\text{-jet})} < 1.3$

The p_{T} of the leptonic candidate is the vectorial sum of the μ and b-jet's transverse momentum, in addition to the missing transverse energy in the event. The b-jet in the leptonic candidate must not be used to form the dijet candidate.

There are two assumptions when measuring this veto efficiency. The first is that the rates at which the two dijets in the Signal Region pass the $t\bar{t}$ veto are uncorrelated and the second is that the rate at which the dijet passes the veto in the SLCS is the same as for a dijet in the Signal Region. Both assumptions were tested in MC and found to have closure of better then 10%. This value is used as an additional uncertainty on the efficiency. Table 5.4 presents the $t\bar{t}$ veto efficiency measured in data, along with a comparison from MC, where the quoted uncertainties are statistical.

The $t\bar{t}$ veto efficiency with associated systematics is:

$$\epsilon_{t\bar{t}} = 0.53 \pm 0.03(\mathrm{stat}) \pm 0.05(\mathrm{sys}). \tag{5.9}$$

The uncertainties on the veto efficiency are given by the statistical uncertainty on the number of events in the SLCS and a 10% systematic uncertainty assigned to cover the non-closure in MC. This systematic uncertainty accounts for the extrapolation of the veto efficiency from the SLCS to the TTSignal Region.

$t\bar{t}$ Normalisation Predictions

After substituting the measured veto efficiency and $N_{t\bar{t}}^{CS}$ into Equation 5.8 the final $t\bar{t}$ prediction in the Signal Region, before the MDCs, is:

$$N_{t\bar{t}}^{Bkgd} = 8.9 \pm 4.4.$$

After the mass dependent cuts are applied, we get:

$$N_{t\bar{t}}^{Bkgd} = 5.2 \pm 2.6.$$

The uncertainty on this prediction includes the full propagation of both the statistical uncertainty on $N_{t\bar{t}}^{CS}$ and the statistical and systematic uncertainties on the veto efficiency. It is ∼50% and is mainly dominated by the low statistics in the $t\bar{t}$ Control Sample.

$t\bar{t}$ Shape

Monte Carlo is used to estimate the shape of the $t\bar{t}$ background. A data-driven method could not be used due to low statistics. Due to low statistics in the 4-tag $t\bar{t}$ MC passing our event selection, the 2-tag selection had to be used. Figure 5.23 shows the $m_{4\text{j}}$ distributions for the 2-tag and 4-tag $t\bar{t}$ MC samples before and after the X_{hh} cut that defines the Signal Region. There is reasonable agreement between the two samples within the large statistical uncertainties. Later, in Section 5.5.3, the level of agreement is quantified and assigned as a shape systematic on the $t\bar{t}$ prediction.

5.3.4. Total Background Prediction

Table 5.5 shows the predicted number of multijet, $t\bar{t}$ and Z+jets background events in the Signal Region. The multijet and $t\bar{t}$ predictions are taken from the data-driven

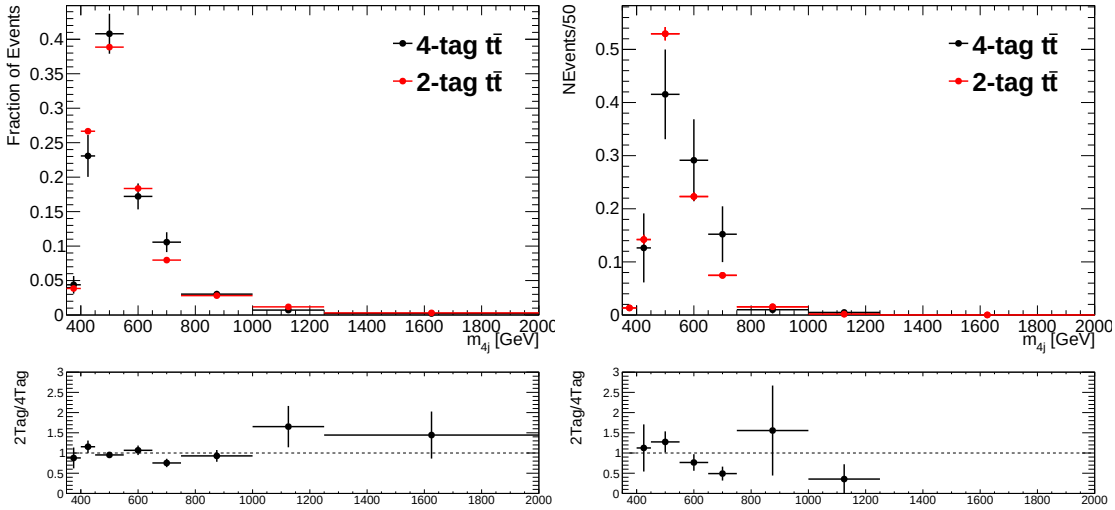

Figure 5.23.: A comparison of the m_{4j} distributions produced from the $t\bar{t}$ MC after applying the 4-tag (black) and 2-tag (red) for **(a)** after the preselection and MDCs and **(b)** in the Signal Region. The distributions are normalised to equal area.

Sample	Signal Region
Multijet	81.4 ± 4.9
$t\bar{t}$	5.2 ± 2.6
Z+jets	0.4 ± 0.2
Total Bkgd	87.0 ± 5.6

Table 5.5.: The number of predicted background events in the Signal Region. The uncertainties on the Z+jets number is purely statistical, reflecting the limited statistics in the Z+jets MC sample. The uncertainty on the $t\bar{t}$ and multijet is the full uncertainty on the data-driven methods, explained in Section 5.3.3 for the $t\bar{t}$ and Section 5.4 for the multijet.

methods already described, whereas the Z+jets is taken from MC. Figure 5.24 shows the predicted background in the Signal Region as a function of m_{4j}. It is shown with the mass rescaling described in Section 5.2.7, as this is what is used in the limit setting.

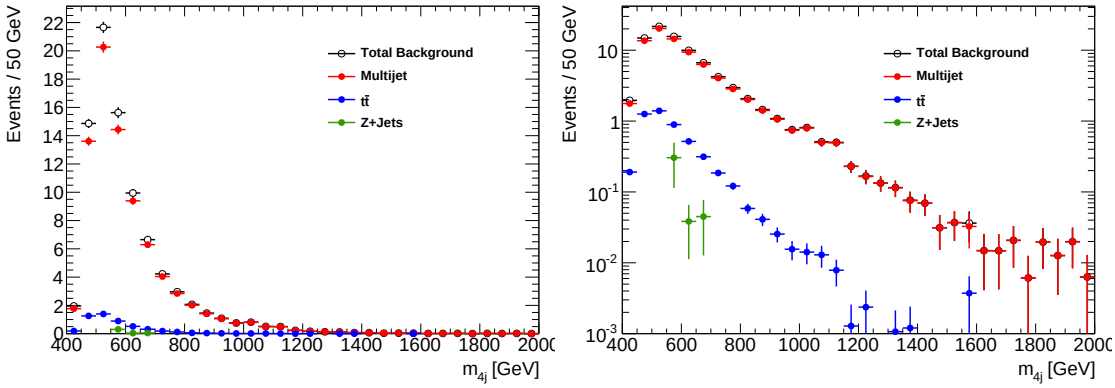

Figure 5.24.: The predicted background m_{4j} distribution in the Signal Region (**(a)** normal scale, **(b)** log scale).

5.4. Multijet Background Cross-checks and Uncertainties

In Section 5.3.2, the agreement between the total number of predicted background events and the data in the Control Region was shown to be well within the 3.4% statistical error on the data. From this, it would be reasonable to assume that a suitable systematic uncertainty on the multijet background normalisation would be 3.4%. When making the data-driven multijet background estimation a few assumptions are made, in this section different variations in the method of predicting the multijet background are used to test these assumptions. Whilst showing the method to be robust in shape and normalisation, they lead to an increased total uncertainty of 6% on the multijet background normalisation.

The first assumption tested is that the multijet background can be modelled using the "2-tag" selection. This is checked by repeating the multijet background estimation using looser and tighter b-tagging requirements when selecting the 2-tag sample. These differing conditions change the flavour composition and influence of b-tagging on the 2-tag model.

The second assumption tested is that the choice of definitions for the Sideband and Control Regions doesn't have an impact on the multijet prediction and its associated systematics. For example, the agreement in the Control Region could be a product of the fact that the Sideband and Control Regions both are dominated by

low-mass dijets, however the Signal Region does not contain as many. This can be tested by varying these definitions and then repeating the background estimation and checking the level of agreement in shape and normalisation in the Control Region and also between the nominal prediction. Figure 5.25a shows the first of these tests, in this case the circle defining the Sideband and Control Regions has been shifted so that the Sideband Region has an enhanced amount of high-mass dijets. Figure 5.25b shows the reverse of this - the Sideband Region contains mostly low-mass dijets. In both cases the Control Region's radius has been altered to give roughly equal statistics between the two regions.

The third assumption is that there is minimal signal contamination in the Control Region. If this was false the uncertainty on the multijet background prediction would be underestimated because one would be checking the level of agreement in the Control Region between the total number of true background events and signal events with the predicted number of background events, rather then the difference between true background and predicted background. The Sideband Region is sufficiently far away enough from the Signal Region that this is not a concern there. Figure 5.25c shows region definitions where the Signal Region has been expanded such that for a 500 GeV Graviton the relative acceptance of signal in the Control Region with respect to the Signal Region has decreased from 34% to 17%, corresponding to 0.9% of the data events in the Control Region. To repeat the data-driven techniques used for predicting the multijet background in this case, the $t\bar{t}$ has to be estimated using the $t\bar{t}$ MC. This is because the Signal Region definition has changed and the data-driven technique is reliant on the original definition.

Table 5.6 shows the results in normalisation between the multijet predictions in all of these cross-checks. In all cases the difference between total background and data in the Control Region is <5%, and the largest difference between the multijet prediction in the Signal Region is in the "Low Mass" variation where there is a difference of -5.5%, for this reason we assign a total uncertainty of 6% to the multijet background normalisation.

Figure 5.26 shows the impact of these varying predictions on the shape of the multijet prediction. Good agreement between the nominal prediction and cross-checks is shown and all fluctuations are well within the shape uncertainty on the multijet prediction. The large errors seen at high $m_{4\mathrm{j}}$ in Figures 5.26c, 5.26d and 5.26e are due to the samples being very highly correlated in this region.

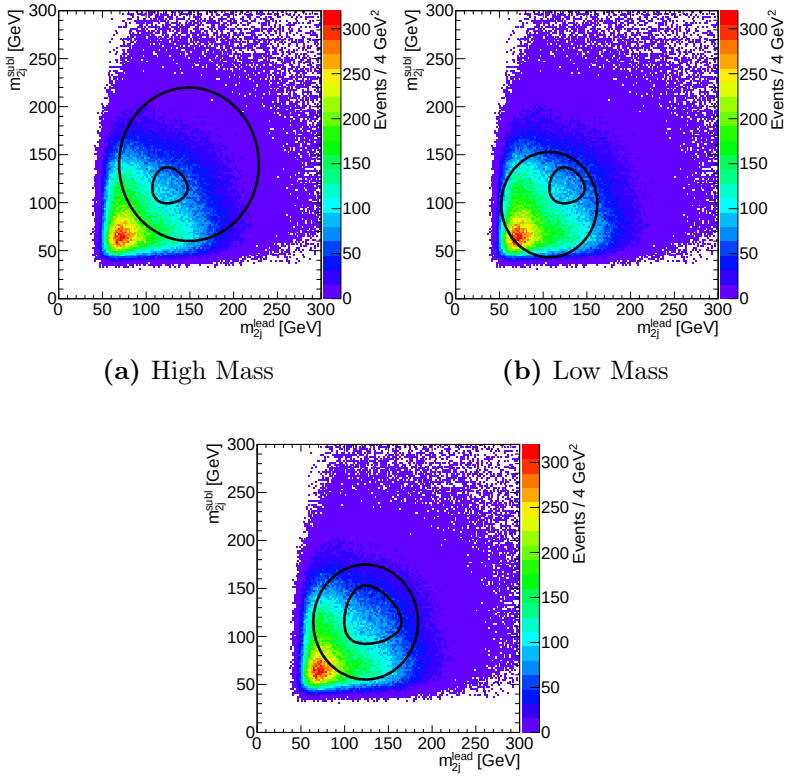

(a) High Mass **(b)** Low Mass

(c) Signal Depleted

Figure 5.25.: Alternative sets of Signal, Control and Sideband Region definitions in the $m_{2\mathrm{j}}^{\mathrm{lead}}$-$m_{2\mathrm{j}}^{\mathrm{subl}}$ plane, overlaid onto the 2-tag data.

	Nominal	60% Tagging	80% Tagging	High Mass	Low Mass	Signal Depleted
Signal Region: Multijet	81.4 ± 0.8	82.8	79.6	77.4	85.9	79.9
Signal Region: $t\bar{t}$	5.2 ± 2.6	6.2	3.0	6.1	4.5	11.9
Control Region: Data - Bkgd	3.4%	-1.9%	4.2%	2.2%	-4.1%	-4.4%
Signal Region: Mulitjet Variation	-	-1.7%	2.2%	4.9%	-5.5%	1.8%

Table 5.6.: Summary of the impact from changing the b-tagging used in the 2-tag QCD background model, and changing the region definitions in terms of the predicted backgrounds in the Signal Regions and the agreement between data and background prediction in the Control Region. The differing region definitions can be found in Figure 5.25. The full uncertainty on the background numbers in the nominal case are shown. The $t\bar{t}$ has been estimated using data-driven techniques for all cases except for the "Signal Depleted" region definition.

5.5. Systematic Uncertainties

There are two types of systematic uncertainty that are evaluated: those affecting the modelling of the signal, and those affecting the background predictions. Detector based uncertainties are only applied to the signal MC because the multijet prediction estimate is fully data-driven and the $t\bar{t}$ MC has a very large shape uncertainty applied that will dominate any uncertainties from detector systematics. The Z+Jets MC constitutes <1% of the total background so only the statistical uncertainty on the prediction is used.

5.5.1. Systematic Uncertainties on the Signal Modelling

Detector Based Uncertainties

There is an uncertainty in the modelling of the measurement of a jet's energy - the jet energy scale (JES), which is described in Section 4.1.2. It is evaluated by applying $\pm 1\sigma$ variations in JES to the signal MC samples.

There is another uncertainty which arises from the modelling of the resolution of the detector's measurement of a jet's energy, the jet energy resolution (JER). This is described in Section 4.1.2. The case where the JER is underestimated is evaluated by smearing each jet's p_{T} by the JER uncertainty (this is p_{T} dependent). The case where the JER is overestimated is not considered.

A third type of detector-based uncertainty comes from the modelling of the efficiency of a jet containing a b-hadron to pass the b-tagging requirement, this is described in Section 4.2.1. This is evaluated by applying $\pm 1\sigma$ variations in b-tagging to the signal MC samples.

The final source of detector-based uncertainty which is calculated for our signal comes from the measurement of the recorded integrated luminosity. This has a relative uncertainty of $\pm 2.8\%$ which is derived using the same methodology as in Ref. [47], and is described in Section 3.2.5.

Figure 5.27 shows the effect of applying the JES shifts and JER smearing to the jet p_{T}s on the dijet masses and $m_{4\mathrm{j}}$ distribution for the $m_{G^*} = 1000$ GeV, $k/\bar{M}_{Pl} = 1.0$ signal MC sample.

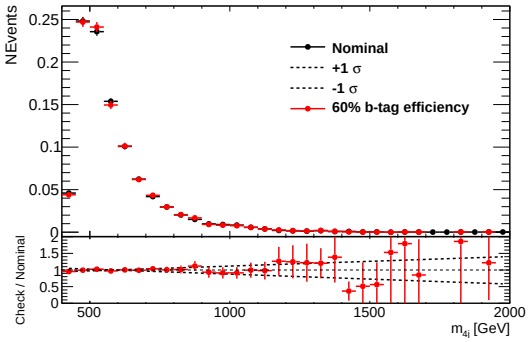

(a) 60% b-tag efficiency used for 2-tag sample

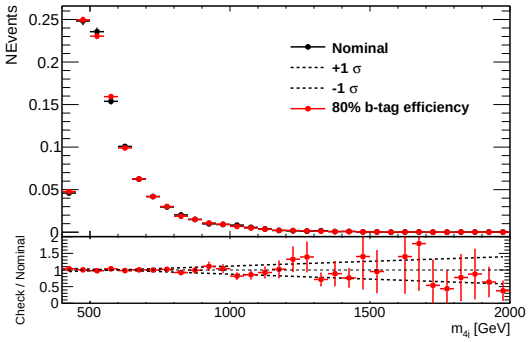

(b) 80% b-tag efficiency used for 2-tag sample

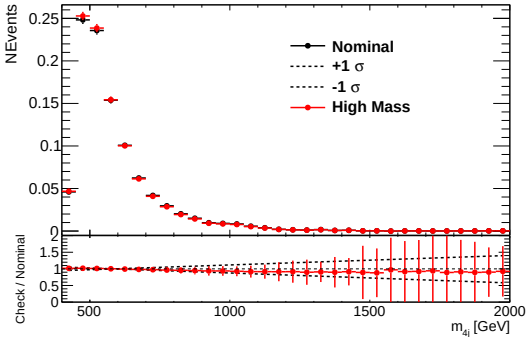

(c) "High mass" variation, data-driven $t\bar{t}$ (Figure 5.25a)

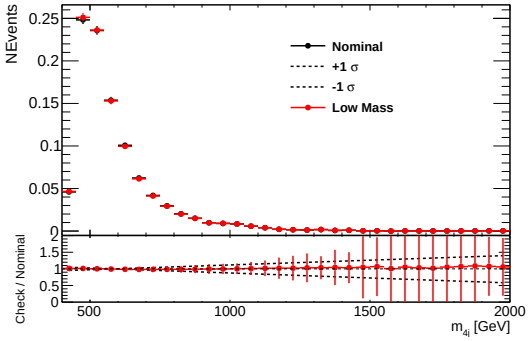

(d) "Low mass" variation, data-driven $t\bar{t}$ (Figure 5.25b)

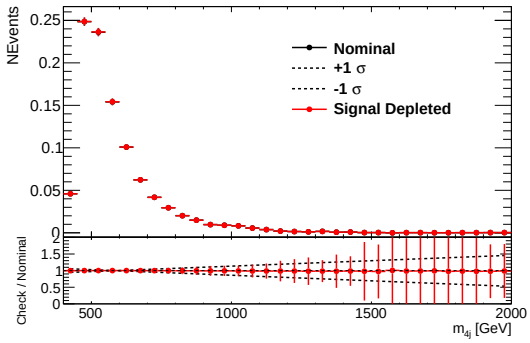

(e) "Signal depleted" variation, MC $t\bar{t}$ (Figure 5.25c)

Figure 5.26.: A comparison of the multijet background prediction of the default 70% b-tag efficiency 2-tag model for the multijet versus the 60% and 80% b-tag efficiency for the 2-tag, and differing region definitions for the multijet model predictions. The dotted line on the ratio pad indicates the multijet shape uncertainty (see Section 5.5.2).

	RS Graviton, m_{G*} [GeV]										
Variation	500	600	700	800	900	1000	1100	1200	1300	1400	1500
JER	-1.53	-0.37	-1.07	-1.46	-2.68	-1.26	-1.88	-1.34	-1.71	-0.44	-3.33
JES Up	9.14	5.61	3.38	1.76	-0.01	-0.60	-0.36	-2.14	-2.45	-2.13	-2.42
JES Down	-10.5	-5.67	-4.16	-4.49	-1.65	-2.98	-2.94	-0.69	-1.82	-0.36	-2.66
b-tagging Up	11.9	14.4	17.0	18.9	20.1	21.0	21.4	21.5	21.2	21.0	20.8
b-tagging Down	-11.0	-13.1	-15.1	-16.6	-17.6	-18.2	-18.5	-18.6	-18.4	-18.3	-18.1

Table 5.7.: A table showing the percentage change in the predicted number of events passing the full Signal Region requirements for each of the Graviton signal mass samples.

Table 5.7 shows the percentage change in the predicted number of events passing the full analysis requirements for the JES, JER and b-tagging uncertainties for each of the $k/\bar{M}_{Pl} = 1.0$ Graviton signal mass samples. It shows that, for signal normalisation, the b-tagging uncertainties dominate except at the very lowest mass. As the sample mass gets larger the b-tagging uncertainty increases even more, and this is due to the larger fraction of jets with $p_{\mathrm{T}} > 300$ GeV for which there is an extra, larger term in the b-tagging uncertainties.

Theoretical Uncertainties on the Acceptance of the Signal

Uncertainties on the signal modelling can also arise from theoretical assumptions which can affect the acceptance of the signal. Three sources of this were considered.

These uncertainties were investigated by generating particle-level samples using the same configurations as the nominal signal samples but with appropriate variations, and then assessing the difference in yields after the full analysis selection.

The first source investigated comes from the modelling of the initial- and final-state radiation (ISR and FSR). The variation was introduced in the relevant parton shower parameters in PYTHIA 8.

The second source investigated comes from PDF uncertainties. Here the uncertainty was estimated by taking the maximum difference between the predictions when using MSTW2008nlo [92], NNPDF2.3 [93] and CTEQ6L1.

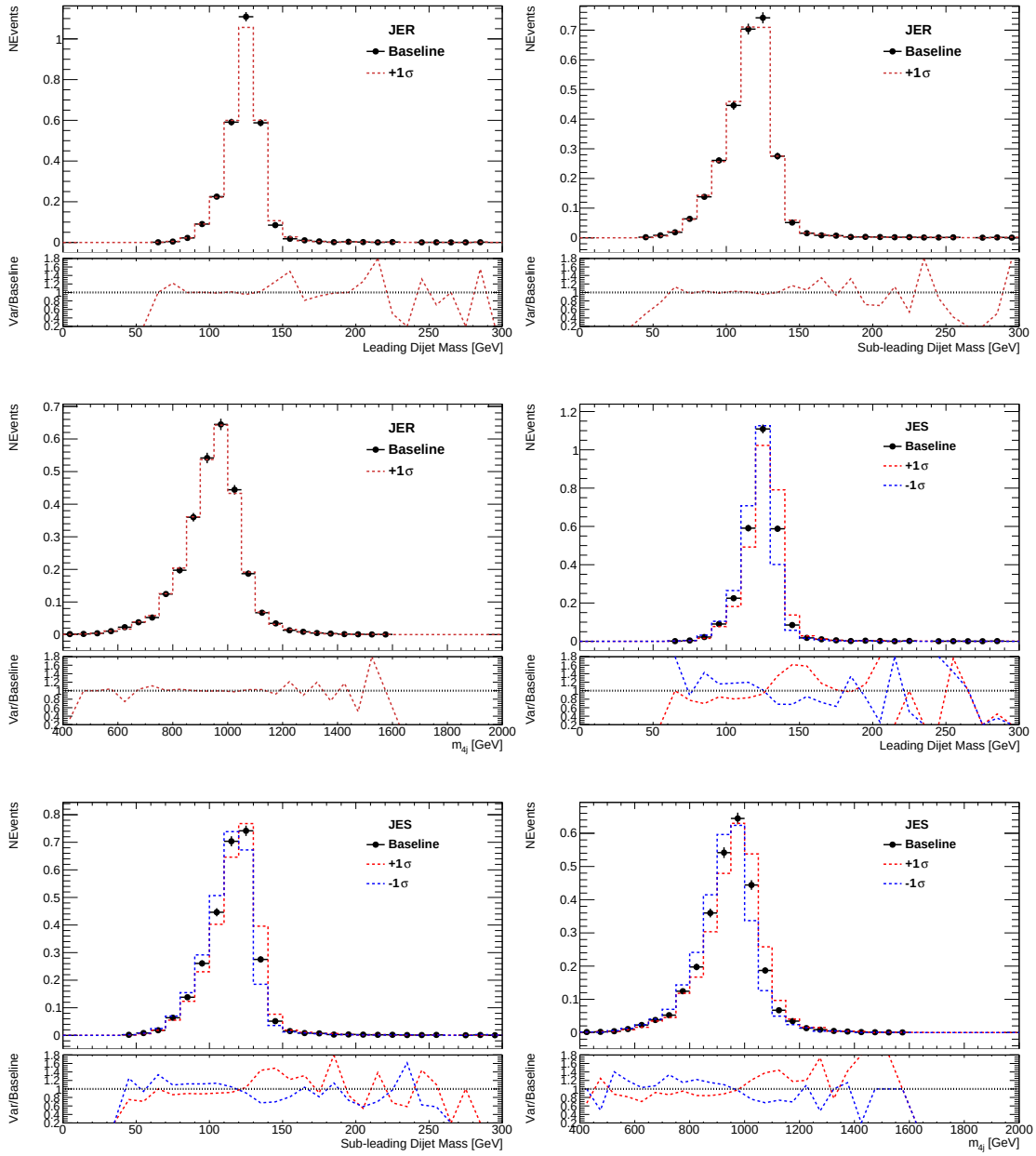

Figure 5.27.: Plots showing the effects of the [**(a-c)**] JER smearing and [**(d-f)**] JES shifts on the dijet masses and $m_{4\mathrm{j}}$ for the $m_{G*} = 1000$ GeV Graviton.

The final source of theoretical uncertainty investigated arises from uncertainties in the beam energy. This was investigated by varying the beam energy by ±26.5GeV [94] in the simulation.

The only variation which showed a non-negligable impact on the yield came from the FSR leading to a ±1.0% theoretical uncertainty on the modelling of the signal acceptance.

5.5.2. Systematic Uncertainties on the Multijet Prediction

Uncertainty on the Multijet Normalisation

As mentioned in the previous section, the multijet background has been assigned a normalisation uncertainty of 6% which has come from re-estimating the background within different scenarios and then testing the agreement between total background and data in the Control Region, as well as the differences in predicted multijet background in the Signal Region from the nominal case (Section 5.4).

Uncertainty on the Multijet Shape

The uncertainty on the multijet background shape is evaluated in the Control Region by looking at the level of agreement between the total background and data in the $m_{4\mathrm{j}}$ distribution, which can be seen in Figure 5.21f. Figure 5.28a shows the ratio of total background events to data in this region, a linear fit to this ratio, and the $\pm 1\sigma$ uncertainties on the two fitted parameters. The fit is good, and the gradient of the fit is consistent with 0 which shows that the background model and data are consistent. We take as a potential bias in the multijet background prediction the maximum gradient allowed by a $\pm 1\sigma$ variation to the fitted parameters. The multijet prediction in the Signal Region is then reweighted to these functions, preserving the normalisation, as can be seen in Figure 5.28b

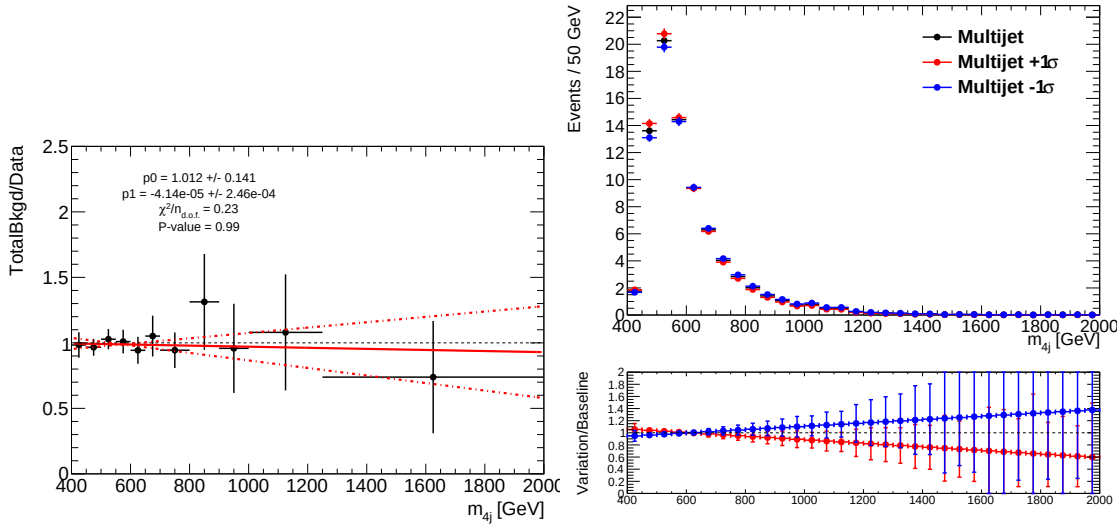

Figure 5.28.: **(a)** A first order polynomial fit to the background-to-data ratio of the $m_{4\mathrm{j}}$ distribution in the Control Region. The dashed lines show the $\pm 1\sigma$ uncertainties on the two fitted parameters. (b) The central multijet background prediction (black), and the plus/minus (red/blue) multijet background variation histograms for the Signal Region.

5.5.3. Systematic Uncertainties on the $t\bar{t}$ Prediction

Uncertainty on the $t\bar{t}$ Normalisation

The uncertainty on the normalisation of the $t\bar{t}$ background is evaluated to be $\pm 50\%$. The main contribution to this is from the large statistical uncertainty on $N_{t\bar{t}}^{CS}$ due to the low yield of events in the $t\bar{t}$ Control Sample. The other component to this is from the statistical and systematic uncertainties on the $t\bar{t}$ veto efficiency.

Uncertainty on the $t\bar{t}$ Shape

The $t\bar{t}$ shape is modelled using "2-tag" $t\bar{t}$ MC (Section 5.3.3), the uncertainty on this shape is evaluated by comparing the $m_{4\mathrm{j}}$ distributions of the "2-tag" and "4-tag" samples, as seen in Figure 5.23. Figure 5.29a shows a linear fit to the ratio of the normalised $m_{4\mathrm{j}}$ distributions in these two samples. The uncertainty is evaluated by finding the maximum gradient when applying the $\pm 1\sigma$ variations to the fit and reweighting the sample to this fit in the Signal Region (the same method as for the

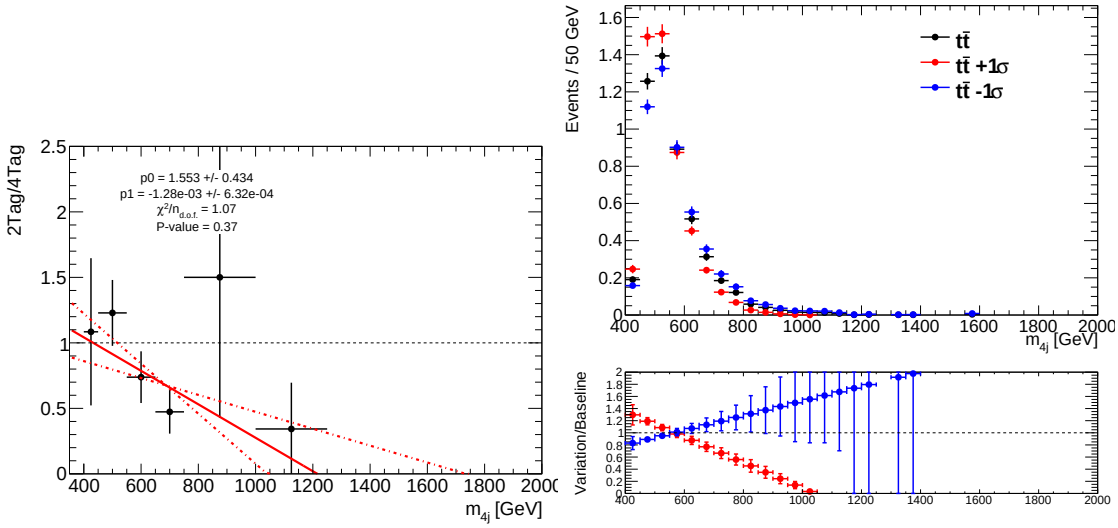

Figure 5.29.: **(a)** A first order polynomial fit to the "2-tag" to "4-tag" ratio in the $t\bar{t}$ MC of the $m_{4\text{j}}$ distribution in the Signal Region. The dashed lines show the $\pm 1\sigma$ uncertainties on the two fitted parameters. (b) The central $t\bar{t}$ background prediction (black), and the plus/minus (red/blue) $t\bar{t}$ background variation histograms for the Signal Region.

multijet background shape). The results of this can be seen in Figure 5.29b, this uncertainty is large: $\sim$30% and $\sim$100% at $m_{4\text{j}} = 400$ and 1000 GeV, and this is mainly due to the very low statistics in the 4-tag sample.

5.5.4. Systematic Uncertainties Summary

Table 5.8 shows the relative impact of the uncertainties on the event yields.

5.6. Statistical Analysis

When analysing the results of a search one can ask two questions:

1. How well does my data agree with the predicted background?
2. How well does my alternate theory describe this data?

Statistical methods are used to find answers to these questions.

Source	Bkgd	SM hh	G^*_{KK}		H
			$k/\bar{M}_{Pl} = 1.0$	$k/\bar{M}_{Pl} = 2.0$	
Luminosity	–	2.8	2.8	2.8	2.8
JER	–	4.5	1.1	1.1	2.0
JES	–	7	1.8	1.3	3.4
b-tagging	–	12	22	21	22
Theoretical	–	1.0	1.1	1.1	1.1
Multijet	5.6	–	–	–	–
$t\bar{t}$	3.0	–	–	–	–
Total	6.4	15	22	22	23

Table 5.8.: Summary of systematic uncertainties (expressed in percent) in the total background and signal event yields. Signal yield uncertainties are provided for non-resonant SM Higgs boson pair production and three resonances with m = 1000 GeV.

To answer the first question we can construct a numerical value known as the "p-value", which is the probability of a background-only (null hypothesis) sample to produce the same or larger fluctuations than the observed data. This is described in Section 5.6.1.

The answer to the second question depends on the first, if there are no significant deviations from the background hypothesis (defined as a global p-value of 3σ or more) then we can proceed to set exclusion limits on the theory. This is described in Section 5.6.2.

In both cases, we need to construct the likelihood function, $L(\mu, \boldsymbol{\theta})$, for which we use poisson statistics:

$$L(\mu, \boldsymbol{\theta}) = \prod_{i=1}^{N} \frac{(\mu s_i + b_i)^{n_i}}{n_i!} e^{-(\mu s_i + b_i)}, \tag{5.10}$$

where i denotes the histogram bin, n_i is the number of data entries in bin i, $\mu s_i + b_i$ is the number of expected signal+background events in bin i, and μ is the signal normalisation ($\mu = 0$ is the background-only case).

The likelihood is also a function of a set of nuisance parameters denoted by $\boldsymbol{\theta}$, these are the systematic uncertainties of the signal and background model. They are extra terms put into Equation 5.10 which are constrained using Gaussian and log-normal functions. These are described in Section 5.6.2. When making test statistics, profile likelihoods are made, whereby the systematic uncertainties are varied to give a maximum value for the likelihood.

In the non-resonant SM hh search, we perform a counting experiment, so rather than the Likelihood being binned in $m_{4\mathrm{j}}$, like in the resonant case, we take the total number of events in the Signal Region (effectively using a histogram with one bin).

5.6.1. Search Procedure

A test statistic is constructed using a one sided profile likelihood ratio:

$$q_0 = \begin{cases} -2\ln\frac{L(0,\hat{\hat{\boldsymbol{\theta}}}(0))}{L(\hat{\mu},\hat{\boldsymbol{\theta}})} & \hat{\mu} > 0 \\ 0 & \hat{\mu} < 0 \end{cases} \tag{5.11}$$

Where, μ is the value of the signal normalisation considered, $\hat{\mu}$ is the maximum likelihood (ML) value of μ (the value of μ when the likelihood is maximised). θ are the set of nuisance parameters, $\hat{\boldsymbol{\theta}}$ is the ML value of θ and $\hat{\hat{\boldsymbol{\theta}}}$ is the ML value of θ when μ is fixed at a particular value. L denotes the profile likelihood, $L(\hat{\mu}, \hat{\boldsymbol{\theta}})$ is the likelihood where μ is allowed to take any value, the unconstrained likelihood. $L(0, \hat{\hat{\boldsymbol{\theta}}}(0))$ is the likelihood for the value of $\mu = 0$, the constrained likelihood. This tests the compatibility of the data with the background-only hypothesis. The local p-value of a set of data, p_0, is defined as the probability for the background only hypothesis to have a q_0 value greater then or equal to that of the q_0 found in data: $\mathrm{P}(q_{0,(\mu=0)} \geq q_{0,(data)})$. To get p_0, the distribution of the test statistic is built up from pseudo-experiments which are generated with the background-only hypothesis.

If a local p_0-value corresponds to a discrepancy of 3σ or more then we apply the Look Elsewhere Effect (LEE) to find the global p-value. The LEE is a correction we apply to the local p_0-value to account for the fact that we are performing many searches, so the probability of seeing an upwards fluctuation in the $m_{4\mathrm{j}}$ distribution is increased. This correction changes the signal hypothesis from a particle with a

specific mass to a new particle with some mass in the observed region, e.g. for the graviton, it goes from looking for a graviton with a specific mass e.g. 500 GeV, to a graviton with mass: $500 \leq m_{G^*} \leq 1500$ GeV. The LEE correction is computed using the distribution of the test statistic, q_0, in background-only pseudo-experiments.

To find the global p_0-value we apply the following equation [95]:

$$p_0^{global} = p_0^{local} + < N_{1\sigma} > e^{-(q_0^{max} - q_0^{1\sigma})/2}, \tag{5.12}$$

where p_0^{local} is the lowest p_0-value across the mass range tested, corresponding to a test statistic value of q_0^{max}. $< N_{1\sigma} >$ is the average number of times the test statistic value crosses the value corresponding to 1σ: $q_0^{1\sigma}$, (upwards crossings) across the mass range tested.

The signal models tested are the resonant RS graviton with $k/\bar{M}_{Pl} = 1.0, 1.5, 2.0$, 2HDM heavy neutral scalar H, and the non-resonant SM hh production. The masses of the resonant signals which are investigated can be seen in Table 5.9. These intervals are chosen because of the combined factors of the $m_{4\mathrm{j}}$ resolution, signal width, and background $m_{4\mathrm{j}}$ distribution, with the narrower resonances having more masses investigated.

The binning for the search phase is driven by the same factors as the mass interval choice. In this case, the $k/\bar{M}_{Pl} = 1.0$ graviton and 2HDM samples have the same binning as in Table 5.9, but for the $k/\bar{M}_{Pl} = 1.5, 2.0$ gravitons a fixed bin width of 50 GeV is used over the whole $m_{4\mathrm{j}}$ spectrum.

Since the MC samples only exist between 500 and 1500 GeV in 100 GeV steps, searching at masses between these points requires the formation of signal templates based on interpolation between the available samples as described below.

Signal Template Interpolation

The $m_{4\mathrm{j}}$ distributions of the signal masses for which we don't have MC samples are generated from pseudo-data using a physically motivated functional form, where the parameters used in the fit are interpolated from the existing samples, after all of the requirements in Section 5.2 have been applied. The functional form has three parts: a term for the resonance, a term for the resolution of our detector and an efficiency

	Sample		
Mass Range [GeV]	$k/\bar{M}_{Pl} = 1.0$, 2HDM	$k/\bar{M}_{Pl} = 1.5$	$k/\bar{M}_{Pl} = 2.0$
500 - 600	20	50	50
600 - 800	20	50	100
800 - 1000	20	100	100
1000 - 1500	50	100	100

Table 5.9.: The mass intervals, in GeV, chosen to investigate the resonant signal models. $k/\bar{M}_{Pl} = n$ refers to the RS graviton samples.

term. The first two parts are a Breit-Wigner term convoluted with a Gaussian, this is a Voigtian - $V((m_{4\mathrm{j}} - \mu), \Gamma, \sigma)$. The efficiency term, $\epsilon(m_{4\mathrm{j}})$, is a sixth order polynomial which depends on $m_{4\mathrm{j}}$, and is found by making a fit to the relevant "Signal Region" curve in Figure 5.11. The functional form is $V((m_{4\mathrm{j}} - \mu), \Gamma, \sigma) \times \epsilon(m_{4\mathrm{j}})$. When making the fit, the width term Γ is fixed to the MC value, whilst the mean, μ, and resolution, σ, terms are free to float.

There are four parameters which are necessary to interpolate the signal $m_{4\mathrm{j}}$ distributions: the number of events, N, the width, Γ, the mean, μ, and the resolution, σ. These all depend on the resonance mass itself and are extracted for every mass point in each signal model using fits. Figure 5.30 shows these parameterisations. The fitted mean and signal width have a simple linear dependence on the resonance mass. The number of events and resolution are fitted in two separate regions: $500 \leq m_{4\mathrm{j}} \leq 1000$ GeV and $1000 \leq m_{4\mathrm{j}} \leq 1500$ GeV. The number of events is fitted using a function of the form: $e^{a+bm_{4\mathrm{j}}} \times \epsilon(m_{4\mathrm{j}})$. The resolution is fitted using quadratic functions. The inflection point seen in the resolution fit is due to the mass-dependent cuts on the leading and sub-leading dijet p_{T}s becoming constant.

Once the value of each parameter has been found, 6000 pseudo-data events are generated using the functional form and the specific values of the parameter for each mass sample necessary. These samples are then scaled to N.

To test the validity of this method, the limits obtained from using this functional form were compared to those obtained when using the MC samples (for masses where there is available MC). The agreement was within 0.1σ. An example of a generated $m_{4\mathrm{j}}$ distribution in comparison with the real $m_{4\mathrm{j}}$ distribution obtained from MC can

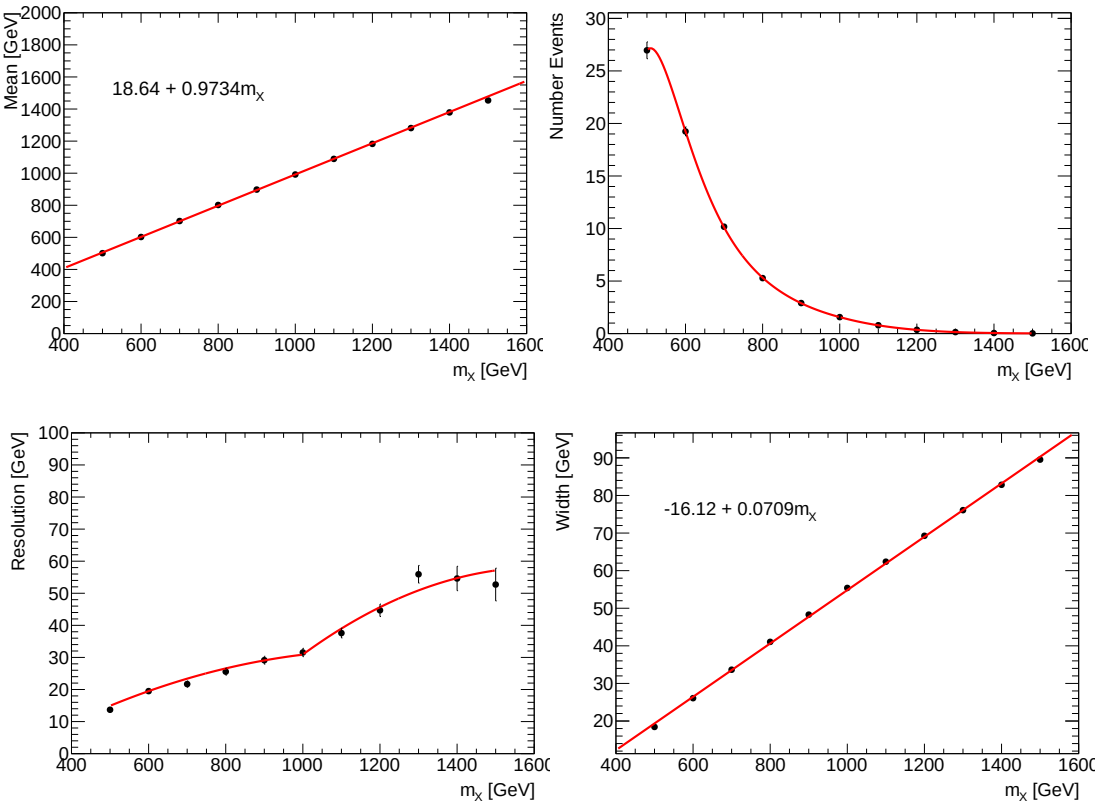

Figure 5.30.: The parameters obtained from a fit to the Graviton $k/\bar{M}_{Pl} = 1.0$ MC samples are shown as black points, along with their parameterisations as red lines.

be seen in Figure 5.31a and the relative difference between the asymptotic limits for the real and generated data can be seen in Figure 5.31b.

5.6.2. Limit Setting

If we do not observe any significant deviation from the background-only hypothesis, defined as a global p-value corresponding to a significance in excess of 3σ, then upper limits on the signal cross-sections are set using the procedure described below.

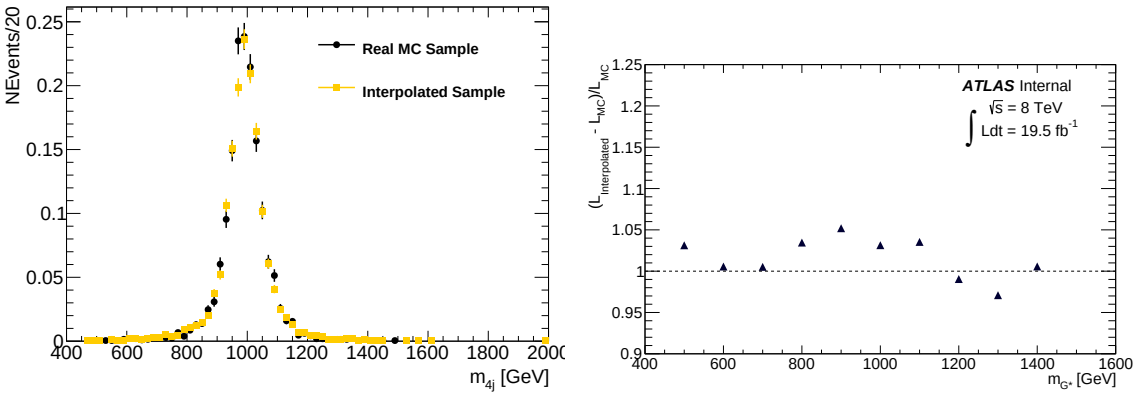

Figure 5.31.: **(a)** The $m_{4\mathrm{j}}$ distributions of the $m_{G^*} = 1000$ GeV, $k/\bar{M}_{Pl} = 1.0$ samples. The MC is shown as black circles and the pseduo-data is shown as orange squares. They are in good agreement. **(b)** The relative difference between the asymptotic limit obtained using the pseudo-data $m_{4\mathrm{j}}$ distribution and the real MC data $m_{4\mathrm{j}}$ distribution.

Choice of Exclusion Statistics

To evaluate an upper limit on a cross-section we use the frequentist CL_s method [96].

$$CL_s = \frac{CL_{s+b}}{CL_b}, \tag{5.13}$$

where CL_{s+b} is the probability of the signal+background hypothesis producing data which gives the same or less compatibility with the signal+background hypothesis than the observed data, and CL_b is the probability of the background-only hypothesis producing data which gives the same or less compatibility with the background-only hypothesis than the observed data. CL_{s+b} can exclude at high confidence limits in places where it has no sensitivity (when the observed data is significantly below the background-only prediction), which is why this ratio is used instead.

The value of the signal normalisation, μ, which gives $CL_s = 0.05$ is used as the upper limit at 95% confidence level.

To calculate the p-values used to determine CL_s we chose a one-sided profile likelihood ratio as the test statistic:

$$\widetilde{q_\mu} = \begin{cases} -2\ln\frac{L(\mu,\hat{\hat{\boldsymbol{\theta}}}(\mu))}{L(0,\hat{\hat{\boldsymbol{\theta}}}(0))} & \hat{\mu} < 0 \\ -2\ln\frac{L(\mu,\hat{\hat{\boldsymbol{\theta}}}(\mu))}{L(\hat{\mu},\hat{\boldsymbol{\theta}})} & 0 \leq \hat{\mu} < \mu \\ 0 & \hat{\mu} > \mu \end{cases}, \tag{5.14}$$

where, μ is the value of the signal normalisation considered, $\hat{\mu}$ is the maximum likelihood (ML) value of μ, θ are the set of nuisance parameters, $\hat{\boldsymbol{\theta}}$ is the ML value of θ and $\hat{\hat{\boldsymbol{\theta}}}$ is the ML value of θ when μ is fixed at a particular value. L denotes the profile likelihood, $L(\hat{\mu}, \hat{\boldsymbol{\theta}})$ is the likelihood where μ is allowed to take any value, the unconstrained likelihood. $L(\mu, \hat{\hat{\boldsymbol{\theta}}})$ is the likelihood for a particular fixed value of μ, the constrained likelihood.

To find the limits, the distribution of the test statistic needs to be found. This is done in two ways: using an asymptotic method and using a toy MC method. The toy MC method doesn't use any assumptions, but is much more CPU intensive. For this reason we use the asymptotic method where valid (this is valid when the statistics are large enough).

For signal masses < 1000 GeV the asymptotic method is used by solving the equations derived in Ref. [97] numerically. These equations are derived by approximating the $\hat{\mu}$ distribution to be Gaussian, such that the profile likelihood ratio becomes a non-central χ^2 distribution. To test the validity of this method, the upper limits were also calculated using the toy experiments method described below, but without any systematics included in the likelihood. Figure 5.32 shows the results of this test for the $k/\bar{M}_{Pl} = 1.0$ graviton, for $m_{G^*} < 1000$ GeV the results are in good agreement.

For signal masses ≥ 1000 GeV, the toy MC method is used. The test statistic distribution is computed from a scan over many signal strengths. For each signal strength, 10000 background-only and 10000 signal+background experiments are generated to find the p-values in order to calculate CL_s.

Once the test statistic pdf is found, the observed limit is that which corresponds to $CL_s = 0.05$. The expected and $\pm 1, 2\sigma$ bands are taken as the median, 68% and 95% bands of the distribution at the μ value corresponding to $CL_s = 0.05$. When

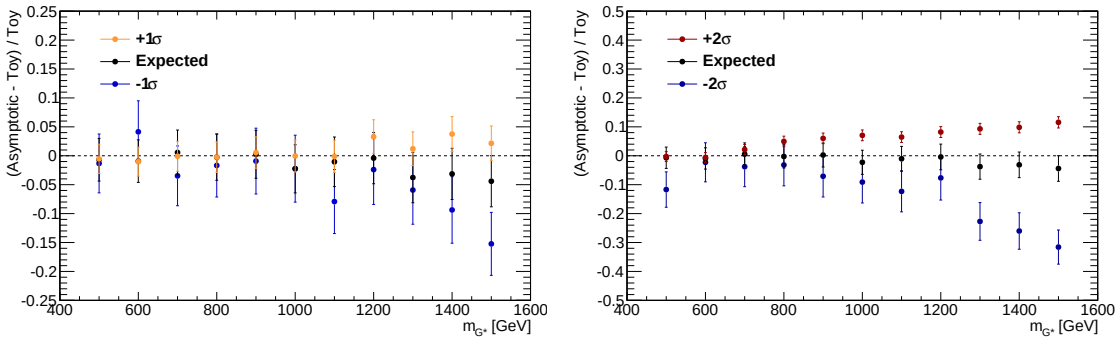

Figure 5.32.: The difference between the limits calculated using toy MC and those derived using the asymptotic approximation for the $k/\bar{M}_{Pl} = 1.0$ graviton signal model.

generating the expected upper limit, toy MC with $\mu = 0$ is used, rather than the actual data when constructing $\widetilde{q_\mu}$.

Treatment of Uncertainties

The uncertainties that are taken into account in the calculation of the limits are outlined in Section 5.5. They are all treated as uncorrelated with each other, and are treated as constraint terms in the profile likelihood. The shape systematics are treated as Gaussian with a linear interpolation between the values of the nominal and $\pm 1\sigma$ histograms, whereas the normalisation terms have an exponential interpolation which is equivalent to a log-normal constraint term with a linear interpolation between the histograms.

The luminosity uncertainty is applied to the signal and Z+jets MC as a normalisation systematic. The b-tagging and jet energy uncertainties are applied only to the signal MC, the jet energy uncertainties are treated as shape systematics whilst the b-tagging uncertainties are treated as normalisation. This is because they have a negligible impact on the shape of the $m_{4\mathrm{j}}$ distribution and because they are large they are better described by an effective log-normal constraint. For the jet energy resolution uncertainty, only the case where the JER is overestimated is considered so this is a conservative uncertainty. For the JES all 15 of the components are used but for the b-tagging uncertainty only components which make $> 1\%$ difference to the signal efficiency are considered.

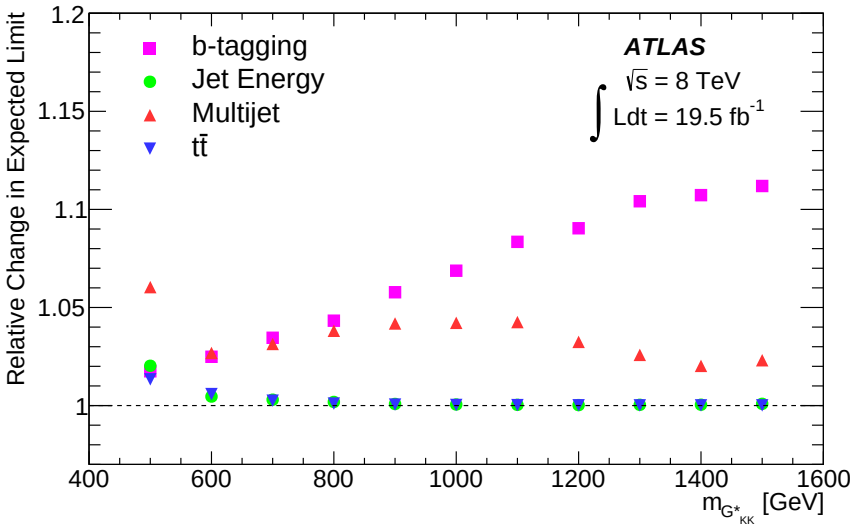

Figure 5.33.: The individual impact of the systematic uncertainties on the expected $\sigma(pp \to G^* \to hh \to b\bar{b}b\bar{b})$ 95% confidence level exclusion limit, as a function of graviton mass, for the $k/\bar{M}_{Pl} = 1.0$ graviton. The impact is the ratio of the limit calculated using all systematic uncertainties sources to the limit calculated using all systematic uncertainty sources excluding those under investigation.

Figure 5.33 shows the individual impact of the systematic uncertainties on the expected $\sigma(pp \to G^* \to hh \to b\bar{b}b\bar{b})$ 95% confidence level exclusion limit, as a function of graviton mass, for the $k/\bar{M}_{Pl} = 1.0$ graviton. The impact is the ratio of the limit calculated using all systematic uncertainties to the limit calculated with all except the one being investigated. At resonance masses $\leq$ 600 GeV, where most of the background is found, the multijet uncertainties dominate the impact on the limit. At masses $>$ 600 GeV, the b-tagging uncertainties become more important. This is due to the larger high-p_{T} uncertainties becoming more and more commonly used with increasing resonance mass.

Expected Limits

Figure 5.34 shows the expected exclusion limits for the $k/\bar{M}_{Pl} = 1.0$, 1.5 and 2.0 gravitons, taking into account all the sources of uncertainty listed in Section 5.6.2. 95% C.L. exclusion is expected for graviton masses below 700 GeV, 860 GeV and 930 GeV for $k/\bar{M}_{Pl} = 1.0$, 1.5, and 2.0 respectively. Figure 5.34d shows the expected exclusion limits for the search for a heavy neutral scalar boson, H, with

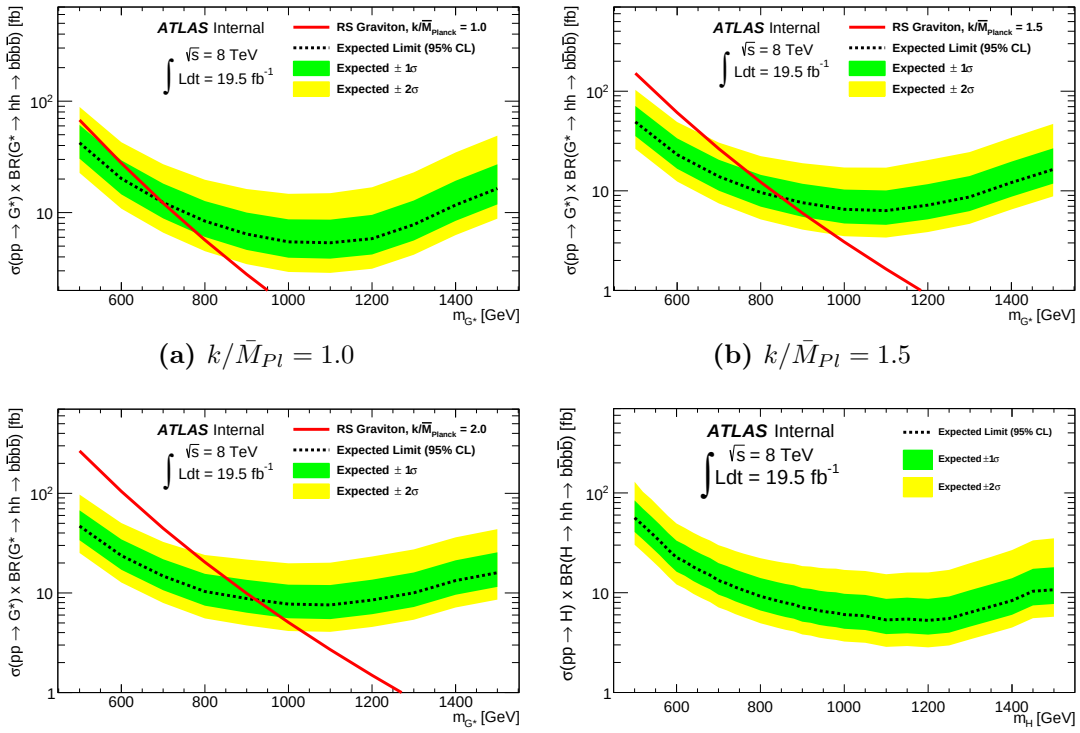

(a) $k/\bar{M}_{Pl} = 1.0$ **(b)** $k/\bar{M}_{Pl} = 1.5$

(c) $k/\bar{M}_{Pl} = 2.0$ **(d)** 2HDM

Figure 5.34.: The expected exclusion limits for **(a-c)** the RS graviton. 95% C.L. exclusion is expected for graviton masses below 700 GeV, 860 GeV and 930 GeV for $k/\bar{M}_{Pl} = 1.0$, 1.5, 2.0 respectively. **(d)** The expected exclusion limit for the 2HDM model H, with fixed $\Gamma_H = 1$ GeV. The exclusion limits are calculated including all systematic uncertainties.

fixed $\Gamma_H = 1$ GeV, again taking into account all the uncertainties listed in Section 5.6.2. This limit does not include a theoretical cross-section because the true Γ_H is dependent on 2HDM parameters. This limit is valid for scalar particles with widths smaller than the $m_{4\mathrm{j}}$ resolution, produced through gluon fusion, that decay to two Higgs bosons.

Figure 5.35 shows the expected limits for all four of the resonant signal models. One can see that they are all similar, with a large difference between the $k/\bar{M}_{Pl} = 1.0$ graviton sample and the 2HDM at the lowest mass coming from the $|\Delta\eta_{\mathrm{dijets}}|$ cut in the mass-dependent cuts giving the 2HDM sample a lower selection efficiency.

Table 5.10 shows the expected limits for SM $pp \to hh \to b\bar{b}b\bar{b}$ production.

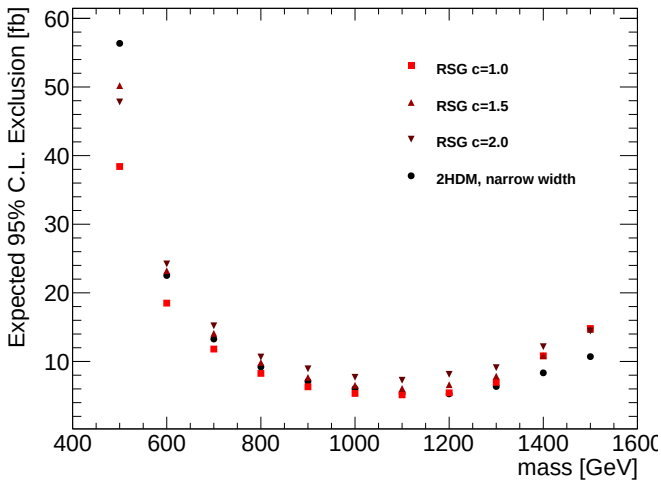

Figure 5.35.: The expected exclusion limits for the four signal models overlaid.

-2σ	-1σ	Central	$+1\sigma$	$+2\sigma$	
108	146	202	290	415	[fb]

Table 5.10.: Expected limits for SM hh production, $\sigma(pp \to hh \to b\bar{b}b\bar{b})$.

Comparison to Previous Result

Prior to this analysis, we made a simpler search for $pp \to G^* \to hh \to b\bar{b}b\bar{b}$, (ATLAS-CONF-2014-005) [76]. That analysis did not have the mass-dependent cuts, or the mass rescaling and had larger b-tagging uncertainties. Figures 5.36 and 5.37 compare the current result to that obtained in the previous version. There is significant improvement to the analysis sensitivity across the full mass range, with the largest gain at low mass coming from the lowering of the subleading dijet p_{T} threshold from 200 GeV to 150 GeV.

5.7. Results

5.7.1. Results of Unblinding

Table 5.11 shows the background prediction and the number of data events in the Signal Region. They are perfectly consistent. Figure 5.38 shows a comparison of the

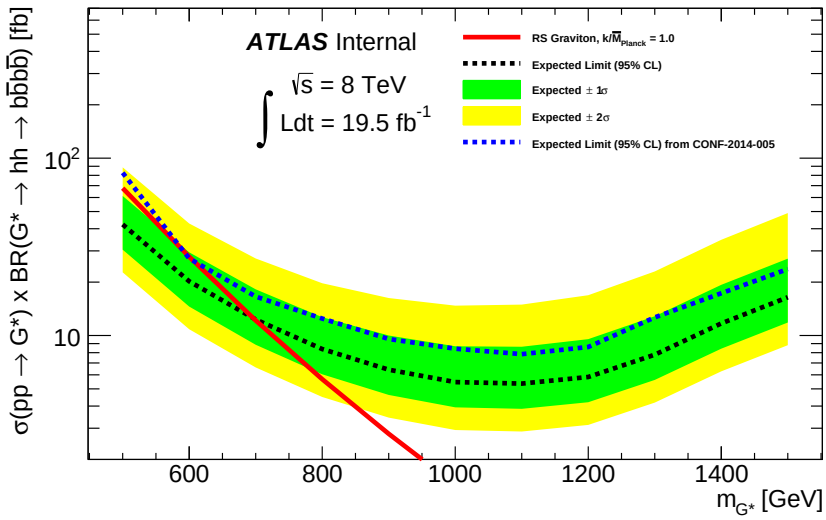

Figure 5.36.: The expected exclusion limits for the RS graviton with $k/\bar{M}_{Pl} = 1.0$ calculated including systematic uncertainties, compared to the previous analysis which is shown as the blue dashed line (Ref. [76]).

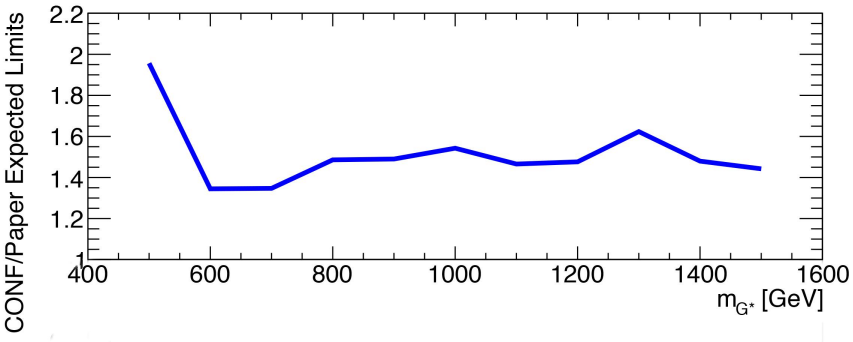

Figure 5.37.: Ratio of the expected exclusion limits for the RS graviton with $k/\bar{M}_{Pl} = 1.0$ calculated including systematic uncertainties, for this analysis and the previous one (Ref. [76]).

Sample	Signal Region
Multijet	81.4 ± 4.9
$t\bar{t}$	5.2 ± 2.6
Z+jets	0.4 ± 0.2
Total Bkgd	87.0 ± 5.6
Data	87

Table 5.11.: The number of predicted background events in the Signal Region, compared to the data. The uncertainty on the Z+jets number is purely statistical, reflecting the limited statistics in the Z+jets MC sample. The uncertainty on the $t\bar{t}$ and multijet is the full uncertainty on the data-driven methods, explained in Section 5.3.3 for the $t\bar{t}$ and Section 5.5.2 for the multijet. The statistical uncertainties on the number of events in the data are not shown.

predicted background vs. the data in the $m_{4\text{j}}$ distribution in the Signal Region. The agreement between the background distribution and the data is very good, with no obvious local excesses although there are features at $m_{4\text{j}} \sim 800$ GeV and $m_{4\text{j}} \sim 1200$ GeV.

Figure 5.39 shows an Event Display, made using Atlantis, of one of the data events from the Signal Region. It shows the typical event topology of a pair of boosted b-tagged dijets.

5.7.2. Background-only Hypothesis Tests

The background-only hypothesis is tested against the data using the procedure described in Section 5.6.1. Figure 5.40 shows the local p_0-value for the background-only hypothesis test as a function of the resonance mass for some of the signal models. The $k/\bar{M}_{Pl} = 1.0$ graviton sample has a similar distribution to the 2HDM model except that is has smaller peaks due to the slightly wider signal $m_{4\text{j}}$ width. There are no significant excesses observed, the maximum deviation from the background distribution is 2.1σ for the $pp \to H \to hh \to b\bar{b}b\bar{b}$ 2HDM signal with fixed width model at $m_{4\text{j}} = 1200$ GeV, this corresponds to a global p_0-value of 0.42σ. The data are consistent with the background-only hypothesis.

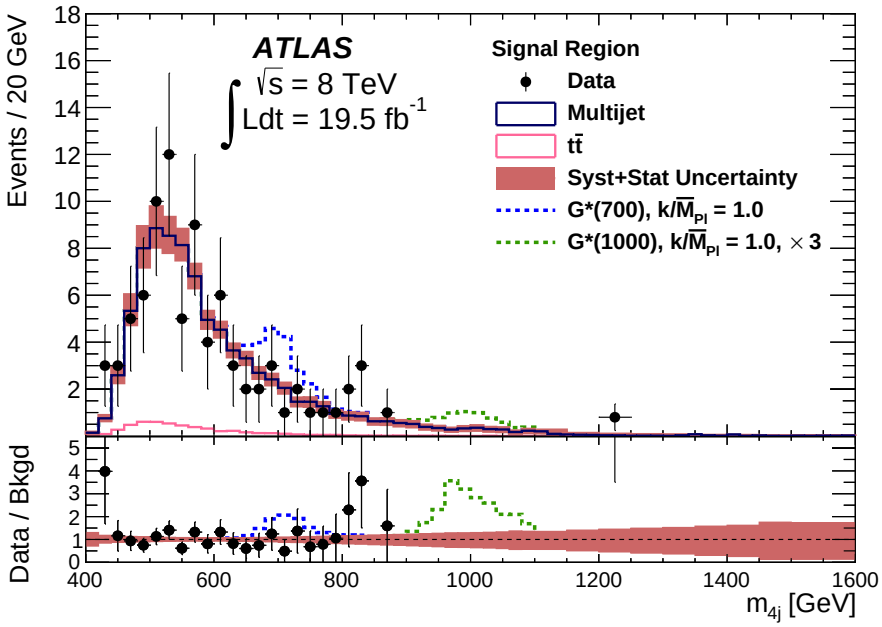

Figure 5.38.: Unblinded m_{4j} data in the Signal Region (shown as black points) compared to the background prediction (shown as red blocks, with height representing the uncertainty). Also shown are two examples of what a Graviton signal would look like.

5.7.3. Observed Limits and Exclusion

We use the data to set upper limits on the cross-section of the signal models, using the procedure described in Section 5.6.2. Figure 5.41 shows the expected and observed limit for the resonant signal models. The observed limit agrees well with the expected limit, is within the 1σ uncertainty band across most of the mass range, and within the 2σ uncertainty band across the whole mass range for all signals. The excluded mass ranges for the bulk RS KK graviton are shown in Table 5.12. The excluded mass range for the 2HDM is parameter dependent, principally because the production cross-section varies, but also because the exclusion limit depends on the parameter-dependent H boson width, Γ_H. As such it is not shown here, but can be found in the paper (Ref. [1]). The limit shown is valid for narrow scalar particles produced through gluon fusion, that decay to two Higgs bosons.

The observed upper limit on non-resonant SM hh at 95% CL is $\sigma(pp \to hh \to b\bar{b}b\bar{b})$ = 202 fb. This can be compared to the inclusive SM prediction (as defined in Section 5.1) of $\sigma(pp \to hh \to b\bar{b}b\bar{b}) = 3.6 \pm 0.5$ fb.

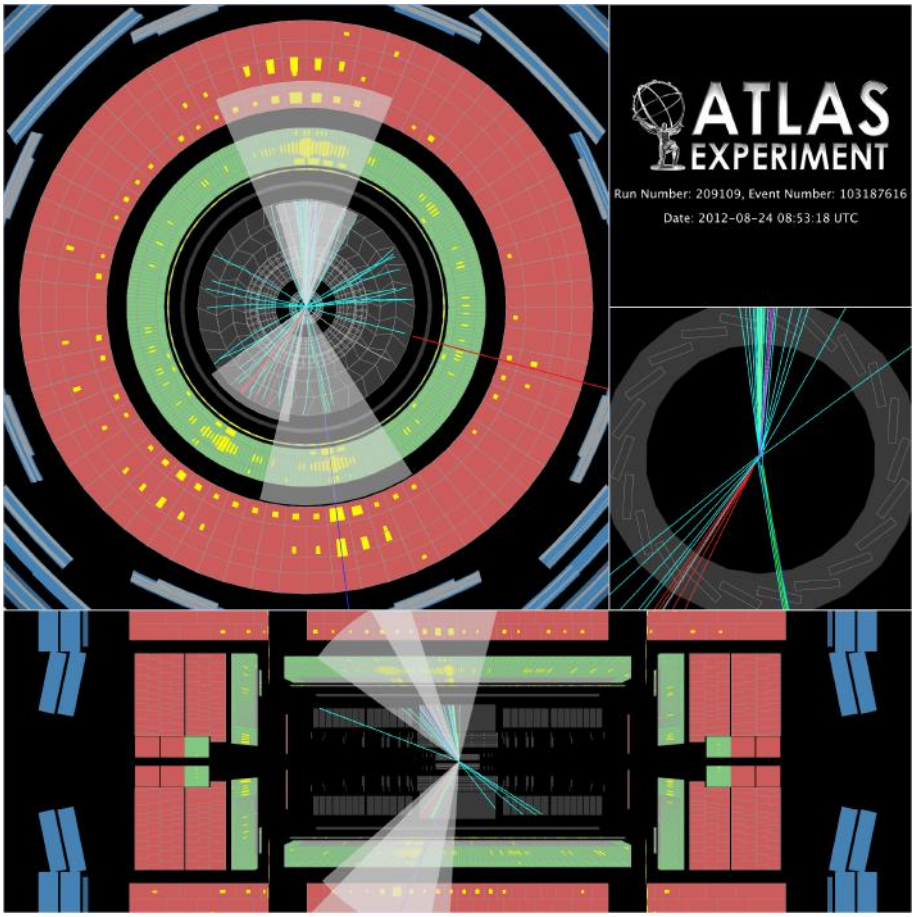

Figure 5.39.: A display of an event passing the full selection. The reconstructed $m_{4\mathrm{j}}$ = 809 GeV. The leading dijet p_{T} = 394 GeV and $m_{2\mathrm{j}}^{\mathrm{lead}}$ = 114 GeV. The subleading dijet p_{T} = 333 GeV and $m_{2\mathrm{j}}^{\mathrm{subl}}$ = 123 GeV. The white cones indicate the size of the jets.

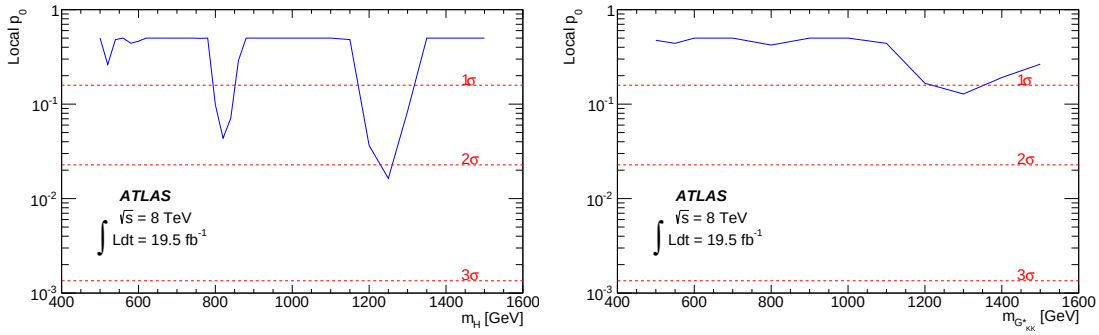

(a) 2HDM **(b)** $k/\bar{M}_{Pl} = 2.0$

Figure 5.40.: The local p_0-value distributions for the background-only hypothesis test (see Section 5.6.1) as a function of the resonant signal mass.

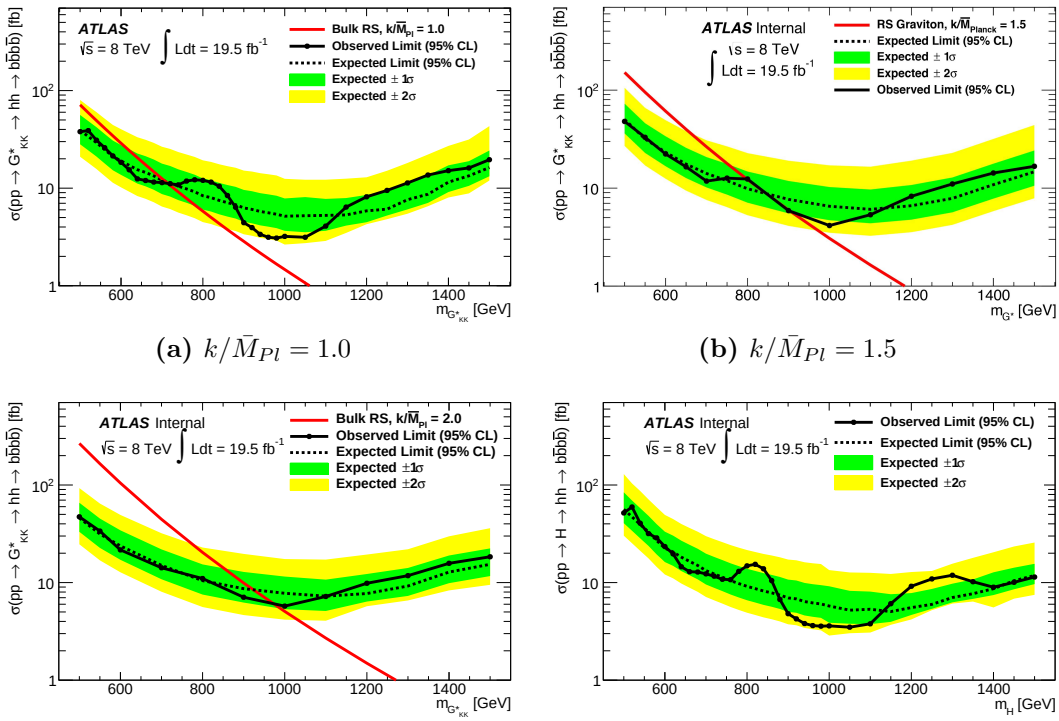

(a) $k/\bar{M}_{Pl} = 1.0$ **(b)** $k/\bar{M}_{Pl} = 1.5$

(c) $k/\bar{M}_{Pl} = 2.0$ **(d)** 2HDM

Figure 5.41.: The expected and observed limit for: **(a-c)** the RS Graviton and **(d)** the 2HDM heavy neutral scalar boson with fixed $\Gamma_H = 1$ GeV.

$k/\bar{M}_{Pl}$	95% CL Excluded G^* KK Mass Range [GeV]
1.0	500 - 720
1.5	500 - 800 and 870 - 910
2.0	500 - 990

Table 5.12.: The range of KK graviton masses excluded at 95% confidence level for $k/\bar{M}_{Pl} = 1.0$ 1.5, 2.0.

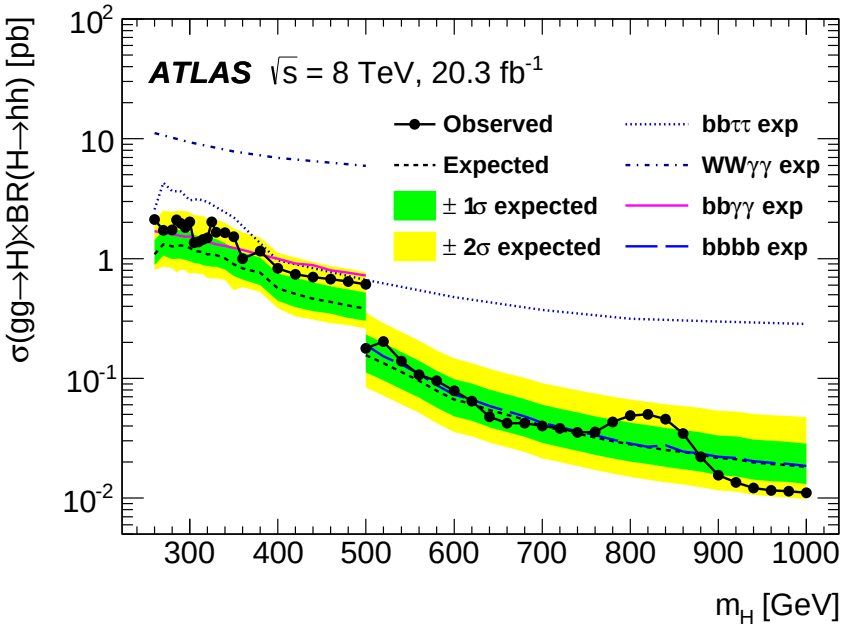

Figure 5.42.: The observed and expected 95% CL upper limits on $\sigma(gg \to H) \times BR(H \to hh)$ at $\sqrt{s} = 8$ TeV as functions of the heavy Higgs boson mass m_H, combining resonant searches in $hh \to \gamma\gamma b\bar{b}$, $b\bar{b}b\bar{b}$, $b\bar{b}\tau\tau$ and $\gamma\gamma WW^*$ final states. The expected limits from individual analyses are also shown. The combination assumes SM values for the decay branching ratios of the lighter Higgs boson h [30].

5.7.4. Comparisons with Other ATLAS Higgs Boson Pair Production Searches

Figure 5.42 shows the expected and observed 95% limits on $\sigma(gg \to H) \times BR(H \to hh)$ for the ATLAS $\sqrt{s} = 8$ TeV, $H \to hh$ searches [30]. This includes the $hh \to \gamma\gamma b\bar{b}$, $b\bar{b}b\bar{b}$, $b\bar{b}\tau\tau$ and $\gamma\gamma WW^*$ final states and their combination. In the range $m_H > 500$ GeV, where the $b\bar{b}b\bar{b}$ final state is investigated, it is the most sensitive, giving an expected limit which is $\mathcal{O}(10)$ times more sensitive than the $b\bar{b}\tau\tau$ channel. Extending the search range of the $hh \to b\bar{b}b\bar{b}$ analysis below $m_H = 500$ GeV could improve the combined limit, however the analysis would encounter large challenges from triggering and the large mutijet background. The non-resonant observed (expected) upper limit for $\sigma(gg \to hh)$ when combining the final states listed is 0.69 (0.47) pb which can be compared to 0.62 (0.62) for the $b\bar{b}b\bar{b}$ channel alone. This degradation is due to a 2.4σ excess in the $\gamma\gamma b\bar{b}$ result.

5.8. Conclusions

Two searches for Higgs boson pair production in the $b\bar{b}b\bar{b}$ final state with the ATLAS detector at the LHC have been performed: one for resonant $pp \to X \to hh \to b\bar{b}b\bar{b}$; the other for non-resonant production. The Higgs boson candidates are reconstructed from pairs of nearby b-tagged jets which form boosted dijets. Due to the large branching ratio of $h \to b\bar{b}$ and the large background rejection factors offered by the boosted dijet topology the sensitivity for Higgs boson pair production is extremely good: the observed 95% confidence level exclusion for $\sigma(pp \to X \to hh \to b\bar{b}b\bar{b})$ at 1 TeV is 3.2 fb. This excellent sensitivity results in constraints on our benchmark models: for the $k/\bar{M}_{Pl} = 1.0$ RS KK graviton, we exclude $500 \leq m_{G^*} \leq 720$ GeV. For non-resonant signals, using the SM hh non-resonant production as the benchmark, the observed 95% confidence level exclusion was $\sigma(pp \to hh \to b\bar{b}b\bar{b}) = 202$ fb, which is in good agreement with the expected exclusion.

Chapter 6.

Future Searches for $pp \to hh \to b\bar{b}b\bar{b}$ at $\sqrt{s} = 14$ TeV

This chapter focuses on two simulation-based studies looking for $pp \to hh \to b\bar{b}b\bar{b}$ at $\sqrt{s} = 14$ TeV. These results are relevant to Run 2 of the LHC and also the HL-LHC. Section 6.2 presents a non-resonant search which is published in Ref. [2]. Section 6.3 presents an unpublished study on the search for resonant $pp \to hh \to b\bar{b}b\bar{b}$ with the Randall-Sundrum Kaluza-Klein Graviton (G^*), with $k/\bar{M}_{Pl} = 1.0$, as the benchmark signal. In this study a new method for reconstruction is proposed.

6.1. Common Analysis Methods

6.1.1. Jets

Both studies here are particle-level studies. The jets are "truth" jets, meaning that they are reconstructed from stable particles in the event record. All jets are required to pass the following requirements:

- $p_{\mathrm{T}} > 40$ GeV
- $|\eta| < 2.5$

If a jet passes these requirements it is given a weight according to its truth flavour using the method described below.

6.1.2. *b*-tagging

Jets are flavour labelled according to the truth record as described in Section 4.2. To mimic a 70% working point for b-tagging they are given a weight dependent on that flavour so b-jets have a weight of 0.7, c-jets a weight of 0.2 and light-jets a weight of 0.01. Each event is then weighted by the product of the chosen jets individual b-weights.

6.2. A Non-Resonant Search for $pp \to hh \to b\bar{b}b\bar{b}$

6.2.1. Signal Topology

The signal Monte Carlo used in this analysis was generated with MadGraph 1.5.12 [71] and showered with Pythia 8.175 [65], using the CTEQ6L1 PDF set [77].

Figure 6.1a shows the p_{T} distribution for the Higgs bosons in signal events. A large fraction of the events (36.6%) have $p_{\mathrm{T}} > 150$ GeV for both Higgs bosons, this falls to 16.6% and 3.6% for 200 GeV and 300 GeV cuts.

Figure 6.1b shows the efficiency to reconstruct Higgs bosons as a function of Higgs boson p_{T} using two methods. The first method is using two anti-k_t R = 0.4 jets which form dijets where the jets pass the cuts outlined in Section 6.1.1 and the jet pairs have $\Delta R_{jet1,jet2} < 1.5$ and a combined $p_{\mathrm{T}} > 150$ GeV. For a Higgs boson to be reconstructed in this way it must have one of its b-quarks in each jet. The second reconstruction method uses Cambridge-Aachen R = 1.2 jets which have two k_t R = 0.3 subjets. The Cambridge-Aachen jets must have $p_{\mathrm{T}} > 80$ GeV and the subjets must have $p_{\mathrm{T}} > 40$ GeV. In this case, the reconstruction requires that both of the Higgs boson b-decays are contained within a single Cambridge-Aachen jet, whilst the b-quarks are contained within separate subjets. The reconstruction efficiency is defined as the ratio of reconstructed Higgs bosons to all Higgs bosons. Up to ~ 400 GeV the anti-k_t jets have a better reconstruction efficiency. This is in line with Figure 6.1c which shows the angular separation between the b-quarks from a Higgs boson decay with respect to the Higgs boson p_{T}. At low Higgs boson p_{T} it is rare for the b-quarks to be within $\Delta R < 1.2$ so they cannot be reconstructed by the Cambridge-Aachen jets used here. At higher Higgs boson p_{T}'s the anti-k_t reconstruction falls rapidly

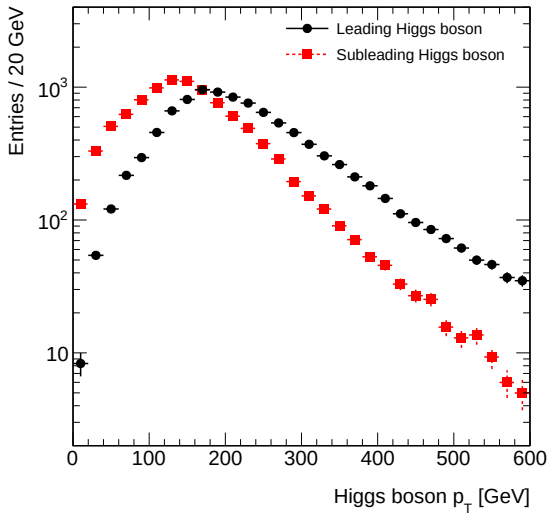

(a)

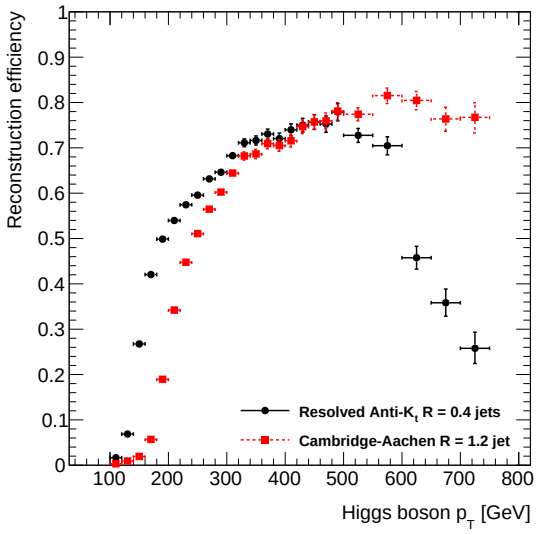

(b)

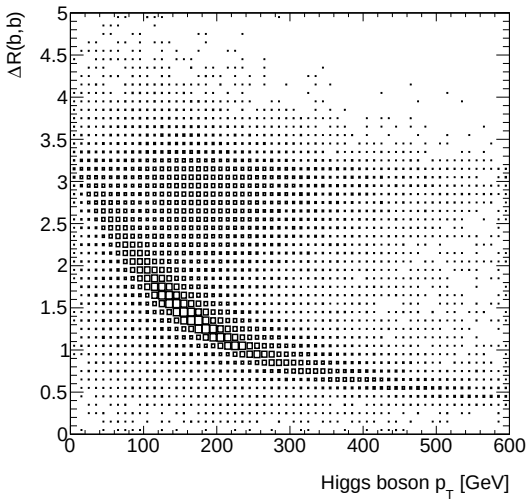

(c)

Figure 6.1.: Signal topology distributions for the SM hh signal showing: **(a)** the p_{T} distributions of the leading (circles) and sub-leading (squares) Higgs bosons, **(b)** the efficiency for reconstructing correctly the Higgs boson from two anti-k_t jets with R = 0.4 (circles) or from a single Cambridge-Aachen jet with R = 1.2 (squares), and **(c)** the distance ΔR between the two b-quarks from the Higgs boson decay as a function of the Higgs boson p_{T}.

($p_{\mathrm{T}} > 500$ GeV) here the decay products are starting to merge into a single R = 0.4 jet. This is not a problem for the search for $pp \to hh \to b\bar{b}b\bar{b}$ as the majority of the signal is at lower p_{T}.

6.2.2. The Analysis

From the information found in the signal topology studies it was determined that for the Standard Model $pp \to hh \to b\bar{b}b\bar{b}$ search it would be best to reconstruct the Higgs bosons using anti-k_t R = 0.4 dijets. The dijets were required to have $p_{\mathrm{T}} > 150$ GeV, $\Delta R_{jet1,jet2} < 1.5$ and $100(85) < m_{dijet} < 140(130)$ GeV for the leading (sub-leading) dijet. After this two Boosted Decision Trees (BDT) were used to distinguish the signal from the background. The background consists of QCD $b\bar{b}b\bar{b}$, QCD $b\bar{b}c\bar{c}$, $t\bar{t}$, and single Higgs samples. The first BDT was based on the $t\bar{t}$ veto used in Section 5.2.4, and the second one took as input the output of the first and also ten kinematic and angular variables which were proposed in Ref. [98] and used in Ref. [99] for an $h \to ZZ^* \to 4l$ analysis at the LHC.

The resulting statistical significance ($s/\sqrt{b}$) for 3000 fb^{-1} was 0.9 after the dijet mass window selection and this doubled to 1.8 after the two BDTs. This can be compared with the analysis presented in Ref. [100] which used Cambridge-Aachen R = 1.2 jets and substructure techniques, which, when applying their techniques to our MC samples, achieved a significance of 0.7.

6.3. Resonant Searches for $pp \to G^* \to hh \to b\bar{b}b\bar{b}$

6.3.1. Monte Carlo Samples

The signal used in this study is a spin-2 Randall-Sundrum Kaluza-Klein Graviton $pp \to G^* \to hh \to b\bar{b}b\bar{b}$, described in Section 2.2.1, with $k/\bar{M}_{Pl} = 1.0$ where $\bar{M}_{Pl}$ is the reduced Planck Mass. There are samples in the range from $1 \leq m_{G^*} \leq 3$ TeV in 500 GeV intervals. The Graviton samples are generated with MadGraph v1.5.1 [71] and showered with pythia v8.175 [65]. The PDFs used are CTEQ6L1 [77].

The dominant background of QCD multijets is generated using Sherpa 2.1.1 [70] using the CT10 [101] PDF set. The samples are scaled to their NLO cross-sections by applying a k-factor of 1.5 [102]. There are three samples, all filtered at parton level to require two partons with $p_{\mathrm{T}} > 65$ GeV and either one parton with $p_{\mathrm{T}} > 250$ GeV or four partons with $p_{\mathrm{T}} > 20$ GeV. Partons are simulated by anti-k_t jets with distance parameter R = 0.1 and are required to have $|\eta| < 2.7$. The three samples are

generated with differing extra requirements to ensure good statistics in the high mass tail (in m_{hh}). The lowest mass sample is required to have the invariant mass of the combination of its two (m_{12}), three (m_{123}) and four (m_{1234}) leading partons to be less then 1 TeV; partons here are outgoing particles in the ME which can be u-, d-, c-, s-, b-quarks, their corresponding anti-quarks, or gluons. The middle sample is required to have $m_{12}, m_{123}, m_{1234} < 2$ TeV and at least one of m_{12}, m_{123}, and $m_{1234} > 1$ TeV. The highest mass sample is required to have at least one of m_{12}, m_{123}, and $m_{1234} > 2$ TeV.

The subdominant background of $t\bar{t}$ is generated with POWHEG [66, 67] interfaced to PYTHIA 8.185 using the CT10 PDF set. $t\bar{t}$ events with W boson decays to electrons and muons, or where both W bosons decay to light-jets are not simulated, since these decays are heavily suppressed by the b-tagging in the event selection.

6.3.2. Signal Topology

Figure 6.2a shows the p_{T} distribution for the Higgs bosons and Figure 6.2b shows the angular separation, between the b-decays of the Higgs bosons with respect to the Higgs boson p_{T} in three of the graviton signal samples. Both figures show an expected trend: as the mass of the graviton increases, the Higgs bosons are given a larger boost in p_{T} and because of that the angular separation between the b-quarks decreases. This angular separation can be roughly evaluated by Equation 6.1:

$$\Delta R \approx \frac{2m}{p_T} \tag{6.1}$$

where ΔR is the angular separation between the decay products, and m and p_{T} are the mass and p_{T} of the decaying particle.

Due to this large range in ΔR separation between the b-quarks, using one kind of Higgs boson reconstruction, such as the dijet method used in the non-resonant search (and in Chapter 5), will not be efficient across the whole mass range. Figure 6.2c shows the efficiency for different jet combinations to reconstruct the Higgs bosons in the graviton samples. The different jet combinations shown are:

- 2 anti-k_t R = 0.4 jets with $p_{\mathrm{T}} > 40$ GeV and $\Delta R < 1.5$. They must have a combined $p_{\mathrm{T}} > 80$ GeV. This is the dijet method used previously. For a Higgs

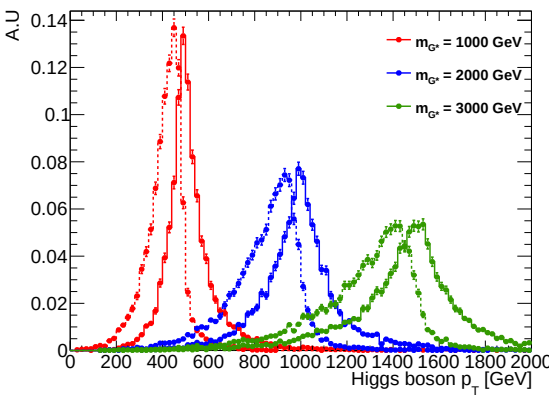

(a)

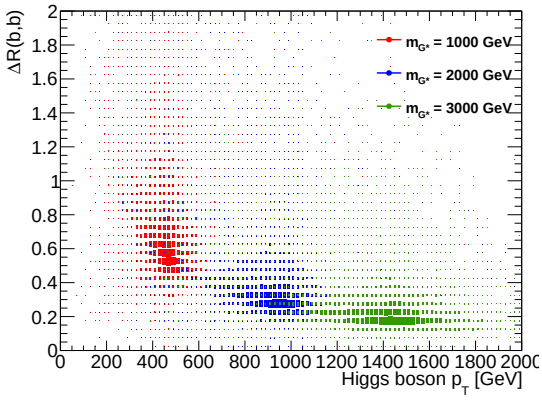

(b)

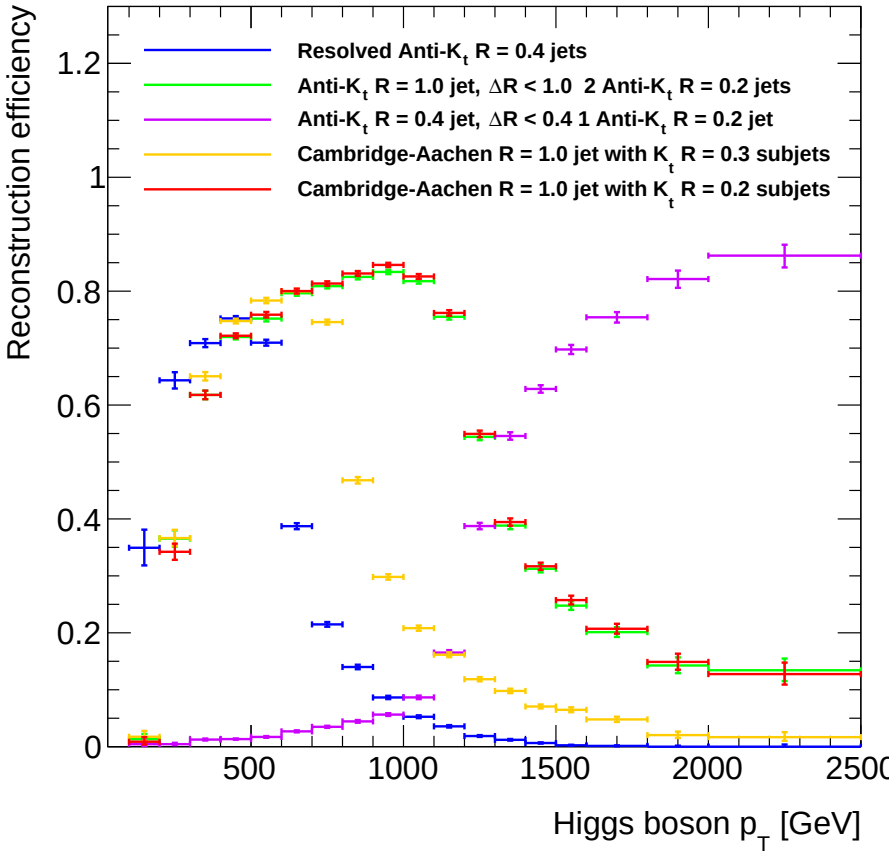

(c)

Figure 6.2.: Signal Topology distributions for three of the graviton samples, showing: **(a)** the p_{T} distributions of the leading (full lines) and sub-leading (dashed lines) Higgs bosons and **(b)** the distance ΔR between the two b-quarks from the Higgs boson decay as a function of the Higgs boson p_{T}. **(c)** The efficiency for reconstructing correctly the Higgs boson for different jet combinations for all the graviton samples.

boson to be successfully reconstructed in this method, each of its b-quarks needs to be in a separate jet.

- 1 anti-k_t R = 1.0 jet with $p_{\mathrm{T}} > 80$ GeV which has $\Delta R < 1.0$ to 2 anti-k_t R = 0.2 jets with $p_{\mathrm{T}} > 40$ GeV. For a Higgs boson to be successfully reconstructed in this method, both of its b-quarks need to be contained in the R = 1.0 jet and contained separately in each R = 0.2 jet.

- 1 anti-k_t R = 0.4 jet with $p_{\mathrm{T}} > 80$ GeV which has $\Delta R < 0.4$ to 1 anti-k_t R = 0.2 jet with $p_{\mathrm{T}} > 40$ GeV. For a Higgs boson to be successfully reconstructed in this method, both of its b-quarks need to be contained in the R = 0.4 jet and also both in the R = 0.2 jet.

- 1 Cambridge-Aachen R = 1.0 jet with $p_{\mathrm{T}} > 80$ GeV which has been reclustered with k_t R = 0.3 subjets. For a Higgs boson to be successfully reconstructed in this method, each of its b-quarks needs to be contained in the R = 1.0 jet and they also need to be contained in separate subjets with $p_{\mathrm{T}} > 40$ GeV.

- 1 Cambridge-Aachen R = 1.0 jet with $p_{\mathrm{T}} > 80$ GeV which has been reclustered with k_t R = 0.2 subjets. For a Higgs boson to be successfully reconstructed in this method, each of its b-quarks needs to be contained in the R = 1.0 jet and they also need to be contained in separate subjets with $p_{\mathrm{T}} > 40$ GeV.

This plot is the combination of efficiencies for all the graviton samples. At low Higgs boson p_{T} (< 500 GeV) the dijet method used previously has the highest efficiency. At higher Higgs boson p_{T} the dijet method efficiency falls dramatically due to the fact that the decay products of the Higgs boson start to merge into a single R = 0.4 jet. At this point the R = 1.0 jets have a higher efficiency. The efficiency drop for the R = 1.0 jets depends on the size of the subjets. The Cambridge-Aachen jet with R = 0.3 subjets starts to loose its efficiency at a p_{T} of ~ 700 GeV which is where it becomes harder to resolve the b-quarks into separate R = 0.3 jets. For the R = 0.2 subjets, the peak in efficiency happens at a Higgs boson p_{T} of ~ 1 TeV. The anti-k_t and Cambridge-Aachen jets have a very similar efficiency curve. For higher Higgs boson p_{T} the b-quarks have merged into a single R = 0.2 jet. For this reason the anti-k_t R = 0.4 jet which has been matched to a R = 0.2 jet (used to simulate a track jet which would be used for high p_{T} b-tagging) has an increasing efficiency.

To obtain a high efficiency of Higgs boson reconstruction in a search range with resonance mass between 1 TeV $\leq m_X \leq$ 3 TeV, it is clear that the combination of different reconstruction methods, where the radius of the jets decreases as the p_{T} increases, is essential. For this reason, we introduce a new reconstruction method to look for "Higgs Candidates" (HCs). In this method, multiple reconstruction techniques are used to identify Higgs bosons, rather than the use of one method. In doing this, a high signal efficiency can be achieved throughout the graviton mass range, without having to perform multiple, separate searches.

Figure 6.3 shows the three types of HCs we have used. The first is called "Resolved", this is used to reconstruct low p_{T} Higgs bosons and is the dijet method used in the non-resonant search and the ATLAS analysis of Chapter 5. As Higgs bosons increase in p_{T} and their b-quarks start to merge into one jet we move to the "Semi-Merged" case, here Higgs bosons are reconstructed via one jet, but it must be double b-tagged by ΔR matching with two b-tagged track jets (in this study we simulate track jets with anti-k_t R = 0.2 particle jets)[1]. To reduce the number of background events getting reconstructed using Semi-Merged HCs, there is an additional requirement that the jet $p_{\mathrm{T}} > 300$ GeV. Finally, as the Higgs boson boost increases further and its b-quarks have a $\Delta R < 0.2$ we use the "Fully Merged" case, this is the same as the Semi-Merged except that it is required to match to only one b-tagged track jet and the jet $p_{\mathrm{T}} > 600$ GeV.

Figure 6.4a shows the efficiency to reconstruct Higgs bosons using Higgs Candidates with differing R parameters for the HCs. The lines shown are the "ORs" of the different combinations of Resolved, Semi-Merged and Fully Merged. All HCs have to pass the additional mass constraint $85 < m_{HC} < 140$ GeV. The jet algorithm used for all of them is the anti-k_t algorithm. The anti-k_t R = 1.0 jets have been trimmed by reclustering their constituents into k_t subjets with distance parameter R = 0.2 and removing any of these subjets which have a p_{T} less than 5% of the original jet p_{T}. The combination of using R = 0.4 for the distance parameter of all the HCs has the best overall efficiency. Figure 6.4b shows the break down of how the different HCs contribute towards the overall efficiency of reconstructing the Higgs bosons, when

[1] In Ref. [103], ATLAS presented a multivariate discriminant to identify double b-tagged anti-k_t R = 0.4 jets (jets which contain two b-hadrons). This method was not investigated in this analysis where the simpler method of matching b-tagged track jets to the jets and high p_{T} requirements have been used instead.

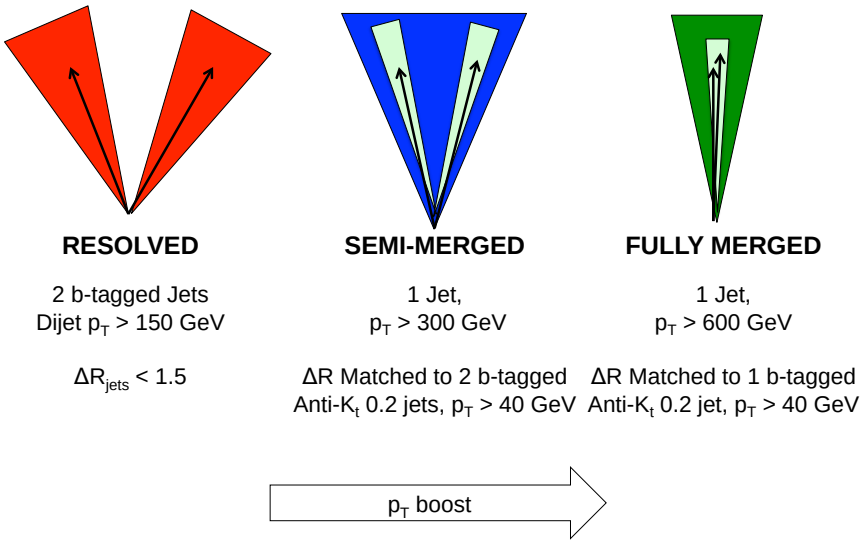

Figure 6.3.: The three types of "Higgs Candidate".

using the chosen method of anti-k_t R = 0.4 jets. There is a high efficiency for Higgs boson $p_{\mathrm{T}} > 400$ GeV, with the efficiency being > 0.8 for Higgs boson $p_{\mathrm{T}} > 700$ GeV.

6.3.3. Event Selection

Jet Criteria

Jets are reconstructed with the anti-k_t algorithm with a radius parameter of 0.4 and also of 0.2. If there are at least two anti-k_t R = 0.4 jets in the event that pass the requirements in Section 6.1.1 then we attempt to reconstruct Higgs Candidates (HCs) using the definitions outlined below.

Higgs Candidate Definitions: Resolved

The formation of resolved Higgs Candidates follows the same selection as the dijets in Section 6.2, they are constructed by pairing up any jets which satisfy the following criteria:

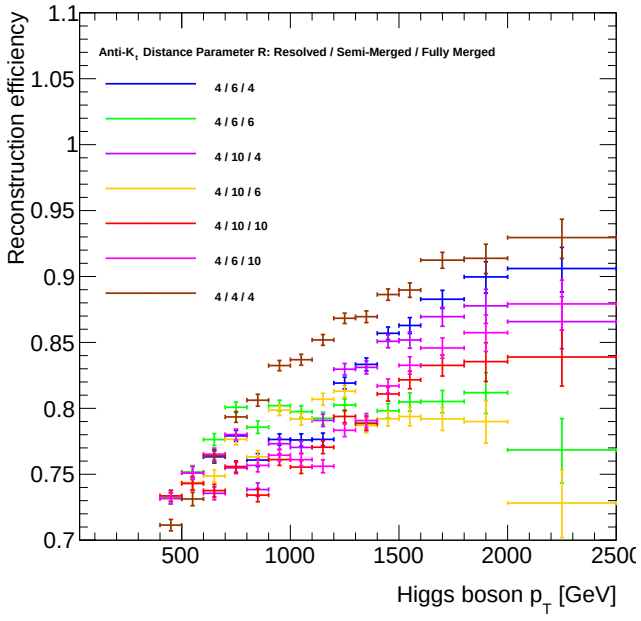

(a)

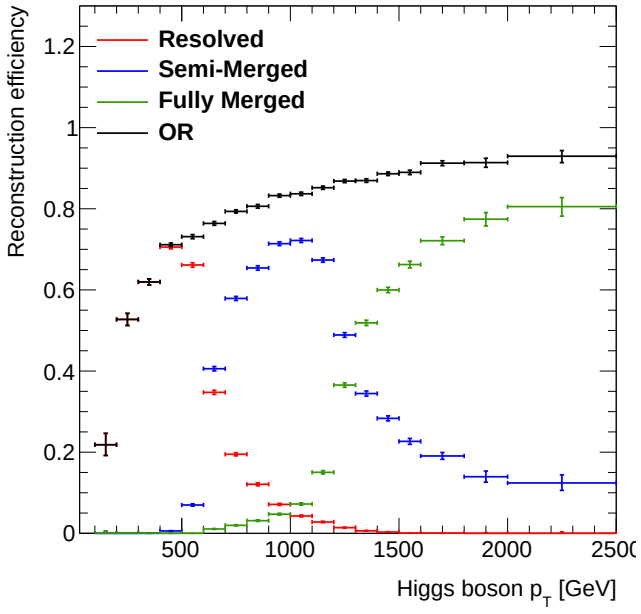

(b)

Figure 6.4.: The efficiency of different jet combinations to reconstruct the Higgs bosons in the graviton samples. **(a)** The OR of different combinations. The numbers in the legend denote the radius parameter $R \times 10$ for each of the HC categories. For example, "4 / 10 / 6" (the yellow points) means that the Resolved HC jets have R = 0.4, the Semi-Merged large jets have R = 1.0 and the Fully-Merged large jets have R = 0.6. The subjets always have R = 0.2. **(b)** The different Higgs Candidate contributions towards the OR when using a distance parameter for R = 0.4 for all the HCs.

- Magnitude of the vectorial sum of the two jets momenta in the transverse plane $(\mathbf{p}_{\text{jet1}} + \mathbf{p}_{\text{jet2}})_{\text{T}} > 150$ GeV
- Angular separation of the jets $\Delta R_{jet1,jet2} < 1.5$
- Invariant mass of the two jets $85 < m_{HC} < 140$ GeV

In the case where a jet can be used to create more than one Resolved HC, the HC which is sub-leading when ordered by b-tag weight, then p_{T} is discarded. The b-tag weight assigned to each Resolved HC is the product of the b-tag weights of the two jets it comprises.

Higgs Candidate Definitions: Semi-Merged

Semi-Merged Higgs Candiates are formed from the anti-k_t R = 0.4 jets (Jet_4) which also satisfy the following criteria:

- $p_{\text{T}} > 300$ GeV
- There are at least two anti-k_t R = 0.2 jets (jet_2) which fulfil $p_{\text{T}} > 40$ GeV and $\Delta R_{Jet_4,jet_2} < 0.4$
- Invariant mass of the Jet_4 $85 < m_{HC} < 140$ GeV

The b-tag weight assigned to each Semi-Merged HC is the product of the b-tag weights of the two subjets which have been matched to it. If more than two anti-k_t R = 0.2 jets are matched to a Semi-Merged HC then the two which are leading and sub-leading in b-tag weight, then p_{T} are chosen. The kinematics of the HC are taken from the anti-k_t R = 0.4 jet.

Higgs Candidate Definitions: Fully Merged

Fully Merged Higgs Candidates are formed from any of the anti-k_t R = 0.4 jet collection which have failed the Semi-Merged selection but also pass:

- $p_{\text{T}} > 600$ GeV
- There is one anti-k_t R = 0.2 jet with $p_{\text{T}} > 40$ GeV and $\Delta R_{Jet_4,jet_2} < 0.4$
- Invariant mass of the Jet_4 $85 < m_{HC} < 140$ GeV

The b-tag weight assigned to the Fully Merged candidate is the b-tag weight of the anti-k_t R = 0.2 subjet. The kinematics of the HC are taken from the anti-k_t R = 0.4 jet.

Higgs Candidate Requirements

Once the HC reconstruction has taken place the HCs are ordered by b-tag weight and then p_{T}. If the leading and sub-leading HCs share a jet then the sub-leading HC is discarded. This is repeated until the leading and sub-leading HCs are not overlapping. An event is discarded if less than two Higgs Candidates can be reconstructed.

Figure 6.5 shows the efficiency for each signal sample to reconstruct two Higgs Candidates, before and after the b-tag weighting is applied. It also shows the composition of the events passing in terms of Higgs Candidate types. It can be seen that as the Graviton mass increases the typical HC composition migrates from Resolved-Resolved up to Fully Merged-Fully Merged. The efficiency gained from combinations where the two HCs are made from separate types, such as Resolved-Semi-Merged, ensures that there is a high efficiency for all graviton masses under study. This also shows the benefit of using this type of reconstruction method over performing two separate analyses and then combining the results because these events would have been missed.

The single b-tagging used in the case of Fully Merged candidates means that once the b-tag weighting has been applied the efficiency increases as the graviton mass increases, (Figure 6.5b).

Additional Requirements

Figure 6.6 shows some kinematic distributions for the total background and some of the signal samples once two Higgs Candidates have been reconstructed. Figure 6.6a shows the mass of the leading HCs (in b-tag weight then p_{T}), the gravitons have a peak at 125 GeV whereas the background is quite flat across the range. By increasing the minimum mass from 85 to 100 GeV the total background is reduced by 34% whilst the decrease in signal ranges between 5-7%.

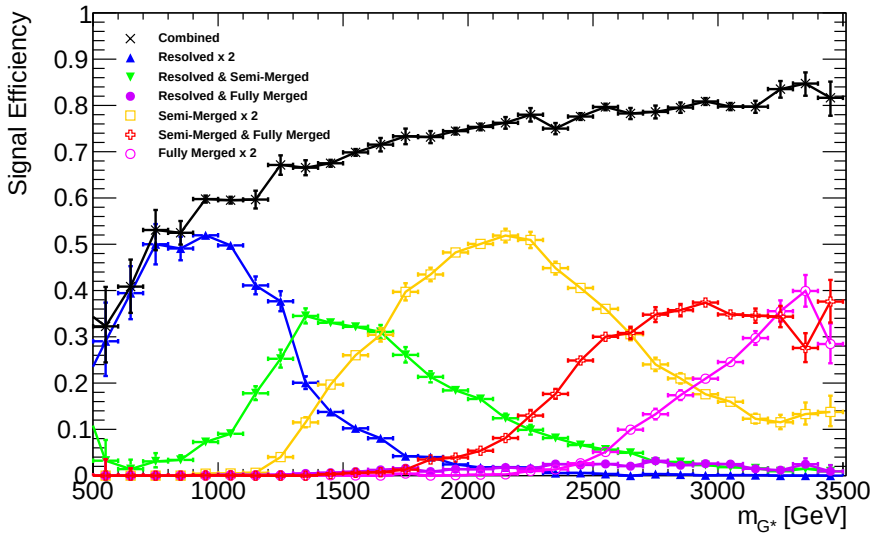

(a) Before b-tag Weighting

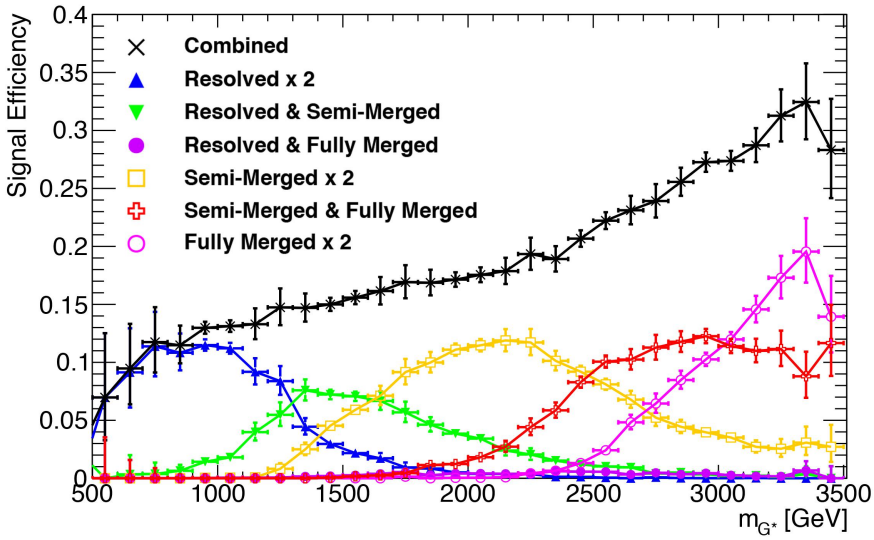

(b) After b-tag Weighting

Figure 6.5.: The efficiency of the graviton samples to pass the requirements in Section 6.3.3 as a function of graviton mass. Also shown is the composition of the events passing in terms of Higgs Candidates types.

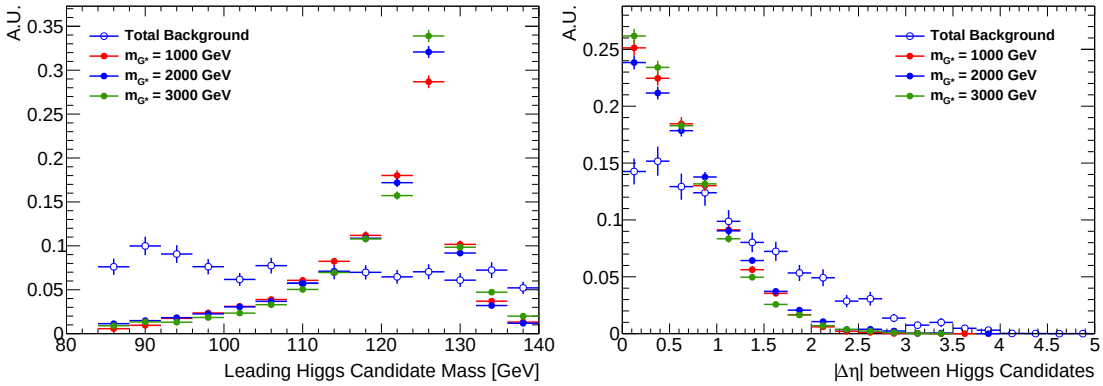

(a) **(b)**

Figure 6.6.: **(a)** The leading Higgs Candidate mass. **(b)** The absolute difference in pseudorapidity between the Higgs Candidates. Both shown after the b-tag weighting has been applied.

Figure 6.6b shows the absolute difference in pseudorapidity between the two Higgs Candidates. All distributions peak at $|\Delta\eta| = 0$ but the total background has a wider spread. Requiring $|\Delta\eta| < 2$ reduces the signal efficiency by a further 1-2% but reduces the total background by 14%.

For these reasons, if two HCs are found then they must pass the following criteria:

- For the leading HC: $100 < m_{HC} < 140$ GeV
- $|\Delta\eta| < 2.0$

Signal Region Definitions

The results of this study are presented as simple s/b and $s/\sqrt{b}$ values. Figure 6.7 shows the invariant mass of the two Higgs Candidates, m_{2HC}, after the full event selection. Due to the large, steeply falling background distribution and small predicted cross-sections of the higher mass gravitons, to obtain the s/b and $s/\sqrt{b}$ values the m_{2HC} range is split into windows around each signal sample mass. The windows have been chosen so that they include the full width at half maximum for each resonant peak. These windows are outlined in Table 6.1.

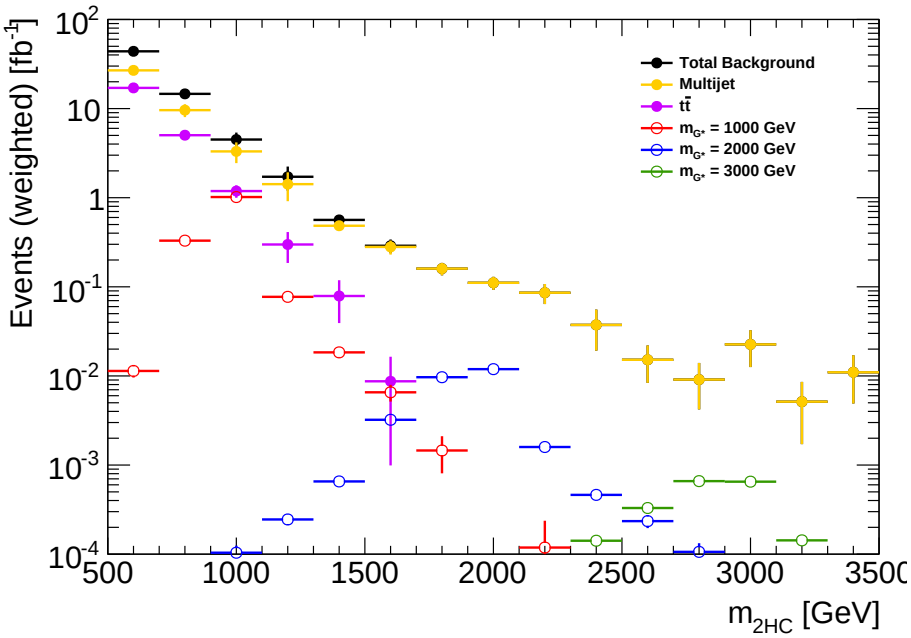

Figure 6.7.: The m_{2HC} distribution for the total background and some of the signal samples after all the cuts outlined in Section 6.3.3.

m_{G^*} [GeV]	Mass Window [GeV]
1000	$890 < m_{2HC} < 1030$
1500	$1320 < m_{2HC} < 1540$
2000	$1780 < m_{2HC} < 2050$
2500	$2200 < m_{2HC} < 2570$
3000	$2670 < m_{2HC} < 3070$

Table 6.1.: The mass windows for each signal sample for which the results are presented.

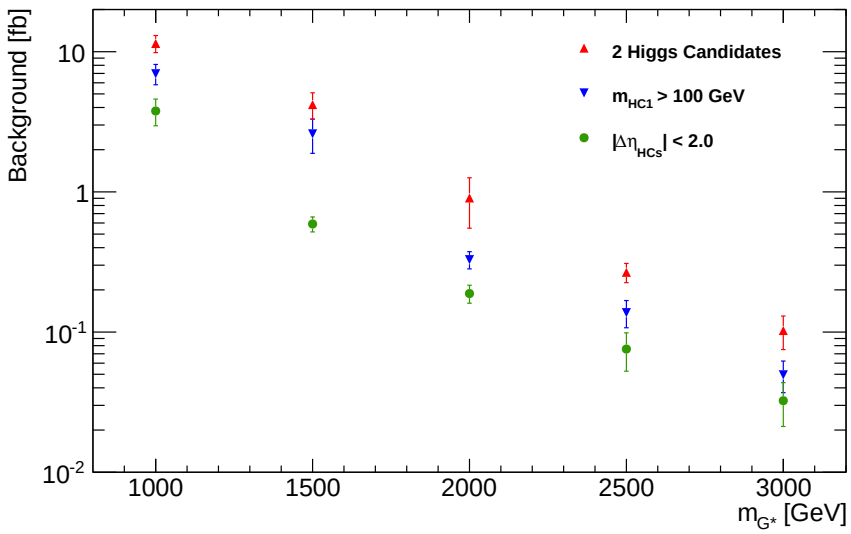

Figure 6.8.: The background cross-section for each of the signal samples in their m_{2HC} windows, at each stage of the cuts.

Figure 6.8 shows the predicted cross-section background within these m_{2HC} windows at each stage of the event selection. Figure 6.9 shows the selection efficiency for each signal at all stages of the event selection. The $m_{G^*} = 1$ TeV signal has the lowest selection efficiency due to the individual jet $p_{\mathrm{T}} > 40$ GeV requirement and also due to the Higgs boson decay products sometimes being outside $\Delta R < 1.5$. The higher graviton masses have a larger selection efficiency since their decay products are almost always within $\Delta R < 1.5$ and also they have a harder subleading jet p_{T} distribution. The higher graviton masses also have a larger selection efficiency due to the lower b-tagging requirements for the Fully Merged HCs.

6.3.4. Results

Table 6.2 shows the total background and signal cross-section for each of the m_{2HC} mass windows, along with the s/b. The $s/\sqrt{b}$ assuming $3\mathrm{ab}^{-1}$ of data is also shown. The lowest graviton mass has the highest significance at 26.2 ± 2.9, with the significance dropping after this due to the lower cross sections of each graviton mass.

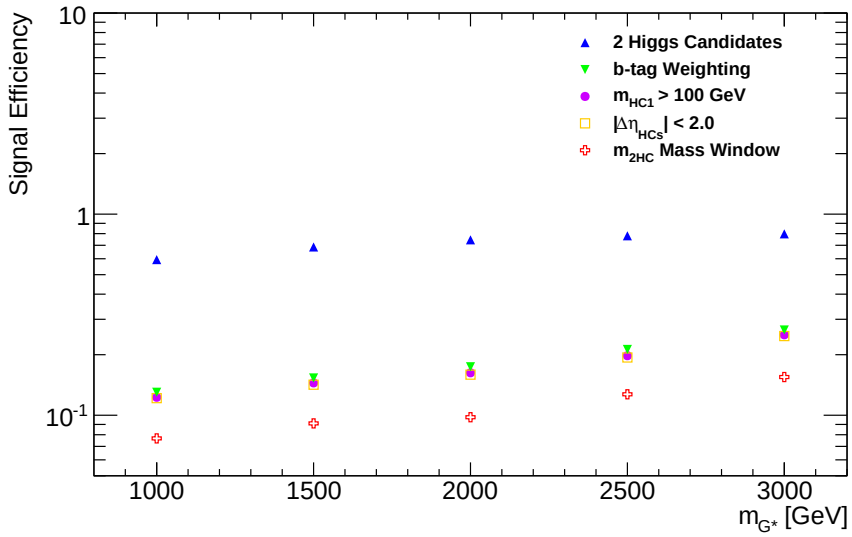

Figure 6.9.: The selection efficiency at each stage of the event selection outlined in Section 6.3.3 for all of the signals.

	m_{2HC} Window [GeV]				
	$890 - 1030$	$1320 - 1540$	$1780 - 2050$	$2200 - 2570$	$2670 - 3070$
Graviton Mass [TeV]	1.0	1.5	2.0	2.5	3.0
Signal Cross Section [fb]	0.93 ± 0.02	0.106 ± 0.002	$(17.5 \pm 0.3) \times 10^{-3}$	$(4.59 \pm 0.07) \times 10^{-3}$	$(1.33 \pm 0.02) \times 10^{-3}$
Total Background Cross Section [fb]	3.8 ± 0.8	0.59 ± 0.07	0.19 ± 0.03	$(7.6 \pm 2.3) \times 10^{-2}$	$(3.2 \pm 1.1) \times 10^{-2}$
s/b	0.25 ± 0.05	0.18 ± 0.02	$(9.3 \pm 1.4) \times 10^{-2}$	$(6.1 \pm 1.9) \times 10^{-2}$	$(4.1 \pm 1.4) \times 10^{-2}$
$s/\sqrt{b}$ (for 3 ab^{-1})	26.2 ± 2.9	7.5 ± 0.5	2.2 ± 0.2	0.91 ± 0.14	0.40 ± 0.07

Table 6.2.: Total cross-sections of the graviton signals after the full event selection, and the corresponding s/b and $s/\sqrt{b}$ (for 3 ab^{-1}) within the m_{2HC} windows outlined in Table 6.1.

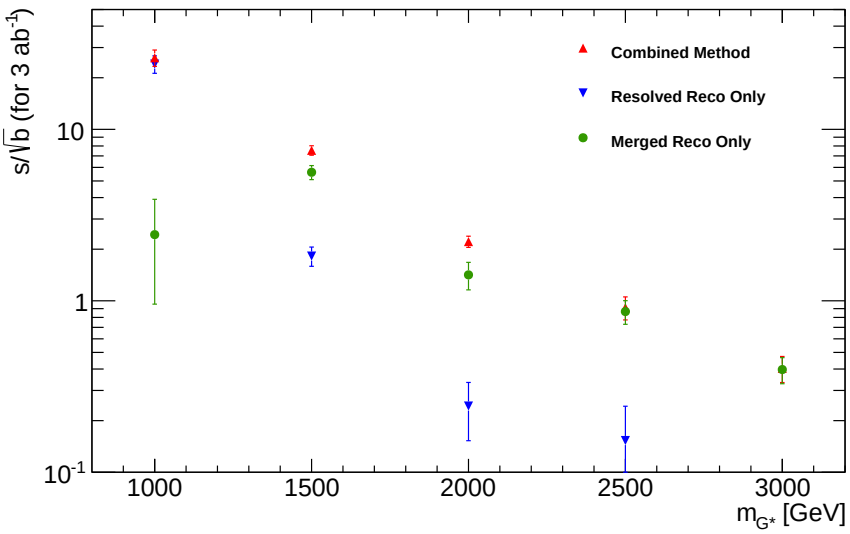

Figure 6.10.: The $s/\sqrt{b}$ for 3 ab^{-1} for each of the signal samples in their m_{2HC} windows. Also shown is these values when using only one type of reconstruction method - either the resolved method or the merged method with one or two track-jets.

Figure 6.10 shows the $s/\sqrt{b}$ for 3 ab^{-1} in the m_{2HC} windows for the Higgs Candidate reconstruction method ("Combined Method") and also for the results obtained from either just using the Resolved dijet method ("Resolved Reco Only") to reconstruct events or using the Merged reconstruction ("Merged Reco Only") (this is the combination of a single anti-k_t R = 0.4 jet with either one or two associated track-jets per Higgs Candidate, with the HC $p_{\mathrm{T}} > 300/600$ GeV). The Combined HC method performs better than the Resolved only or Merged only cases for the 1 - 2 TeV m_{2HC} windows and for the higher masses it performs the same as the Merged method, as the contribution from the Resolved method becomes negligible.

6.3.5. Conclusions

By using the combined approach of three different Higgs boson reconstruction methods, a high signal efficiency is attained across the large Graviton mass range. Using anti-k_t R = 0.4 jets as the basis for the three types of HC reconstruction works well, and the combination does not have any gaps in efficiency. A simple cut-based analysis has shown that this method works and is superior to using separate

reconstruction techniques. The sensitivity could be improved by using more complex analysis techniques, such as a BDT, as in the non-resonant case.

Chapter 7.

Conclusions

This thesis covered searches for Higgs boson pair production in the $b\bar{b}b\bar{b}$ final state at the LHC. All-hadronic final states provide challenging search channels due to the large QCD background but through the use of b-tagging and requiring the Higgs bosons to have large transverse momenta the search for $pp \to hh \to b\bar{b}b\bar{b}$ has been made possible.

A search for resonant and non-resonant $pp \to hh \to b\bar{b}b\bar{b}$ was performed with $\sqrt{s} = 8$ TeV data collected by ATLAS in 2012, corresponding to an integrated luminosity of 19.5 fb^{-1}. Using anti-k_t R = 0.4 jets, Higgs bosons were reconstructed as a pair of close-by b-tagged jets, requiring a high transverse momentum for the dijet system. The resonant signals looked for were a Randall-Sundrum Kaluza-Klein graviton and a heavy neutral scalar boson in the 2HDM model. A non-resonant search was also performed. The combination of multijet and b-jet triggers provided an estimated trigger efficiency of 99% (or better) for signal events passing the full offline selection, for all resonant signal masses. The large QCD background was estimated using a data-driven method. No evidence for resonant or non-resonant Higgs boson pair production was observed. Upper limits were set on $\sigma(pp \to G^* \to hh \to b\bar{b}b\bar{b})$ and $\sigma(pp \to hh \to b\bar{b}b\bar{b})$.

Simulation studies for searches for $pp \to hh \to b\bar{b}b\bar{b}$ at $\sqrt{s} = 14$ TeV were also presented, these are applicable to Run 2 of the LHC and also the HL-LHC. In the non-resonant search it was shown that a dijet method similar to the Run 1 search provided a better signal selection efficiency than a larger radius jet with subjets. The resonant search used gravitons for the signal. It was shown here that a combination

of Higgs reconstruction techniques was more optimal than using just one method, e.g. dijets.

Appendix A.

Bad Channel Correction Study

Throughout the data taking periods in 2012 there were some tile calorimeter modules in ATLAS that were either temporarily or permanently masked. The bad channel correction, BCH, was applied to the affected cells to estimate jet energies, but it was shown to be inaccurate for high-p_{T} jets. Figure A.1a shows the leading jet distribution on "2-tag" data after the basic kinematic cuts defined in Section 5.2.4, some of these masked regions can be seen in the plot. Figure A.1b shows the $m_{4\mathrm{j}}$ distribution from this sample, one can see that the masked events have little impact.

The signal MC samples used in Chapter 5 only had one of the masked modules simulated, two signal MC samples were generated with the masked modules fully modelled. Figure A.2 compares the $m_{4\mathrm{j}}$ distributions for these samples among with the nominal samples and the nominal samples with $+1\sigma$ JER uncertainty shift. The effects of these masked modules are well within the JER uncertainty.

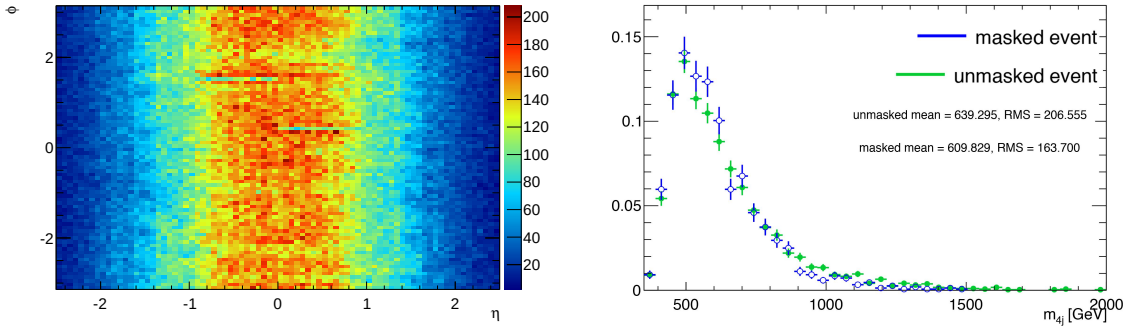

(a) **(b)**

Figure A.1.: **(a)** The η-ϕ distributions of the leading jet in the "2-tag" data sample. **(b)** The $m_{4\mathrm{j}}$ distribution in 2-tag events with and without the BCH issues.

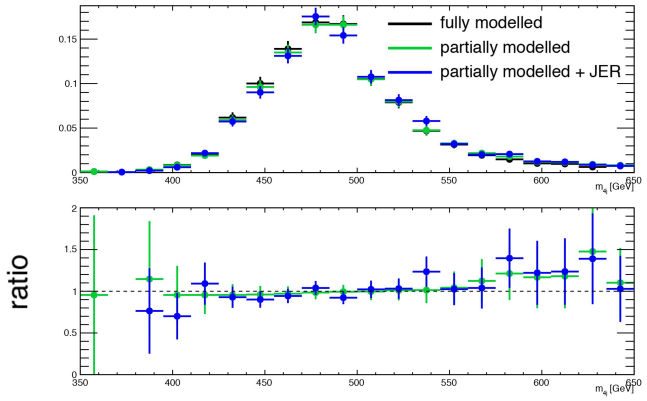

(a) $m_{4\mathrm{j}} = 500$ GeV

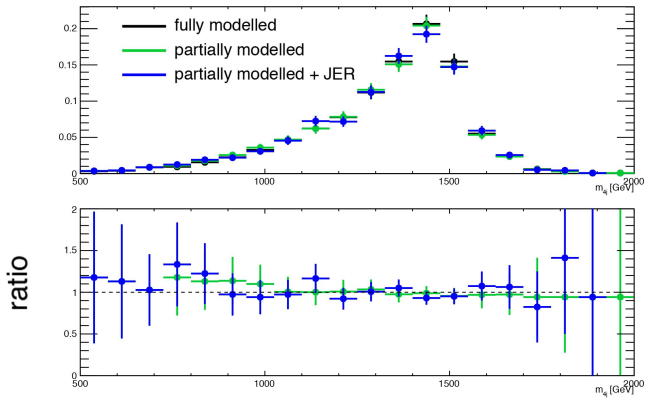

(b) $m_{4\mathrm{j}} = 1500$ GeV

Figure A.2.: The $m_{4\mathrm{j}}$ distributions in the graviton signal samples with and without the extra modules simulated and also with the baseline $+1\sigma$ JER uncertainty.

Colophon

This thesis was made in LaTeX 2_ε using the "hepthesis" class [104].

Bibliography

[1] ATLAS Collaboration, G. Aad et al., *Search for Higgs boson pair production in the $b\bar{b}b\bar{b}$ final state from pp collisions at $\sqrt{s} = 8$ TeV with the ATLAS detector*, Eur. Phys. J. **C75** (2015) no. 9, 412, arXiv:1506.00285 [hep-ex].

[2] D. Wardrope, E. Jansen, N. Konstantinidis, B. Cooper, R. Falla, and N. Norjoharuddeen, *Non-resonant Higgs-pair production in the $b\bar{b}$ $b\bar{b}$ final state at the LHC*, Eur. Phys. J. **C75** (2015) no. 5, 219, arXiv:1410.2794 [hep-ph].

[3] ATLAS Collaboration, G. Aad et al., *Observation of a new particle in the search for the Standard Model Higgs boson with the ATLAS detector at the LHC*, Phys. Lett. **B716** (2013) 1–29, arXiv:1207.7214 [hep-ex].

[4] CMS Collaboration, S. Chatrchyan et al., *Observation of a new boson at a mass of 125 GeV with the CMS experiment at the LHC*, Phys. Lett. **B716** (2012) 30–61, arXiv:1207.7235 [hep-ex].

[5] S. Dawson, S. Dittmaier, and M. Spira, *Neutral Higgs-boson pair production at hadron colliders: QCD corrections*, Phys. Rev. D **58** (Nov, 1998) 115012, arXiv:hep-ph/9703387.

[6] J. Grigo, J. Hoff, K. Melnikov, and M. Steinhauser, *On the Higgs boson pair production at the LHC*, Nucl. Phys. **B875** (2013) 1–17, arXiv:1305.7340 [hep-ph].

[7] D. de Florian and J. Mazzitelli, *Higgs Boson Pair Production at Next-to-Next-to-Leading Order in QCD*, Phys. Rev. Lett. **111** (Nov, 2013) 201801, arXiv:1309.6594.

[8] K. Agashe, H. Davoudiasl, G. Perez, and A. Soni, *Warped Gravitons at the LHC and Beyond*, Phys. Rev. **D76** (2007) 036006, arXiv:hep-ph/0701186

[hep-ph].

[9] A. L. Fitzpatrick, J. Kaplan, L. Randall, and L.-T. Wang, *Searching for the Kaluza-Klein Graviton in Bulk RS Models*, JHEP **09** (2007) 013, arXiv:hep-ph/0701150 [hep-ph].

[10] R. Grober and M. Muhlleitner, *Composite Higgs Boson Pair Production at the LHC*, JHEP **06** (2011) 020, arXiv:1012.1562 [hep-ph].

[11] R. Contino, M. Ghezzi, M. Moretti, G. Panico, F. Piccinini, and A. Wulzer, *Anomalous Couplings in Double Higgs Production*, JHEP **08** (2012) 154, arXiv:1205.5444 [hep-ph].

[12] A. Salam, *Weak and Electromagnetic Interactions*, Conf. Proc. **C680519** (1968) 367–377.

[13] S. Weinberg, *A Model of Leptons*, Phys. Rev. Lett. **19** (1967) 1264–1266.

[14] S. L. Glashow, *Partial Symmetries of Weak Interactions*, Nucl. Phys. **22** (1961) 579–588.

[15] F. Englert and R. Brout, *Broken Symmetry and the Mass of Gauge Vector Mesons*, Phys. Rev. Lett. **13** (1964) 321–323.

[16] P. W. Higgs, *Broken Symmetries and the Masses of Gauge Bosons*, Phys. Rev. Lett. **13** (1964) 508–509.

[17] G. S. Guralnik, C. R. Hagen, and T. W. B. Kibble, *Global Conservation Laws and Massless Particles*, Phys. Rev. Lett. **13** (1964) 585–587.

[18] P. W. Higgs, *Spontaneous Symmetry Breakdown without Massless Bosons*, Phys. Rev. **145** (1966) 1156–1163.

[19] T. W. B. Kibble, *Symmetry breaking in nonAbelian gauge theories*, Phys. Rev. **155** (1967) 1554–1561.

[20] R. K. Ellis, W. J. Striling, and B. R. Webber, *QCD and Collider Physics*, Cambridge University Press (1996) .

[21] K. A. Olive and others. (Particle Data Group), *Review of Particle Physics*, Chin. Phys. **C38** (2014) 090001.

[22] ATLAS and CMS Collaborations, *Combined Measurement of the Higgs Boson Mass in pp Collisions at $\sqrt{s} = 7$ and 8 TeV with the ATLAS and CMS Experiments*, Phys. Rev. Lett. **114** (2015) 191803, arXiv:1503.07589 [hep-ex].

[23] ATLAS and CMS Collaborations, *Measurements of the Higgs boson production and decay rates and constraints on its couplings from a combined ATLAS and CMS analysis of the LHC pp collision data at $\sqrt{s} = 7$ and 8 TeV*, Tech. Rep. ATLAS-CONF-2015-044, CERN, Geneva, Sep, 2015. https://cds.cern.ch/record/2052552.

[24] ATLAS Collaboration, G. Aad et al., *Search for the Standard Model Higgs boson produced in association with a vector boson and decaying to a b-quark pair with the ATLAS detector*, Phys. Lett. **B718** (2013) 369–390, arXiv:1207.0210 [hep-ex].

[25] ATLAS Collaboration, G. Aad et al., *Search for the Standard Model Higgs boson produced in association with top quarks and decaying into $b\bar{b}$ in pp collisions at $\sqrt{s} = 8$ TeV with the ATLAS detector*, Eur. Phys. J. **C75** (2015) no. 7, 349, arXiv:1503.05066 [hep-ex].

[26] CMS Collaboration, S. Chatrchyan et al., *Search for the standard model Higgs boson produced in association with a W or a Z boson and decaying to bottom quarks*, Phys. Rev. **D89** (2014) no. 1, 012003, arXiv:1310.3687 [hep-ex].

[27] CMS Collaboration, V. Khachatryan et al., *Search for the standard model Higgs boson produced through vector boson fusion and decaying to $b\bar{b}$*, Phys. Rev. **D92** (2015) no. 3, 032008, arXiv:1506.01010 [hep-ex].

[28] CMS Collaboration, V. Khachatryan et al., *Search for a Standard Model Higgs Boson Produced in Association with a Top-Quark Pair and Decaying to Bottom Quarks Using a Matrix Element Method*, Eur. Phys. J. **C75** (2015) no. 6, 251, arXiv:1502.02485 [hep-ex].

[29] ATLAS Collaboration, G. Aad et al., *Search For Higgs Boson Pair Production in the $\gamma\gamma b\bar{b}$ Final State using pp Collision Data at $\sqrt{s} = 8$ TeV from the ATLAS Detector*, Phys. Rev. Lett. **114** (2015) no. 8, 081802, arXiv:1406.5053 [hep-ex].

[30] ATLAS Collaboration, G. Aad et al., *Searches for Higgs boson pair production in the $hh \to bb\tau\tau, \gamma\gamma WW*, \gamma\gamma bb, bbbb$ channels with the ATLAS detector*, arXiv:1509.04670 [hep-ex].

[31] CMS Collaboration, V. Khachatryan et al., *Searches for a heavy scalar boson H decaying to a pair of 125 GeV Higgs bosons hh or for a heavy pseudoscalar boson A decaying to Zh, in the final states with h to tautau*, arXiv:1510.01181 [hep-ex].

[32] CMS Collaboration, *Search for the resonant production of two Higgs bosons in the final state with two photons and two bottom quarks*, Tech. Rep. CMS-PAS-HIG-13-032, CERN, 2014.

[33] CMS Collaboration, V. Khachatryan et al., *Searches for heavy Higgs bosons in two-Higgs-doublet models and for $t \to ch$ decay using multilepton and diphoton final states in pp collisions at 8 TeV*, Phys. Rev. **D90** (2014) 112013, arXiv:1410.2751 [hep-ex].

[34] CMS Collaboration, V. Khachatryan et al., *Search for resonant pair production of Higgs bosons decaying to two bottom quark-antiquark pairs in proton-proton collisions at 8 TeV*, Phys. Lett. **B749** (2015) 560–582, arXiv:1503.04114 [hep-ex].

[35] G. C. Branco, P. M. Ferreira, L. Lavoura, M. N. Rebelo, M. Sher, and J. P. Silva, *Theory and phenomenology of two-Higgs-doublet models*, Phys. Rept. **516** (2012) 1–102, arXiv:1106.0034 [hep-ph].

[36] G. K. H.E. Haber, *The search for supersymmetry: Probing physics beyond the standard model*, Physics Reports **117** (1985) no. 2-4, 75–263. http://www.sciencedirect.com/science/article/pii/0370157385900511.

[37] O. S. Brüning, P. Collier, P. Lebrun, S. Myers, R. Ostojic, J. Poole, and P. Proudlock, *LHC Design Report*. CERN, Geneva, 2004. https://cds.cern.ch/record/782076.

[38] ATLAS Collaboration, G. Aad et al., *The ATLAS Experiment at the CERN Large Hadron Collider*, JINST **3** (2008) S08003.

[39] CMS Collaboration, S. Chatrchyan et al., *The CMS experiment at the CERN LHC*, JINST **3** (2008) S08004.

[40] LHCb Collaboration, A. A. Alves, Jr. et al., *The LHCb Detector at the LHC*, JINST **3** (2008) S08005.

[41] ALICE Collaboration, K. Aamodt et al., *The ALICE experiment at the CERN LHC*, JINST **3** (2008) S08002.

[42] CERN, *CERN's Accelerator Complex*, `http://cds.cern.ch/record/1621583`, 2003.

[43] ATLAS Experiment © 2008 CERN, *Computer generated image of the whole ATLAS detector*, `http://cds.cern.ch/record/1095924`.

[44] ATLAS Experiment © 2008 CERN, *Computer generated image of the ATLAS inner detector*, `http://cds.cern.ch/record/1095926`.

[45] ATLAS Experiment © 2008 CERN, *Computer Generated image of the ATLAS calorimeter*, `http://cds.cern.ch/record/1095927`.

[46] ATLAS Experiment © 2008 CERN, *Computer generated image of the ATLAS Muons subsystem*, `http://cds.cern.ch/record/1095929`.

[47] ATLAS Collaboration, G. Aad et al., *Improved luminosity determination in pp collisions at sqrt(s) = 7 TeV using the ATLAS detector at the LHC*, Eur. Phys. J. **C73** (2013) no. 8, 2518, `arXiv:1302.4393 [hep-ex]`.

[48] S. van der Meer, *Calibration of the effective beam height in the ISR*, Tech. Rep. CERN-ISR-PO-68-31. ISR-PO-68-31, CERN, Geneva, 1968. `https://cds.cern.ch/record/296752`.

[49] M. Capeans, G. Darbo, K. Einsweiller, M. Elsing, T. Flick, M. Garcia-Sciveres, C. Gemme, H. Pernegger, O. Rohne, and R. Vuillermet, *ATLAS Insertable B-Layer Technical Design Report*, Tech. Rep. CERN-LHCC-2010-013. ATLAS-TDR-19, CERN, Geneva, Sep, 2010. `https://cds.cern.ch/record/1291633`.

[50] ATLAS Collaboration, *Physics at a High-Luminosity LHC with ATLAS*, Tech. Rep. ATL-PHYS-PUB-2012-001, CERN, Geneva, Aug, 2012. `https://cds.cern.ch/record/1472518`.

[51] ATLAS Collaboration, *Physics at a High-Luminosity LHC with ATLAS (Update)*, Tech. Rep. ATL-PHYS-PUB-2012-004, CERN, Geneva, Oct, 2012.

https://cds.cern.ch/record/1484890.

[52] M. Cacciari, G. P. Salam, and G. Soyez, *The Anti-k(t) jet clustering algorithm*, JHEP **04** (2008) 063, arXiv:0802.1189 [hep-ph].

[53] Y. L. Dokshitzer, G. D. Leder, S. Moretti, and B. R. Webber, *Better jet clustering algorithms*, JHEP **08** (1997) 001, arXiv:hep-ph/9707323 [hep-ph].

[54] S. Catani, Y. L. Dokshitzer, M. H. Seymour, and B. R. Webber, *Longitudinally invariant K_t clustering algorithms for hadron hadron collisions*, Nucl. Phys. **B406** (1993) 187–224.

[55] W. Lampl, S. Laplace, D. Lelas, P. Loch, H. Ma, S. Menke, S. Rajagopalan, D. Rousseau, S. Snyder, and G. Unal, *Calorimeter Clustering Algorithms: Description and Performance*, Tech. Rep. ATL-LARG-PUB-2008-002. ATL-COM-LARG-2008-003, CERN, Geneva, Apr, 2008. https://cds.cern.ch/record/1099735.

[56] ATLAS Collaboration, *Flavor Tagging with Track Jets in Boosted Topologies with the ATLAS Detector*, Tech. Rep. ATL-PHYS-PUB-2014-013, CERN, Geneva, Aug, 2014. https://cds.cern.ch/record/1750681.

[57] ATLAS Collaboration, G. Aad et al., *Jet energy measurement and its systematic uncertainty in proton-proton collisions at $\sqrt{s} = 7$ TeV with the ATLAS detector*, Eur. Phys. J. **C75** (2015) 17, arXiv:1406.0076 [hep-ex].

[58] ATLAS Collaboration, G. Aad et al., *Jet energy resolution in proton-proton collisions at $\sqrt{s} = 7$ TeV recorded in 2010 with the ATLAS detector*, Eur. Phys. J. **C73** (2013) no. 3, 2306, arXiv:1210.6210 [hep-ex].

[59] ATLAS Collaboration, *Commissioning of the ATLAS high-performance b-tagging algorithms in the 7 TeV collision data*, Tech. Rep. ATLAS-CONF-2011-102, CERN, Geneva, Jul, 2011. http://cds.cern.ch/record/1369219.

[60] G. Piacquadio and C. Weiser, *A new inclusive secondary vertex algorithm for b-jet tagging in ATLAS*, Journal of Physics: Conference Series **119** (2008) no. 3, 032032. http://stacks.iop.org/1742-6596/119/i=3/a=032032.

[61] ATLAS Collaboration, *Calibration of the performance of b-tagging for c and light-flavour jets in the 2012 ATLAS data*, Tech. Rep. ATLAS-CONF-2014-046, CERN, Geneva, Jul, 2014. https://cds.cern.ch/record/1741020.

[62] ATLAS Collaboration, *Calibration of b-tagging using dileptonic top pair events in a combinatorial likelihood approach with the ATLAS experiment*, Tech. Rep. ATLAS-CONF-2014-004, CERN, Geneva, Feb, 2014. http://cds.cern.ch/record/1664335.

[63] GEANT4 Collaboration, S. Agostinelli et al., *GEANT4: A Simulation toolkit*, Nucl. Instrum. Meth. **A506** (2003) 250–303.

[64] The ATLAS collaboration, *The ATLAS Simulation Infrastructure*, The European Physical Journal C **70** (2010) no. 3, . http://dx.doi.org/10.1140/epjc/s10052-010-1429-9.

[65] T. Sjostrand, S. Mrenna, and P. Z. Skands, *A Brief Introduction to PYTHIA 8.1*, Comput. Phys. Commun. **178** (2008) 852, arXiv:0710.3820.

[66] P. Nason, *A New method for combining NLO QCD with shower Monte Carlo algorithms*, JHEP **11** (2004) 040, arXiv:hep-ph/0409146 [hep-ph].

[67] S. Frixione, P. Nason, and C. Oleari, *Matching NLO QCD computations with Parton Shower simulations: the POWHEG method*, JHEP **11** (2007) 070, arXiv:0709.2092 [hep-ph].

[68] S. Frixione, P. Nason, and G. Ridolfi, *A Positive-weight next-to-leading-order Monte Carlo for heavy flavour hadroproduction*, JHEP **09** (2007) 126, arXiv:0707.3088 [hep-ph].

[69] S. Alioli, P. Nason, C. Oleari, and E. Re, *A general framework for implementing NLO calculations in shower Monte Carlo programs: the POWHEG BOX*, JHEP **06** (2010) 043, arXiv:1002.2581 [hep-ph].

[70] T. Gleisberg, S. Hoeche, F. Krauss, M. Schonherr, S. Schumann, F. Siegert, and J. Winter, *Event generation with SHERPA 1.1*, JHEP **02** (2009) 007, arXiv:0811.4622 [hep-ph].

[71] J. Alwall et al., *MadGraph 5: going beyond*, JHEP **1106** (2011) 128,

arXiv:1106.0522.

[72] J. Alwall, R. Frederix, S. Frixione, V. Hirschi, F. Maltoni, O. Mattelaer, H. S. Shao, T. Stelzer, P. Torrielli, and M. Zaro, *The automated computation of tree-level and next-to-leading order differential cross sections, and their matching to parton shower simulations*, JHEP **07** (2014) 079, arXiv:1405.0301 [hep-ph].

[73] X. Artru and G. Mennessier, *String model and multiproduction*, Nucl. Phys. **B70** (1974) 93–115.

[74] R. D. Field and S. Wolfram, *A QCD model for e^+e^- annihilation*, Nuclear Physics B **213** (1983) no. 1, 65 – 84.

[75] B. Cooper, N. Konstantinidis, L. Lambourne, and D. Wardrope, *Boosted $hh \to b\bar{b}b\bar{b}$: A new topology in searches for TeV-scale resonances at the LHC*, Phys. Rev. **D88** (2013) no. 11, 114005, arXiv:1307.0407 [hep-ex].

[76] ATLAS Collaboration, *A search for TeV-scale resonances decaying to $\mathbf{hh} \to b\bar{b}b\bar{b}$*, Tech. Rep. ATLAS-CONF-2014-005, CERN, March, 2014.

[77] D. Stump et al., *Inclusive jet production, parton distributions, and the search for new physics*, JHEP **0310** (2003) 046, arXiv:hep-ph/0303013.

[78] T. Plehn, M. Spira, and P. Zerwas, *Pair production of neutral Higgs particles in gluon-gluon collisions*, Nucl. Phys. B **479** (1996) 46, arXiv:hep-ph/9603205.

[79] R. Frederix et al., *Higgs pair production at the LHC with NLO and parton-shower effects*, Phys. Lett. B **732** (2014) 142, arXiv:1401.7340.

[80] M. Cacciari et al., *Top-pair production at hadron colliders with next-to-next-to-leading logarithmic soft-gluon resummation*, Phys. Lett. B **710** (2012) 612, arXiv:1111.5869.

[81] P. Bärnreuther, M. Czakon, and A. Mitov, *Percent Level Precision Physics at the Tevatron: First Genuine NNLO QCD Corrections to $q\bar{q} \to t\bar{t} + X$*, Phys. Rev. Lett. **109** (2012) 132001, arXiv:1204.5201.

[82] M. Czakon and A. Mitov, *NNLO corrections to top-pair production at hadron colliders: the all-fermionic scattering channels*, JHEP **1212** (2012) 054,

arXiv:1207.0236.

[83] M. Czakon and A. Mitov, *NNLO corrections to top pair production at hadron colliders: the quark-gluon reaction*, JHEP **1301** (2013) 080, arXiv:1210.6832.

[84] M. Czakon, P. Fiedler, and A. Mitov, *The total top quark pair production cross-section at hadron colliders through $O(\alpha_S^4)$*, Phys. Rev. Lett. **110** (2013) 252004, arXiv:1303.6254.

[85] M. Czakon and A. Mitov, *Top++: A Program for the Calculation of the Top-Pair Cross-Section at Hadron Colliders*, Comput. Phys. Commun. **185** (2014) 2930, arXiv:1112.5675 [hep-ph].

[86] ATLAS Collaboration, *Measurement of the top quark pair differential cross-sections in the l+jets channel in pp collisions at $\sqrt{s} = 7$ TeV using the ATLAS detector*, Tech. Rep. ATLAS-CONF-2013-099, CERN, September, 2013.

[87] H.-L. Lai et al., *New parton distributions for collider physics*, Phys. Rev. D **82** (2010) 074024, arXiv:1007.2241.

[88] S. Alioli, P. Nason, C. Oleari, and E. Re, *Vector boson plus one jet production in POWHEG*, JHEP **1101** (2011) 095, arXiv:1009.5594 [hep-ph].

[89] ATLAS Collaboration, *Selection of jets produced in proton-proton collisions with the ATLAS detector using 2011 data*, Tech. Rep. ATLAS-CONF-2012-020, CERN, Geneva, March, 2012.

[90] ATLAS Collaboration, G. Aad et al., *Measurement of the muon reconstruction performance of the ATLAS detector using 2011 and 2012 LHC proton-proton collision data*, Eur. Phys. J. **C74** (2014) no. 11, 3130, arXiv:1407.3935 [hep-ex].

[91] ATLAS Collaboration, *Measurement of the differential cross-section of highly boosted top quarks as a function of their transverse momentum using the ATLAS detector in $\sqrt{s} = 8$ TeV proton-proton collisions*, Tech. Rep. ATLAS-CONF-2014-057, CERN, September, 2014.

[92] A. Martin, W. Stirling, R. Thorne, and G. Watt, *Parton distributions for the LHC*, Eur. Phys. J. C **63** (2009) 189, arXiv:0901.0002.

[93] R. D. Ball et al., *Parton distributions with LHC data*, Nucl. Phys. B **867** (2013) 244, arXiv:1207.1303.

[94] J. Wenninger, *Energy Calibration of the LHC Beams at 4 TeV*, Tech. Rep. CERN-ATS-2013-040, CERN, Geneva, May, 2013. http://cds.cern.ch/record/1546734.

[95] E. Gross and O. Vitells, *Trial factors or the look elsewhere effect in high energy physics*, Eur. Phys. J. **C70** (2010) 525–530, arXiv:1005.1891 [physics.data-an].

[96] A. L. Read, *Presentation of search results: The CL(s) technique*, J.Phys. **G28** (2002) 2693–2704.

[97] G. Cowan, K. Cranmer, E. Gross, and O. Vitells, *Asymptotic formulae for likelihood-based tests of new physics*, Eur.Phys.J. **C71** (2011) 1554, arXiv:1007.1727 [physics.data-an].

[98] Y. Gao, A. V. Gritsan, Z. Guo, K. Melnikov, M. Schulze, and N. V. Tran, *Spin determination of single-produced resonances at hadron colliders*, Phys. Rev. **D81** (2010) 075022, arXiv:1001.3396 [hep-ph].

[99] CMS Collaboration, S. Chatrchyan et al., *Measurement of the properties of a Higgs boson in the four-lepton final state*, Phys. Rev. **D89** (2014) no. 9, 092007, arXiv:1312.5353 [hep-ex].

[100] D. E. Ferreira de Lima, A. Papaefstathiou, and M. Spannowsky, *Standard model Higgs boson pair production in the ($b\bar{b}$)($b\bar{b}$) final state*, JHEP **08** (2014) 030, arXiv:1404.7139 [hep-ph].

[101] H.-L. Lai, M. Guzzi, J. Huston, Z. Li, P. M. Nadolsky, J. Pumplin, and C. P. Yuan, *New parton distributions for collider physics*, Phys. Rev. **D82** (2010) 074024, arXiv:1007.2241 [hep-ph].

[102] N. Greiner, A. Guffanti, T. Reiter, and J. Reuter, *NLO QCD corrections to the production of two bottom-antibottom pairs at the LHC*, Phys. Rev. Lett. **107** (2011) 102002, arXiv:1105.3624 [hep-ph].

[103] ATLAS Collaboration, *Identification and Tagging of Double b-hadron jets with the ATLAS Detector*, Tech. Rep. ATLAS-CONF-2012-100, CERN, July, 2012.

[104] A. Buckley, *A class for typesetting academic theses*, 2010.